

A Study of
Plasma-Induced Surface Roughness and Ripple Formation
during Silicon Etching in Inductively Coupled Chlorine Plasmas

Nobuya NAKAZAKI

2016

Preface

This thesis discusses the atomic- or nanometer-scale plasma-induced surface roughness and ripple structures formed on etched surfaces as a result of plasma–surface interactions during plasma etching. The plasma–surface interactions are extremely complicated because those include many chemical and physical interactions both within the plasma and on the surfaces exposed to the plasma, while the nature enables surface modification and material processing unattainable by chemical methods.

Plasma etching, which is one of the active applications of the plasma–surface interactions, is a surface processing technique indispensable for fabrications of today’s state-of-the-art electronic devices. In plasma etching processes of semiconductor-based devices, energetic ions and reactive neutrals generated in the plasma remove atoms from material surfaces through nonequilibrium processes to fabricate nanoscale three-dimensional structures on the substrate, where strict requirements are imposed on plasma etching technology, including precise control of profile, critical dimension (CD), and their microscopic uniformity (or aspect-ratio dependence), together with that of etch rate, selectivity, and damage. As the device dimensions continue to be scaled down, atomic- or nanometer-scale plasma-induced surface roughness becomes one of the most important issues to be resolved in the fabrication of nanoscale microelectronics devices, because the roughness formed during plasma etching would be comparable with the CD and the thickness of the layer being etched and/or the layer underlying.

However, the mechanisms for surface roughening during plasma etching are not yet fully understood, depending on a number of factors in processing.

In this study, experiments of Si etching in inductively coupled Cl₂ plasmas have been performed, with attention to atomic- or nanometer-scale surface roughness and ripple formation during plasma etching for a deeper understanding of plasma–surface interactions that are responsible for. In the experiments, the plasma and etched surfaces were measured and characterized by using several diagnostic techniques. In addition, numerical simulations have been conducted by Monte Carlo-based three-dimensional atomic-scale cellular model for the surface feature evolution and classical molecular dynamics for etch fundamentals, to interpret the mechanisms of surface roughening.

Firstly, plasma-induced surface roughening on blank or planar substrates was investigated as a function of bias power or ion incident energy in the range $E_i \approx 20\text{--}500$ eV, by varying the feed gas flow rate, wafer stage temperature, and etching or plasma exposure time. The experiments found two modes of plasma-induced surface roughening which occur depending on E_i ; and the mechanisms of interest were revealed with the help of plasma diagnostics and numerical simulations. One is the roughening mode at low $E_i < 200\text{--}300$ eV, where the root-mean-square (rms) roughness of etched surfaces increases with increasing E_i , exhibiting an almost linear increase with time during etching ($t < 20$ min); the other is the smoothing mode at higher E_i , where the rms roughness decreases substantially with E_i down to a low level of RMS < 0.4 nm, reaching a quasi-steady state after some increase at the initial stage ($t < 1$ min). The mode transition is ascribed primarily to reduced effects of the ion reflection on surfaces owing to a change of incident ion species.

Secondly, surface smoothing of pre-roughened substrates was achieved by plasma etching in the smoothing mode, and the experiments indicated that a threshold for initial surface roughness exists for the surface smoothing. In addition, off-normal ion incidence onto surfaces was achieved during plasma etching by using sheath control plates, and surface rippling by oblique ion incidence during plasma etching was demonstrated; more precisely, at ion incident angle $\theta_i \approx 40^\circ$ or oblique ion incidence, periodic or ripple structures were formed on surface perpendicularly to the direction of ion incidence, while at $\theta_i \approx 80^\circ$ or grazing ion incidence, small ripples or slit like grooves were formed on the surface parallel to the direction of ion incidence. These experimental results of the surface smoothing and rippling were well consistent with predictions of numerical simulations.

Acknowledgements

This study was carried out in Propulsion Engineering Laboratory, Department of Aeronautics and Astronautics, Graduate School of Engineering, Kyoto University (Ono, Eriguchi, Takao Lab.) from April 2011 to March 2016. My special thanks go to everyone who has helped me to complete this work.

First and foremost, I would like to express sincere appreciation to my adviser, Prof. Kouichi Ono for his thorough guidance and patience in every aspect over the graduate course, and for giving me many chances to present papers in various international conferences. I learned an awful lot from his immense knowledge of plasma physics, experimental techniques, and writing skill in English. His excellent education I was received is the most invaluable in my life.

I give heartfelt thanks to Associate Prof. Koji Eriguchi and Assistant Prof. Yoshinori Takao (Associate Prof. in Yokohama National University from April 2014) for fruitful discussion on my research. Their warm advice and encouragement always helped and motivated me.

I would like to thank Prof. Kazuo Aoki and Prof. Takaji Inamuro for their careful review of this thesis and their valuable comments.

I am again grateful to all current and former members in Propulsion Engineering Laboratory for their encouragement and valuable discussion on plasma physics, plasma etching, numerical methods, and experimental techniques, and for sharing me the great time in the

Acknowledgements

laboratory. Especially, I would like to thank Dr. Hiroataka Tsuda for imparting me his great knowledge of plasma etching and experimental/numerical methods used in this study, and Mr. Takumi Saegusa and Mr. Ken Taniguchi for teaching me the molecular dynamics simulation. I would also like to thank Dr. Yoshinori Nakakubo and Dr. Asahiko Matsuda for fruitful discussion about this study and plasma-induced damage. Many thanks must go Mr. Takumi Hatsuse, Mr. Soma Sonobe, and Mr. Haruka Matsumoto for their assistance with simulations and experiments.

This work was supported by a Grant-in-Aid for Scientific Research on Innovative Areas from the Ministry of Education, Culture, Sports, Science and Technology, Japan, and by that from the Japan Society for the Promotion of Science (JSPS). I have also been supported from April 2015 by Research Fellowships from the JSPS for Young Scientists.

And last but not least, I would like to express my deepest gratitude to my family for their continuous support all my life. This work would not have been possible without the warmest support and continuous encouragement from them.

中崎 暢也

Nobuya NAKAZAKI

2016, Kyoto

Nomenclature

Symbols and Units

a	lattice constant	nm
a	cutoff radius	nm
A	proportional constant of yield per ion vs $E_i^{1/2}$	$\text{eV}^{-1/2}$
d_{etch}	etched depth	nm
e	elementary charge ($\approx 1.6 \times 10^{-19}$ C)	C
\mathbf{E}	electrostatic field vector	V/m
E_e	electron energy	eV
E_i	ion incident energy	eV, V
E_n	incident energy of neutrals	eV
E_p	ion energy at peak rms roughness	eV, V
E_r	ion energy after reflection	eV
E_{th}	threshold energy	eV
ER	etch rate	nm/min
ER_{chem}	chemical etch rate	nm/min
\mathbf{f}	force vector	N
F_0	gas flow rate	sccm
h_0	height of the part not to be etched	nm
h_{etch}	height of the part etched	nm
h_s	slit height of sheath control plate	mm
H_{fin}	fin height	nm

Nomenclature

i	imaginary unit	
I	Intensity	
I_0	IR beam intensity of reference spectra	
k	spatial frequency	nm^{-1}
k_B	the Boltzmann constant ($\approx 1.38 \times 10^{-23}$ J/K)	J/K
K	spectral strength of PSD distribution	nm^4
l	absorption pass length	cm
L	ASCeM-3D cell size	Å
L_A	AFM pixel size	nm
L_g	gate length	nm
m	atomic mass	kg
m_{Cl}	atomic mass of Cl ($\approx 5.89 \times 10^{-26}$ kg)	kg
$m_{i,\text{eff}}$	effective ion mass	kg
m_{Si}	atomic mass of Si ($\approx 4.67 \times 10^{-26}$ kg)	kg
n_{Cl}	Cl concentration in gas phase	cm^{-3}
n_e	electron density	cm^{-3}
n_i	ion density	cm^{-3}
N	AFM resolution	
N_d	dopant density	cm^{-3}
N_p	plasma density	cm^{-3}
P	PSD function	nm^4
P_0	gas pressure	mTorr, Pa
P_{ICP}	ICP coil power	W
P_{rf}	rf bias power	W
\mathbf{r}	position of atoms	
r_{ij}	distance between atoms	nm
R	ratio of the ion incident energy to ion temperature	
R_i	reflection probability	
RMS	rms surface roughness	nm
RMS_0	initial surface roughness	nm
$\text{RMS}_{0,\text{th}}$	threshold for initial surface roughness	nm
S	surface area of substrates	cm^2
S_n	sticking probability of neutral Cl	
S_o	sticking probability of neutral O	
S_p	deposition probability of byproducts	
S_q	deposition probability of desorbed products	
t_{etch}	etching time	min
t_{rough}	plasma exposure time of roughening step	min

t_s	blade thickness of sheath control plate	mm
T_e	electron temperature	K, eV
T_g	gas temperature	K, eV
T_i	ion temperature	K, eV
T_s	stage temperature	K
\bar{u}	average thermal velocity	m/s
u_B	Bohm velocity	m/s
\mathbf{v}	velocity vector	m/s
v_n	n -body potential function	
V_0	chamber volume	cm ³
V_{dc}	dc self-bias voltage	V
V_p	plasma potential	V
V_s	sheath potential	V
w_0	plateau height value	nm ⁴
w_s	slit width of sheath control plate	mm
W	ASCeM-3D domain size	nm
W_A	AFM scan length	μm
W_{fin}	fin width	nm
W_g	gate width	nm
Y	yield	
Y^*	effective yield	
Y_{SiClx}	yield for chloride Si surface	
Y_{SiClxO}	yield for oxidized Si surface	
Y_{SiO_2}	yield for SiO ₂ surface	
z	height or depth distribution on surfaces	nm
z_{ave}	average height of surfaces	nm
α_{SiCl_4}	reaction probability of chemical etching	
β	etch selectivity	
Γ_{Cl}	flux of Cl	cm ⁻² s ⁻¹
Γ_i^0	ion flux	cm ⁻² s ⁻¹
Γ_n^0	neutral flux	cm ⁻² s ⁻¹
Γ_o^0	oxygen flux	cm ⁻² s ⁻¹
Γ_p^0	products/byproducts flux	cm ⁻² s ⁻¹
Δt	time step	s
ϵ	energy unit for MD (= 2.1692 eV)	eV
ϵ_0	permittivity in vacuum ($\approx 8.85 \times 10^{-12} \text{ m}^{-3}\text{kg}^{-1}\text{s}^4\text{A}^2$)	$\text{m}^{-3}\text{kg}^{-1}\text{s}^4\text{A}^2$
η	fractal dimension	

Nomenclature

θ	local incident angle	
θ_i	ion incident angle	
θ_n	incident angle of neutrals	
θ_s	slit angle of sheath control plate	
Θ	incident angle	
Θ_d	desorbed angle of products	
κ	miniaturization ratio	
λ_n	mean free pass of neutrals	cm
ξ_0	correlation length	nm
$\xi_{0,th}$	threshold for initial correlation length	nm
ρ	charge density	C/m^{-3}
ρ_r	resistivity	$\Omega \cdot cm$
ρ_s	Si atom density	cm^{-3}
σ	length unit for MD (= 2.0951 Å)	Å
τ_r	gas residence time	s
ϕ	electrostatic potential	V
Φ	potential energy function	
χ	concentration fraction	

Abbreviations

1D	one-dimensional
2D	two-dimensional
3D	three-dimensional
AFM	atomic force microscopy
ASCeM-3D	three-dimensional atomic-scale cellular model
B–H	Bradley and Harper
CCP	capacitively coupled plasma
CD	critical dimension
c-Si	single-crystalline Si
DFT	discrete Fourier transform
ECR	electron cyclotron resonance
FET	field effect transistor
FinFET	fin-type FET
FTIR	Fourier transform infrared
high- k	high dielectric constant
IC	integrated circuit

ICP	inductively coupled plasma
IED	ion energy distribution
ITRS	International Technology Roadmap for Semiconductors
KRS-5	thallium-bromide-iodide
LER	line edge roughness
low- k	low dielectric constant
LWR	line width roughness
MCT	MgCdTe
MD	molecular dynamics
MEMS	microelectromechanical systems
ML	monolayer
MOS	metal-oxide-semiconductor
OES	optical emission spectroscopy
PIC	particle-in-cell
PSD	power spectral density
QMS	quadrupole mass spectrometry
RAS	reflection absorption spectroscopy
rf	radio frequency
rms	root-mean-square
SEM	scanning electron microscopy
STI	shallow trench isolation
SW	Stillinger–Weber
TAS	transmission absorption spectroscopy
ULSI	ultra-large-scale integrated
uv	ultraviolet

Contents

Preface	i
Acknowledgements	iii
Nomenclature	v
Symbols and Units	v
Abbreviations	viii
Contents	xi
Chapter 1 General Introduction	1
1.1 Semiconductor Devices	1
1.1.1 Field effect transistors	3
1.1.2 Device fabrication	4
1.2 Plasma Etching	5
1.2.1 Inductively coupled plasma etcher	6
1.2.2 Plasma–surface interactions	9
1.3 Plasma-Induced Surface Roughness	13
1.3.1 Overview of plasma-induced damage and roughness	13
1.3.2 Previous researches on plasma-induced surface roughness	15
1.4 Structure of This Thesis	17
	xi

Chapter 2 Apparatus, Operation, Sample, and Diagnostics	19
2.1 Plasma Reactor and Etching Sample	20
2.2 Plasma and Surface Diagnostics	22
2.2.1 <i>Optical emission spectroscopy</i>	22
2.2.2 <i>Quadrupole mass spectrometry</i>	24
2.2.3 <i>Langmuir probe</i>	25
2.2.4 <i>Fourier transform infrared absorption spectroscopy</i>	26
2.2.5 <i>Stylus profilometry</i>	27
2.2.6 <i>Atomic force microscopy</i>	28
2.2.7 <i>Scanning electron microscopy</i>	29
Chapter 3 Two Modes of Surface Roughening during Plasma Etching of Silicon	31
3.1 Plasma Parameters	32
3.2 Etch Rate and Surface Roughness	33
3.3 Power Spectral Density of Surface Roughness	41
3.4 Summary	44
Chapter 4 Role of Ionized Etch Products for Surface Roughening	47
4.1 Etch Products and Byproducts	48
4.1.1 <i>Optical emission spectroscopy</i>	48
4.1.2 <i>Infrared absorption spectroscopy</i>	51
4.1.3 <i>Mass spectrometry</i>	53
4.2 Etch Fundamentals of Ionized Etch Products	57
4.3 Mechanisms for Surface Roughening	61
4.3.1 <i>Smoothing mode</i>	62
4.3.2 <i>Roughening mode</i>	64
4.3.3 <i>Overview of mechanisms</i>	67
4.4 Summary	69
Chapter 5 Surface Smoothing and Threshold for Initial Surface Roughness	73
5.1 Experimental Procedure	74
5.2 Roughness Evolution on Pre-roughened Surfaces	75
5.3 Mechanisms for Surface Smoothing	80
5.4 Summary	81

Chapter 6 Surface Rippling by Oblique Ion Incidence during Plasma Etching	83
6.1 Sheath Control Plate for Off-Normal Ion Incidence	85
6.2 Experimental Demonstration of Surface Rippling	87
6.3 Ion Incident Angle Dependence of Etch Rate	90
6.4 Summary	92
Chapter 7 Concluding Remarks	93
7.1 Conclusions	93
7.2 Future Outlooks	95
Appendix A Atomic-Scale Cellular Model	97
A.1 Simulation Domain	98
A.2 Particle Transportation	98
A.3 Surface Chemistry and Kinetics for Si Etching in Cl ₂ /O ₂ Plasmas	101
A.4 Surface Advancement	103
Appendix B Classical Molecular Dynamics	105
B.1 Improved Stillinger-Weber Interatomic Potential for Si/Cl System	105
B.2 Molecular Dynamics Modeling of Cl ₂ Plasma Etching of Silicon	108
Appendix C Particle-in-Cell Simulation	113
C.1 Calculation of Ion Trajectories	113
References	117
List of Publications	127
Journal Paper	127
International Conference	128
Japanese Conference	130
Review	132
Award	132

Chapter 1

General Introduction

1.1 Semiconductor Devices

The electronics industry has grown at an incredible speed since the mid-20th century, and is now the largest industry in the world.^[1-3] The rapid growth came from developments of semiconductor devices, including integrated circuits (ICs), power devices, photonic devices, sensors, and microelectromechanical systems (MEMS). In particular, ICs, which are the core element of today's information technology and telecommunications, were firstly invented by Kilby^[4] and Noyce,^[5] and elevated to ultra-large-scale integrated (ULSI) devices through the continued technological breakthroughs based on Moore's law,^[6,7] which predicts that the number of transistors on an IC chip has been doubling approximately every 18 months. In practice, the modern ULSI device has more than one billion transistors on the chip, which was achieved by the continuous miniaturization of them to sub-20 nm.

According to International Technology Roadmap for Semiconductors (ITRS), the miniaturization of transistors will be continued for years to come.^[8] **Figure 1.1** shows technology trend targets of printed and physical gate length of metal-oxide-semiconductor field effect transistors (MOSFETs) [L_g in Fig. 1.2(a)] in micro-processor units and fin width of recent

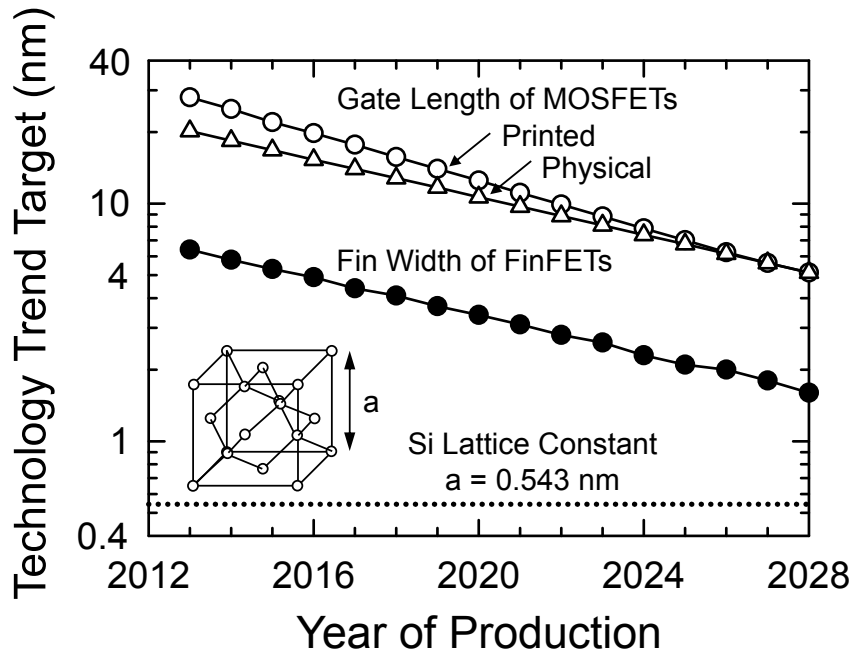


Fig. 1.1. Technology trend targets of printed and physical gate length of MOSFETs in micro-processor units and fin width of FinFETs as a function of year of production.^[8] Inset is a schematic of a unit cell of crystalline Si with the lattice constant of $a = 0.543$ nm.

fin-type FETs (FinFETs) [W_{fin} in Fig. 1.2(b)] as a function of year of production. These FETs are the most important components for ULSI devices and semiconductor memories. The trend indicates that the gate length of MOSFETs and fin width of FinFETs will decrease continuously to sub-10 nm and several nm within this decade, respectively; and the feature sizes will become to be the comparable with a unit cell size (or the lattice constant $a = 0.543$ nm) of crystalline Si, which is the main material of MOSFETs and FinFETs.

One of the driving forces for the extreme miniaturization of transistors is the scaling law,^[2,9] which states that when the dimension of a MOSFET is decreased by a factor of $1/\kappa$ while preserving its electric field pattern, the propagation delay decreases by $1/\kappa$ and the power dissipation by $1/\kappa^2$. Therefore, this characteristic encouraged the developments of microfabrication technologies for semiconductor devices, including photolithography, ion implantation, thin film deposition, polishing, and plasma etching.

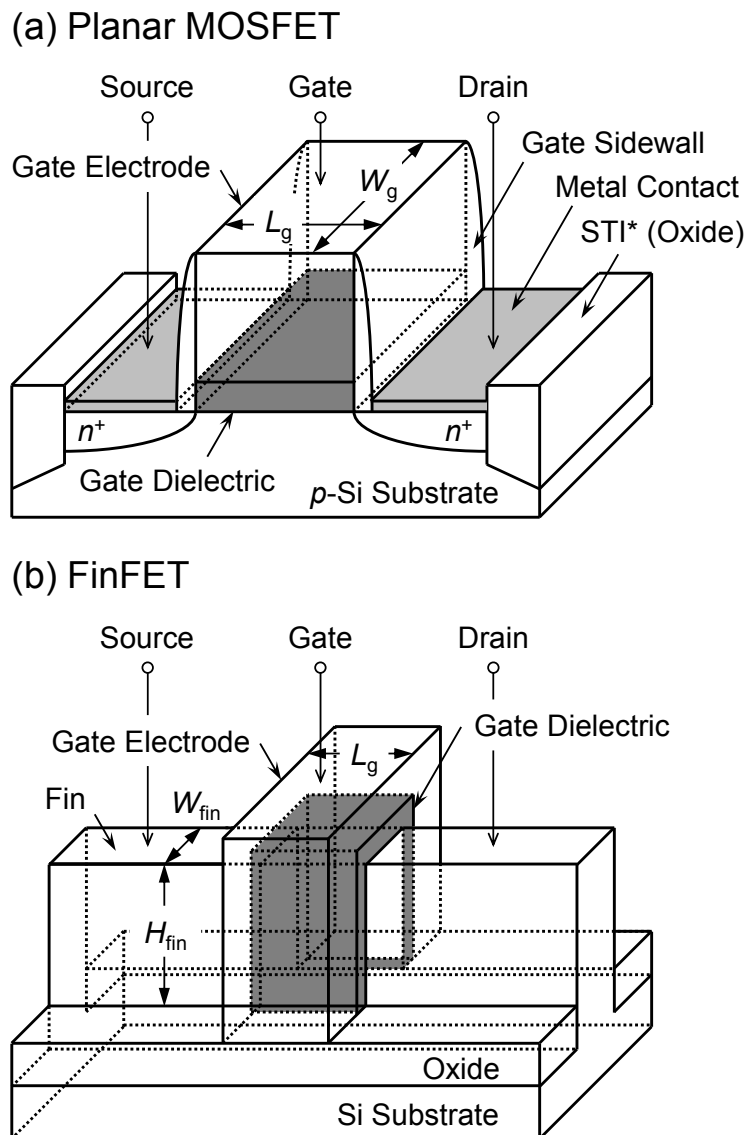


Fig. 1.2. Schematic illustrations of (a) a conventional planar n -channel MOSFET and (b) a 3D FinFET with a bulk silicon substrate.

1.1.1 Field effect transistors

Figure 1.2(a) shows a schematic illustration of a conventional planar n -channel MOSFET.^[10] This three-terminal device consists of a p -type semiconductor substrate (e.g. Si) into which two n^+ -regions, the source and drain, formed by ion implantation. The gate dielectric (e.g. SiO_2) is formed by thermal oxidation of Si between the source and drain, and then the gate electrode is formed thereon by deposition and etching of a highly-doped polysilicon layer. In ICs, this

device is electrically separated from other devices by shallow trench isolation (STI). When a sufficiently large positive bias is applied to the gate, a surface inversion layer (or channel) is formed under the gate dielectric, and then the source and drain are connected by a conducting surface channel, through which a large current can flow.^[1] The current can be modulated by varying the gate voltage. In this way, MOSFET is used as a switching device. The key design parameters for MOSFET performance are the gate or channel length L_g and width W_g , the dielectric thickness, the n^+ -region depth, and the substrate doping.

Figure 1.2(b) shows a schematic illustration of an advanced FinFET with a three-dimensional (3D) multi-gate structure,^[2,11–14] where the gate electrode and dielectric wrap the fin. The gate width for the FinFET shown will be the sum of twice the height plus the width ($W_g \approx 2H_{\text{fin}} + W_{\text{fin}}$), which enables the further miniaturization and higher device performance at low gate voltage comparing to conventional MOSFETs; on the other hand, the fabrication is more difficult because of the complex structure.^[15]

1.1.2 Device fabrication

Figure 1.3 shows a typical processing unit in MOSFETs and FinFETs fabrications to create sub-micrometer features on a large area wafer substrate from a thin film (or target to be etched). A film is grown or deposited on the substrate [Fig. 1.3(a)], followed by photoresist coating over the film [Fig. 1.3(b)]. The resist is selectively exposed to ultraviolet (uv) light through a pattern [Fig. 1.3(c)], and then the exposed regions are removed, leaving behind a patterned resist mask [Fig. 1.3(d)]. This mask pattern is transferred into the target film by an etch process, where the mask protects the underlying film from being etched. The etching techniques are divided into plasma etching [Fig. 1.3(e1)] and wet etching [Fig. 1.3(e2)]. After etching, the remaining resist mask is removed [Figs. 1.3(f1) and 1.3(f2)]. In IC fabrication processes, these steps are repeated to build up a number of different layers.

It is noted that in the plasma etching process [Fig. 1.3(e1)], the mask pattern is faithfully transferred into the target film and vertical sidewalls aligned with the resist mask are achieved. This can be accomplished by an etch process that removes material in the vertical direction only, where the horizontal etch rate is almost zero. Such anisotropic etching is easily produced by plasma processing. On the other hand, the wet etching process [Fig. 1.3(e2)] results in an isotropic etching profile, where undercutting occurs behind the mask. This is produced by comparable vertical and lateral etch rates. The undercutting may be acceptable when the

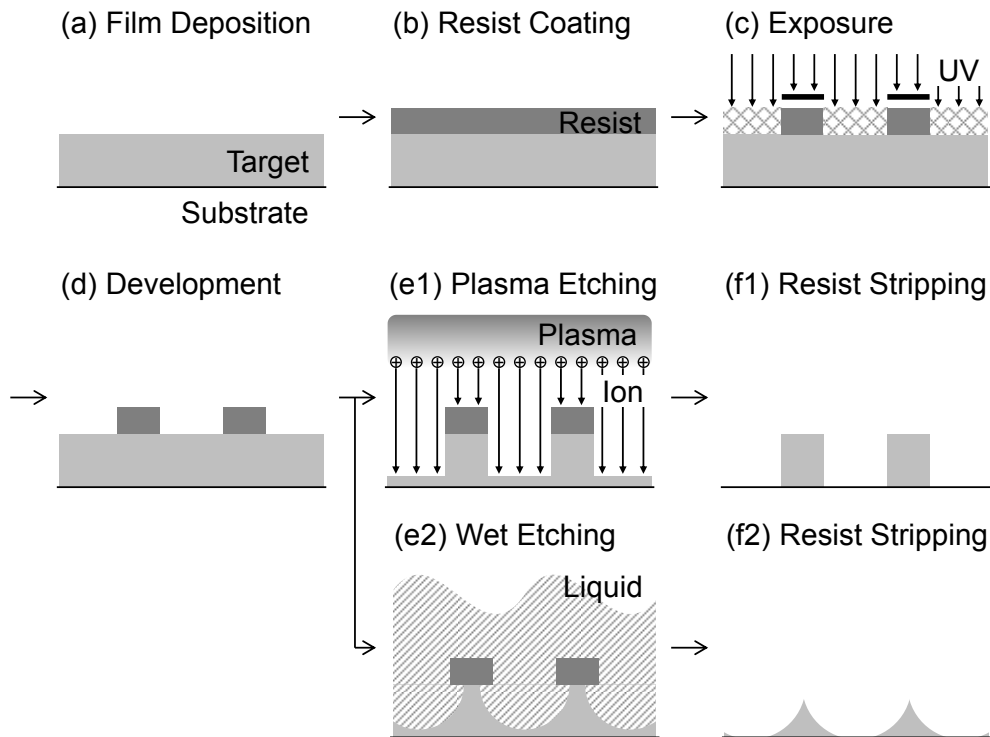


Fig. 1.3. Deposition and pattern transfer in manufacturing an IC: (a) film deposition; (b) photoresist coating; (c) optical exposure through a pattern; (d) photoresist development; (e1) anisotropic plasma etching and (e2) isotropic wet etching; (f1), (f2) remaining photoresist stripping.

feature spacing is much larger than film thickness, but it is no longer true with sub-micrometer feature spacing.^[16] In the reduction of feature sizes and spacings, anisotropic etch processes are essential. Therefore, in today's semiconductor production lines, plasma etching is used for very-high-accuracy transfer of resist patterns.

1.2 Plasma Etching

Plasma etching is now widely employed for manufacturing ULSI devices^[3,17] and MEMS.^[18] In plasma etching, atoms/molecules and ions of them generated in the plasma are used as tools for processing.^[16]

Plasma is a quasi-neutral ionized gas which consists of approximately equal amount of positively charged particles (positive ions) and negatively charged particles (electrons and a small amount of negative ions).^[19] Although plasma is quasi-neutral in a macroscopic sense, it

behaves quite differently from a molecular gas, because the charged particles therein can be influenced by applied electric and magnetic fields. The plasmas used for material processing are low-pressure weakly-ionized plasmas, containing a significant density of neutral particles (typically > 90%), where charged particle collisions with neutral gas molecules are important. Weakly-ionized plasmas are sustained in the steady state primarily by a balance between generation of positive ions through electron impact ionization of neutrals and surface loss of the ions.^[16]

In plasma etching (or reactive ion etching), positive ions and chemically reactive neutrals (or radicals) are generated in the plasma, and then transported toward material surfaces to be etched. After reaching the surfaces, they chemically react with the surface atoms to make a volatile product which desorbs easily from the surface. Therefore, the plasma should be chosen adequately depending on the material to be etched: Cl₂/HBr/O₂ plasmas for Si in FET fabrications, SF₆/O₂ plasmas for Si in MEMS fabrications, fluorocarbon and hydrofluorocarbon plasmas for dielectric materials such as SiO₂, Si₃N₄, SiN, and various low dielectric constant (low-*k*) materials,^[17] Cl₂/O₂ plasmas for photoresist^[16] and Cr,^[20] Cl₂-based plasmas for Al and the alloys, BCl₃/Cl₂/O₂ plasmas for Ti, TiN, and HfO₂,^[21] and CO/NH₃ plasmas for Ni and the alloys.^[22]

The plasma etching systems are extremely complicated owing to many chemical and physical interactions both within the plasma and on the surfaces exposed to the plasma, which are not yet fully understood. In this section, an inductively coupled plasma etcher is introduced as an example of plasma reactors, and plasma generation, particle transportation, and plasma–surface interactions concerned with this study are described.

1.2.1 Inductively coupled plasma etcher

Inductively coupled plasma (ICP) is one of the high density plasmas, as well as electron cyclotron resonance (ECR) plasma,^[23] surface wave plasma,^[24] and helicon plasma.^[25] Such plasma sources can operate with a higher plasma density above $N_p \approx 10^{11} \text{ cm}^{-3}$, a lower neutral-to-ion flux ratio in the range of $\Gamma_n^0/\Gamma_i^0 \approx 1\text{--}1000$, and a much lower plasma potential of $V_p \approx 10 \text{ V}$ than capacitively coupled plasma (CCP) sources (typically, $N_p \approx 10^9\text{--}10^{10} \text{ cm}^{-3}$, $\Gamma_n^0/\Gamma_i^0 \approx 1000\text{--}10000$, and $V_p \approx 100\text{--}1000 \text{ V}$). The high density plasma will lead to high processing rates; additionally the low neutral-to-ion ratio will lead to processes where the ion bombardment on the surface plays a very important role.^[26] The low neutral-to-ion ratio will

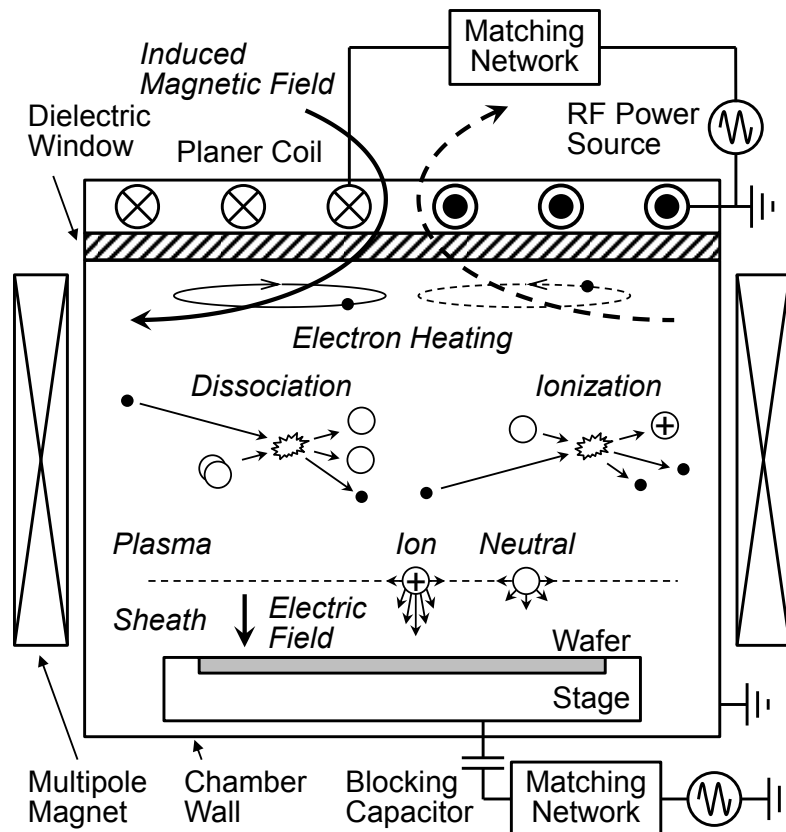


Fig. 1.4. Schematic of a typical ICP etcher with a planar inductive coil, multipole magnets, and wafer stage. Also shown is an illustration of the mechanisms of plasma generation and particle transportation onto the wafer to be processed.

also enhance the anisotropy of the processing, because the ions from the plasma can be directed towards the substrate surface by applying a voltage to the substrate. ICP etchers generally operate at pressures of a few mTorr to tens of mTorr and are used for the etching of STI, gate electrodes, high dielectric constant (high- k) materials, aluminum and its alloys.^[17]

Figure 1.4 shows a schematic of a typical ICP etcher with a planar inductive coil (or spiral antenna). Also shown is an illustration of the mechanisms of plasma generation and particle transportation onto the wafer to be processed. It consists of a cylindrical vacuum chamber (or discharge region), whose diameter is typically larger than its height. Most semiconductor processing applications are very sensitive to contamination by metallic,^[27,28] so the induction coil is placed outside of the vacuum chamber, separated from the plasma by a dielectric window typically made of quartz or alumina, where some of the window materials will be sputtered into the plasma. In addition, some etchers employ an array of multipolar magnets placed around

the discharge region as a means of enhancing plasma uniformity and density.^[29,30]

The induction coil is power supplied by a radio frequency (rf) power source and the power is coupled to (or absorbed in) the plasma through matching networks in order to heat electrons in the plasma. In semiconductor device industry, the frequency usually used is 13.56 MHz, the electrons can follow the instantaneous voltage because the frequency is smaller than an electron plasma frequency ($> \text{GHz}$), while ions cannot because it is larger than an ion plasma frequency (\sim several MHz).^[16] Therefore, the rf power selectively heats the electrons, and in turn, the electrons are not in thermal equilibrium with the ions and neutral gas molecules in the plasma ($T_e \gg T_i \approx T_g$, where T_e , T_i , and T_g are temperatures of electrons, ions, and gases, respectively). The accelerated electrons dissociate and ionize the feed gas molecules through collisions between them to sustain the plasma and generate etchants: for example, in Cl_2 plasmas,



Through these collisions, many etchant species (radicals and ions) can be generated at the same time in the plasma, which is one of the advantages of plasma etching.

Two discharge modes can be observed depending on the rf power desorbed in ICP sources.^[31-33] At low rf power desorbed, the E-mode discharge with a low electron density and a low luminosity of the plasma is dominant, where the electrons are accelerated mainly by the electrostatic fields between powered coil and grounded walls. When the rf power desorbed increases and reaches a certain critical value, the electron density and luminosity of the plasma suddenly increase, which is known as H-mode discharge, where the electrical fields induced by oscillating magnetic fields accelerate the electrons. H-mode discharge is generally used for processing, and in some ICP etchers, E-mode discharge is depressed by using a Faraday shield (not shown in Fig. 1.4).

The wafers to be processed are placed on the stage in the discharge region facing the coil. The stage is capacitively coupled to another rf power source. When the plasma is in contact with solid walls grounded, the electrostatic potential on the wall becomes negative comparing to the plasma potential V_p , as shown in **Fig. 1.5(a)**, because the light electrons more rapidly diffuse to the wall surfaces than heavy ions. The potential drop generates an electric field from the plasma to the wall, and then reflects electrons traveling toward the wall back into the plasma. As the results, thin positively charged layers naturally exist between the plasma and the wall. This region is called sheath. If the rf voltage is applied to the wall (or stage), large electron

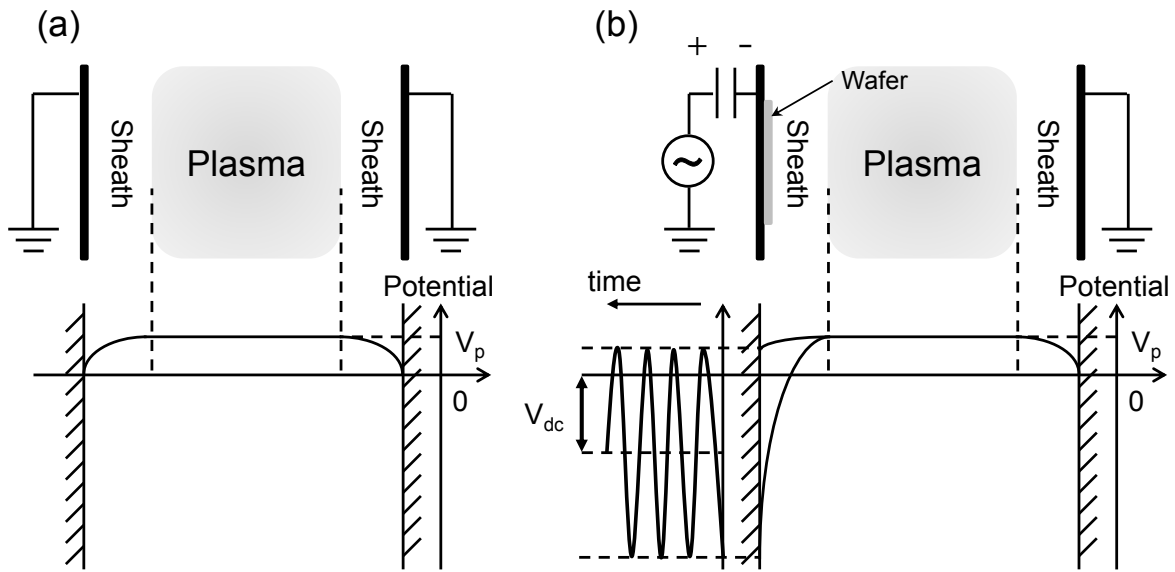


Fig. 1.5. Illustration of potential distributions for two conditions: (a) grounded walls surround the plasma, (b) an rf bias power is applied to the wafer stage.

current flows to the stage during the positive voltage phase. Here, to sustaining charge neutrality of the plasma, ion fluence from the plasma should be balanced with electron one. Therefore, the negative voltage phase must be longer than positive one, and thus, the time-averaged bias voltage on the stage becomes negative, as shown in **Fig. 1.5(b)**. This negative voltage is called dc self-bias voltage (V_{dc}). The magnitude of dc self-bias voltage increases with increasing rf bias power. For a 13.56-MHz power, ions are accelerated toward the stage by the time-averaged voltage, and impact wafer surfaces on the stage with incident energy of $E_i = V_p - V_{dc}$. It is noted here that the E_i is much larger than the thermal energy of ions ($3k_B T_i/2$, where k_B is the Boltzmann constant), and thus, the ions normally incident onto the surfaces. The energetic ion bombardments enable the nonequilibrium processes on the surfaces to be etched, which is another advantage of plasma etching.

1.2.2 Plasma–surface interactions

When reactive neutrals and ions generated in the plasma reach the material surfaces, they react with surface atoms through several kinds of surface reaction kinetics. **Figure 1.6** shows an illustration of surface reactions on substrate surfaces during etching. In the chemical etching

[Fig. 1.6(a)], reactive neutrals (e.g. Cl, Cl₂) chemically react with surface atoms (e.g. Si) and make volatile products, and then the products thermally desorb from the surface: for example,



where (s) and (g) indicate solid and gaseous forms, respectively. This etch process occurs spontaneously and isotropically as in wet etching. The etch rate (or etch yield) depends strongly on the surface temperature.^[34] The etch selectivity, which is the ratio of etch rates of the target material to other materials, is relatively high. In the physical sputtering [Fig. 1.6(b)], surface atoms and/or molecules are received enough kinetic energy (or momentum) from the collision cascade after ion bombardments to overcome surface binding energy.^[35]



This is an anisotropic etch process, but the etch selectivity is low and many lattice damages are generated in the underlying substrates.

Ion-enhanced etching is caused by a combination of chemical reactions by reactive neutrals and physical processes by ion bombardments [Fig. 1.6(c)]. This includes two kinds of mechanism: chemically enhanced physical sputtering and chemical sputtering.^[36] In the former mechanism, absorbed reactive neutrals produce a weakly bound product on the surface and then the product overcomes the surface binding energy force by receiving kinetic energy from collision cascade:



In the latter mechanism, ion bombardment energy causes or allows a chemical reaction to produce a volatile particle and then the product is desorbed thermally:



The etch rate is much higher for the ion-enhanced etching than for the chemical etching and the physical sputtering,^[37] and the anisotropic etching is achieved as in the physical sputtering. Therefore, the ion-enhanced etching is the most important process in plasma etching.

Deposition process is also important in plasma etching [Fig. 1.6(d)]. In this process, etch inhibitors attach and deposit on the surface to be etched. In ICP Cl₂ plasma etching of Si, the etch inhibitors include etch products/byproducts and oxygen coming from quartz windows of the chamber. Here, it is noted that the etch products/byproducts deposited on the surface are removed by the etching process mentioned above, while deposited oxygen is removed only by physical sputtering because it does not react with chlorine. These inhibitors reduce the net etch

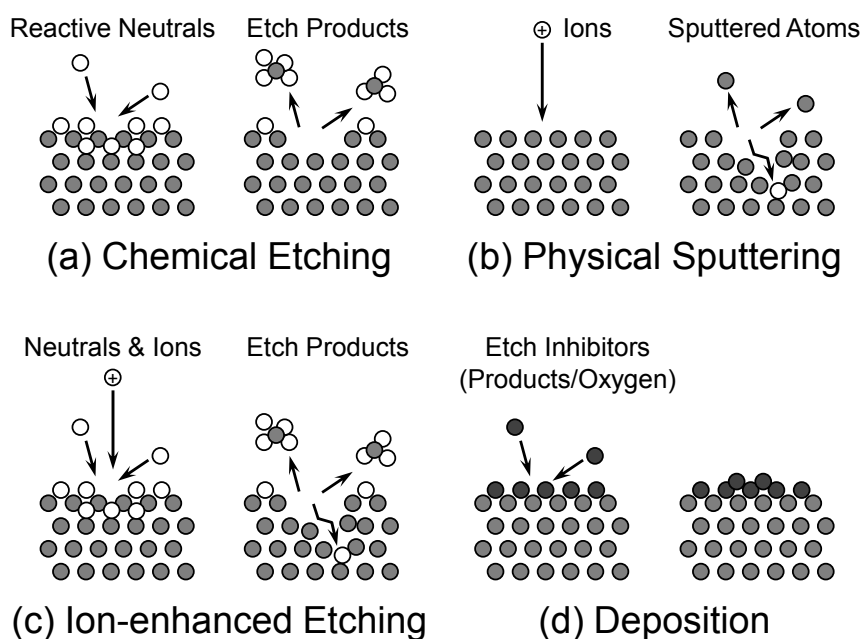


Fig. 1.6. Illustration of surface reactions on substrate surfaces during plasma etching: (a) chemical etching, (b) physical sputtering, (c) ion-enhanced etching, and (d) deposition.

rate; on the other hand, the nature is useful for formation of a passivation layer on feature sidewalls to improve the anisotropy of the etching.

The final feature etched is left as a result of these plasma–surface interactions. **Figure 1.7** shows an illustration of plasma–surface interactions in microstructures during Si etching in ICP Cl_2 plasmas concerned with this study. Reactive neutrals (Cl , Cl_2) and feed gas ions (Cl^+ , Cl_2^+) in the plasmas etch surface atoms (Si) by generating volatile etch products (SiCl_x) in surface reaction layers formed on the bottom of the etched feature. The etch products attaching onto the feature sidewalls form passivation layers thereon, which prevent the sidewalls from being etched. The products diffused to the plasma become etch inhibitors (SiCl_xO_y) and byproduct ions (SiCl_x^+) through the collisions with electrons and neutrals in the plasma, where oxygen atoms come from quartz windows of the chamber; and then these product/byproduct species are reemitted to the substrate surfaces. It should be noted here that the densities and fluxes of the inhibitors and byproduct ions often reach the same degree of or exceed those of the feed gas species during plasma etching. In this case, the plasma–surface interactions become more complex because the surface reaction kinetics is significantly different for between inhibitors/byproduct ions and reactive neutrals/feed gas ions, and in turn, the prediction of the

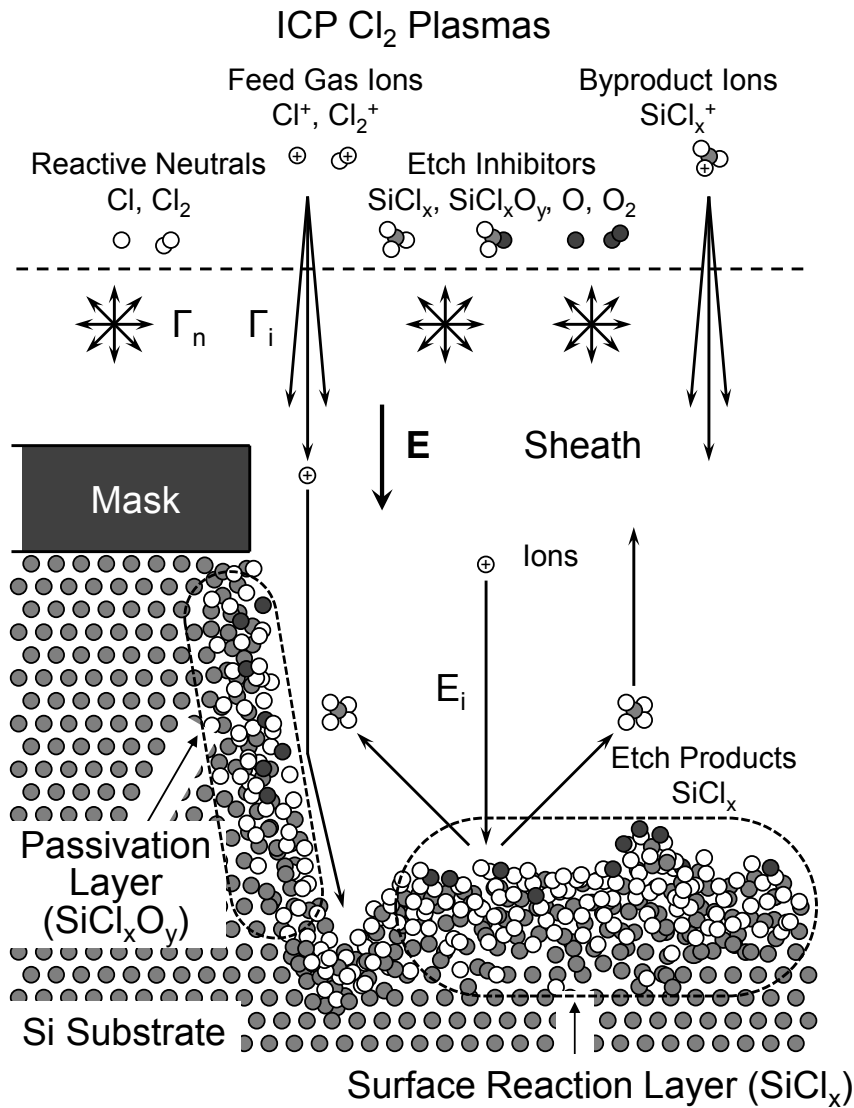


Fig. 1.7. Illustration of plasma–surface interactions in microstructures during Si etching in ICP Cl₂ plasmas, including transportation of reactive neutrals, feed gas ions, etch inhibitors, and byproduct ions, and formation of a surface reaction layer at the feature bottom and a passivation layer on the sidewall, where oxygen atoms come from quartz windows of the chamber.

etched profiles becomes more difficult. Therefore, the precise control of Si etching in Cl- and/or Br-based plasmas is indispensable for the fabrication of gate electrodes and STI of FETs^[3,17] through suppressing profile anomalies of sidewalls and bottom surfaces of the feature.^[38,39] However, the mechanisms are not yet fully understood, so a deeper understanding of the plasma–surface interactions is required.

1.3 Plasma-Induced Surface Roughness

As the device dimensions continue to be scaled down,^[8] increasingly strict requirements are being imposed on plasma etching technology,^[15] including the precise control of profile, critical dimension (CD), and their microscopic uniformity (or aspect-ratio dependence), together with that of etch rate, selectivity, and damage. One of the most important problems to be resolved in the fabrication of nanoscale microelectronic devices is atomic- or nanometer-scale plasma-induced damage and roughness. The effects to device performance have become significant in the course of the miniaturization, where the device scale approaches the size of the damage and roughness.

1.3.1 Overview of plasma-induced damage and roughness

Figure 1.8 shows an illustration of plasma-induced damage and roughness during FET fabrications. Plasma-induced damage occurring inside of the substrate exposed to plasmas has become an important issue, because it directly affects the device performance. The damage can be classified into charging damage, radiation damage, and physical damage.^[40] Charging damage is caused by an electrical stress which originated from the imbalance between electron and ion current from the plasma and the potential difference between the gate electrode and Si substrate, resulting in breakdown of the gate oxide.^[41] Radiation damage is caused by uv radiation from the plasma, which may result in charging and/or electron–hole pair generation.^[42] Physical damage is caused by ion bombardment which generates a damaged layer on the top surface of Si substrate with defect sites including Si vacancies, displaced Si, interstitials, and dangling bonds. The damaged layer removal by wet treatment following plasma etching leaves Si recess structures on the substrate,^[43–45] which causes a shift in threshold voltage of a MOSFET,^[46] and residual defects distributed deeper in the substrate causes a degradation of drain current.^[47,48]

In addition, atomic- or nanometer-scale roughness on etched feature surfaces of Si has become an important issue to be resolved in the fabrication of nanoscale microelectronic devices,^[49–67] because the roughness formed during plasma etching would be comparable with the CD and the thickness of the layer being etched and/or the layer underlying. The nanoscale roughness of etched surfaces of SiO₂,^[62,65,68,69] metal,^[63] metal oxide,^[63] photoresist,^[70–72] polymer/polymeric,^[67,73,74] and low-*k* films^[62,68,75] has also be an issue of great interest similarly.

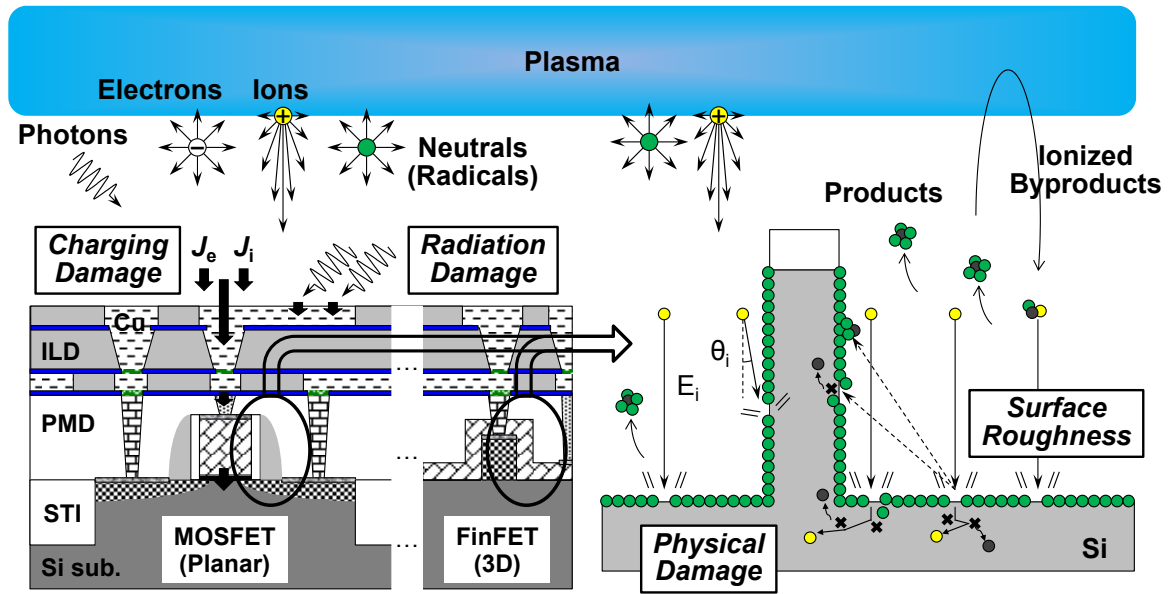
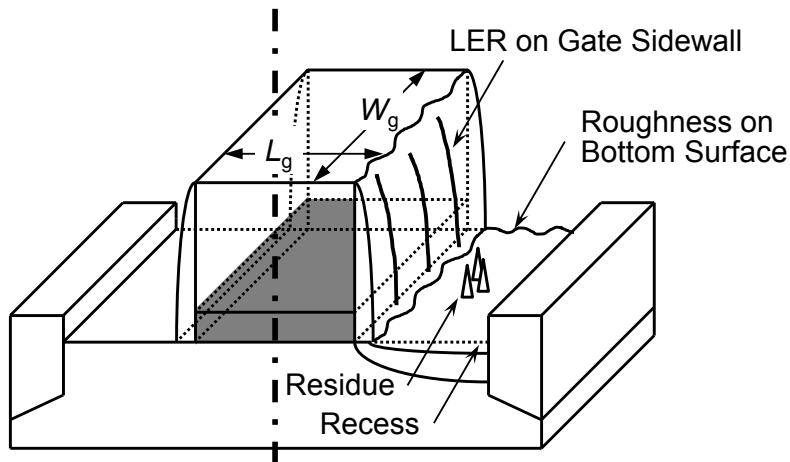


Fig. 1.8. Illustration of plasma-induced damage and roughness during FET fabrications. The damage can be classified into charging damage, radiation damage, and physical damage.

Figure 1.9 shows schematic illustrations of a planar MOSFET and a FinFET with roughness on the feature surfaces. In gate fabrication of MOSFET, the roughness on feature sidewalls is responsible for the line edge roughness (LER) and line width roughness (LWR),^[76,77] which cause the variability in gate or channel length, and thus lead to that in transistor performance.^[78,79] Moreover, in advanced 3D device structures, such as FinFETs,^[15,78,80] the effects of the fin as well as the gate LER and LWR become significant,^[78] because the LER and LWR occur also in fin etch processes,^[15,80] and the conducting channel of FinFETs is formed on top and sidewall surfaces of the fin. The surface roughness and/or residue at the feature bottom affects the uniformity of bottom surfaces, which is responsible for a recess and damage in substrates,^[81] and in turn, also leads to the variability in transistor performance.

The surface roughness formed during plasma etching of Si has also been an important issue in MEMS fabrication processes, although the device dimensions are much larger than those of ULSI devices. In practice, the surface roughness is appreciated to affect the performance of MEMS through the fracture strength of fabricated microstructures^[82] and the friction force between moving microparts.^[83] Additionally, the processing time for etching deep microstructures is significantly long as compared with that in ULSI processes, which in turn

(a) Planar MOSFET



(b) FinFET

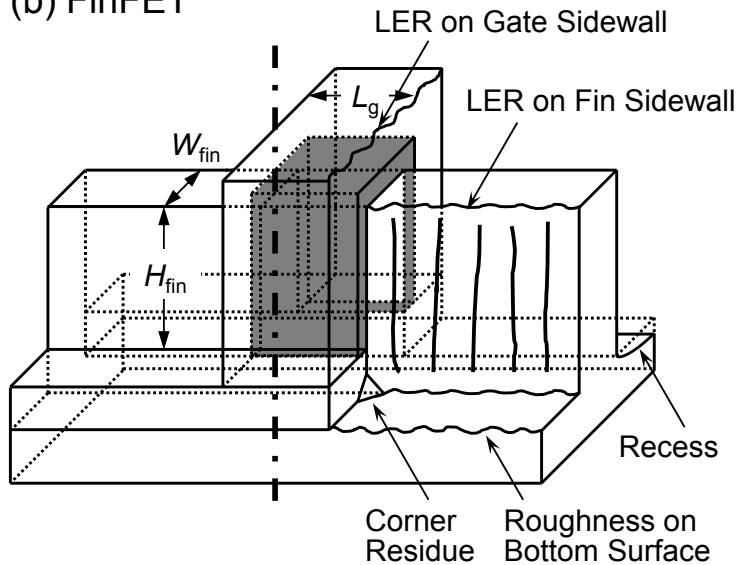


Fig. 1.9. Schematic illustrations of (a) a planar MOSFET with LER on gate sidewall, roughness on bottom surface, residue, and recess, and (b) a FinFET with LER on gate and fin sidewalls, roughness on bottom surface, corner residue, and recess.

would lead to the growth of more significant surface roughness in MEMS processes.

1.3.2 Previous researches on plasma-induced surface roughness

Several experiments have been concerned with the formation and evolution of surface roughness during etching of blank (or planar) Si substrates in SF_6 ,^[50,58,61,64,67] CF_4/O_2 ,^[55] Cl_2 ,^[49,52,63] and

Ar^[62] plasmas, and also in XeF₂ gases with^[59] and without^[53] Ar⁺ ion beams. Correspondingly, several theoretical and/or numerical studies have been made to interpret the roughness observed in plasma etching experiments, using a continuum model,^[54–57] Monte Carlo simulation,^[56,57,60,61,65,67,84–89] and classical molecular dynamics (MD) simulation.^[51,66] The low-level surface roughening at the initial stage of plasma exposure is assumed to be caused by the noise (or stochastic roughening due to the uniformity of incident fluxes of ions and/or neutral etchants on surfaces at microscale);^[54–57,62,65] however, it is not sufficient for interpreting the following evolution of roughness, which has further invoked a few qualitative mechanisms, such as geometrical shadowing,^[54] surface reemission of etchants,^[55–57,60] and effects of etch inhibitors.^[61,67] More generic 3D Monte Carlo simulations have recently been performed to reproduce the surface features roughened in Ar,^[65] SF₆,^[67] and Cl₂/O₂^[86–89] plasma etching of Si, taking into account surface chemistries, such as sputtering and ion-enhanced etching with inhibitor deposition. However, the mechanisms for surface roughening during plasma etching are not yet fully understood, depending on a number of factors in processing.

Moreover, a number of experiments have been concerned with the surface roughness formed on feature sidewalls during plasma etching of patterned Si wafers to understand the origin of LER and LWR, and to find the way of reducing them as much as possible in the fabrication process for microelectronic devices.^[76–80] Sidewall roughening of the feature being etched is assumed to be caused by the pattern transfer of the mask edge roughness (resulting from lithography) into the underlayers being etched and also by that of grain boundaries of polycrystalline films to be etched into themselves.^[76–80] In practice, the addition of depositive gas species such as CF₄ and/or reactive gases such as HBr giving depositive etch byproducts is often invoked to control and suppress the sidewall roughness in poly-Si gate and single-crystalline Si (c-Si) fin fabrication processes,^[76,80] through etch inhibitor deposition or passivation layer formation on feature sidewalls. On the other hand, the sidewall roughness would also be caused by plasma–surface interactions themselves on feature sidewalls, where the ion incidence is assumed to be off-normal or oblique to the surface being etched. However, in plasma etching for pattern definition, it is hard to distinguish the sidewall roughness caused by plasma–surface interactions from that caused by especially the pattern transfer of the mask edge roughness.

Only several studies of Sawin *et al.* have so far been concerned with the sidewall roughening originating from plasma–surface interactions during plasma etching, through

investigations of the effects of the oblique ion incidence on blank substrates: 3D cellular Monte Carlo simulations of Si^[65] and SiO₂^[65,69] etching in Ar and C₄F₈/Ar plasmas, respectively, and the experiments of Ar plasma beam etching of Si, SiO₂, and low-*k* films,^[62] C₂F₆/Ar plasma beam etching of low-*k* films,^[75] and C₄F₈/Ar plasma beam etching of SiO₂^[68,69] and low-*k* films.^[68] Tsuda *et al.* also performed a 3D Monte Carlo simulation concerned with the oblique ion incidence during Cl₂/O₂ plasma etching of Si by using three-dimensional atomic-scale cellular model (ASCeM-3D),^[86–89] and the simulation results revealed the surface roughening and ripple formation in response to ion incidence angle θ_i onto substrate surfaces.^[87,88] Vegh and Graves indicated the ripple formation on Si surface by off-normal CF₃⁺ ion incidence using classical MD simulation.^[66] However, the mechanisms for surface rippling during plasma etching are also not yet fully understood; moreover, the oblique ion incidence and ripple formation during plasma etching are not yet achieved experimentally because of the existence of sheath between the plasma and the surface.

1.4 Structure of This Thesis

This thesis presents details of the experiments concerned with the atomic- or nanometer-scale plasma-induced surface roughness and ripple formation during ICP etching of Si in Cl₂, with attention being placed on a deeper understanding of plasma–surface interactions that are responsible for. Numerical simulations (ASCeM-3D and MD) are also used for interpreting the experimental findings in atomic scale. It is believed that the understandings obtained from this study contribute to developments of a higher-accuracy fabrication process for the next generation devices (**Fig. 1.10**).

In Chapter 2, the apparatus, operation, sample, and diagnostics used in this study are described. Chapter 3 gives the results and discussion for the etching of blank (or planar) Si substrates, where two modes of surface roughening are observed depending on ion incident energy E_i : one is the roughening mode at low E_i , and the other is the smoothing mode at high E_i . In Chapter 4, the possible mechanisms of these modes are proposed from the results of plasma diagnostics during etching and numerical simulations using Monte Carlo-based ASCeM-3D for profile evolution and classical MD for etch fundamentals; here, these simulation methods are described in Appendices A and B, respectively. In Chapter 5, surface smoothing of initially roughened substrates by plasma etching or exposure in the smoothing mode is achieved.

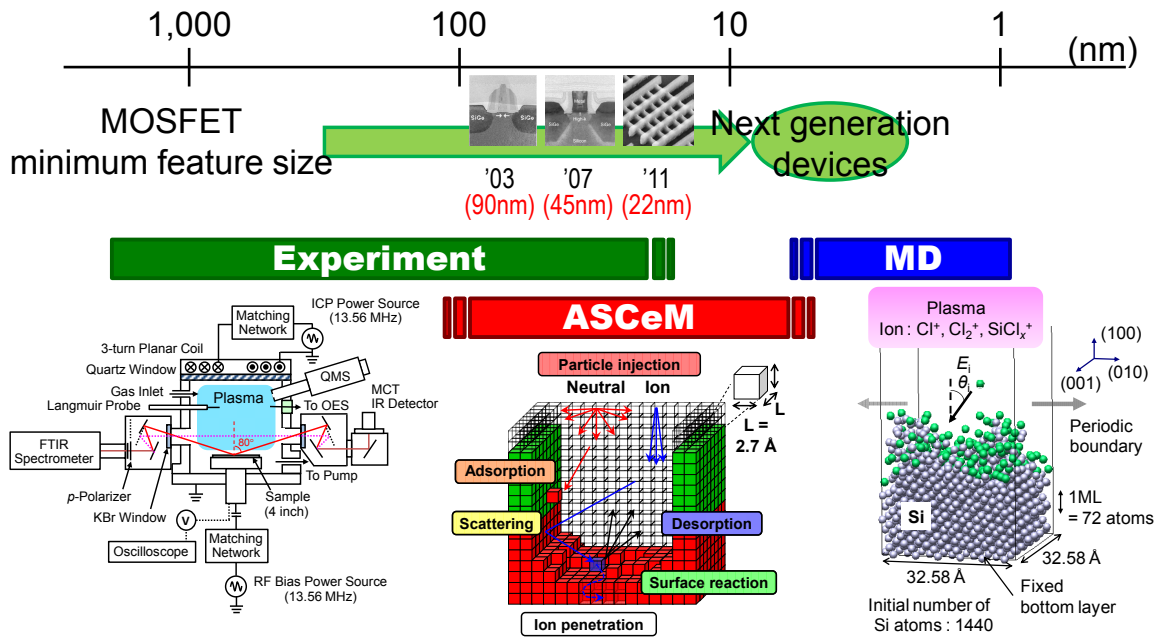


Fig. 1.10. The aim of this study.

Moreover, in Chapter 6, ripple formation by oblique ion incidence during plasma etching is experimentally demonstrated by a sheath control plate used to vary the sheath structures thereon and thus, to vary the ion trajectories onto substrate surfaces. Finally, in Chapter 7, conclusions and future outlooks are mentioned.

Chapter 2

Apparatus, Operation, Sample, and Diagnostics

Nanometer-scale roughness formed on substrate surfaces during plasma etching is caused by temporal and spatial fluctuations of plasma-surface interactions occurring there. The fluctuations and the roughness caused are concerned with many parameters of plasma conditions (feed gas, gas flow rate, pressure, power, etc.), etching conditions (incident neutrals and ions, ion incident energy and angle, etc.), and surface conditions (material, temperature, roughness, etc.). Moreover, the parameters include both macroscopic (centimeter- or millimeter-scale) ones and microscopic (micrometer- or nanometer-scale) ones. Thus, it is difficult to measure and/or consider the whole parameters at the same time. Therefore, the key parameters must be identified from among a number of ones through systematical experiments, to reveal the nanometer-scale plasma–surface interactions and surface roughening mechanisms during plasma etching.

In this study, plasma etching experiments with an ICP reactor were performed for measurements and analyses of nanometer-scale surface roughness on Si substrate caused by

plasma etching in Cl_2 . In addition, several plasma diagnostics were also performed to characterize the plasma at around etched samples position during etching. From these experiments, the relation between plasma conditions and surface roughening on the substrates etched can be obtained. Moreover, to understand and reveal the mechanisms of roughening during etching from the experimental findings, two numerical simulations were performed. The first one is a profile simulation with ASCeM-3D. This can simulate the time evolution of etched feature surface with cell-based model based on Monte Carlo algorithm.^[86–89] The second one is a surface reaction kinetics simulation with classical MD simulation. This solves motions of atoms in substrate surfaces and can determine the etching fundamentals of incident ions.^[90–98] The numerical findings from these simulations can characterize the nanometer-scale phenomena, and thus, explain the mechanisms of surface roughening during plasma etching.

This chapter describes the experimental apparatus, operation, samples, and diagnostics used in this study. In Sec. 2.1, the experimental setup of the ICP reactor used and the typical operation conditions are described. In Sec. 2.2, the plasma and surface diagnostics techniques are mentioned. The simulation models of ASCeM-3D and MD are given in Appendices A and B, respectively.

2.1 Plasma Reactor and Etching Sample

Figure 2.1 shows the experimental setup used in this study. The ICP plasma reactor consists of a stainless-steel chamber 25 cm in diameter and 30 cm high, a three-turn planar coil on a dielectric window at the top, and a 4-in.-diam. electrode or wafer stage at the bottom; the distance between the dielectric window and the wafer is ~ 9 cm in experiments, and the effective volume of the chamber is $V_0 \approx 1.2 \times 10^4 \text{ cm}^3$. The discharge is established by 13.56-MHz rf powers of nominally $P_{\text{ICP}} = 450 \text{ W}$. The wafer stage is capacitively coupled to a 13.56-MHz rf power supply through an impedance matching network for additional rf biasing, where the rf bias power is varied in the range $P_{\text{rf}} = 0\text{--}200 \text{ W}$ to vary the ion incident energy E_i onto substrate surfaces. The reactor chamber is pumped down to a base pressure $< 5 \times 10^{-7}$ Torr by a 1000 l/s turbomolecular pump, and pure Cl_2 gases are introduced therein with the flow rate being varied in the range $F_0 = 5\text{--}50 \text{ sccm}$ (typically 20 sccm). In these experiments, the pressure is kept constant at $P_0 = 20 \text{ mTorr}$ (2.66 Pa) by adjusting the pumping rate with an automatic throttle valve between the chamber and the tubomolecular pump, where the gas residence time

2.2 Plasma and Surface Diagnostics

As shown in Fig. 2.1, several plasma and surface diagnostics are also employed to characterize the plasma at around the wafer position and the surface immersed in the plasma during processing, by using optical emission spectroscopy (OES), quadrupole mass spectrometry (QMS), Langmuir probe measurement, and Fourier transform infrared (FTIR) absorption spectroscopy. Moreover, the etched surfaces are analyzed by using stylus profilometry, atomic force microscopy (AFM), and scanning electron microscopy (SEM). These surface diagnostics were performed with no wafer cleaning after etching in this study.

2.2.1 Optical emission spectroscopy

OES is the most widely used nonintrusive diagnostic technique in plasma etching for monitoring composition of the plasma and/or endpoint detection of processes. The vast majority of optical emission in etching plasmas is a result of electron-impact excitation. Most atomic and diatomic species can be monitored by OES.^[17] Because of the complexity of the excitation mechanism, OES is usually a qualitative technique.

Actinometry is one of the methods which determine quantitative, relative, and absolute species number densities in the plasma.^[99] In this approach, a small amount of a rare gas, A , with an excited state A_k that has an energy close to that of X_k is added to the discharge, and the relative (or, in a few cases, absolute) number density of species X is determined from the ratio of intensity of X_k to A_k . The 750.4 nm line of Ar is used for measurements of the densities of F atom,^[99–104] O atom,^[105,106] and Cl atom.^[107,108] For the measurement of a Cl number density, using the Xe 828.0 or 834.7 nm line provides a much better energy match to the Cl emitting levels, and more consistent tracking of Cl number density than the Ar 750.4 nm line.^[107]

The OES employed in this study a 10-cm focal length spectrometer (Ocean Optics HR2000CG-UV-NIR with a grating of 300 lines/mm and a spectral resolution of 1 nm), where the optical emission spectra of the plasma are observed through a quartz window attached on the chamber sidewalls. **Figure 2.2** shows typical optical emission spectra from Cl₂ plasmas in the absence of etching and during etching. The spectra are dominated by emission from Cl,^[109] Cl₂,^[110–115] and Cl₂⁺,^[110,111,116–118] and, during etching, from Si,^[109] SiCl,^[110,111,119] SiCl₂,^[120–124] SiCl₃,^[125,126] and Si₂.^[110,111,124,127] The wavelengths and transitions for the atomic and molecular emissions concerned are listed in **Table 2.1**.

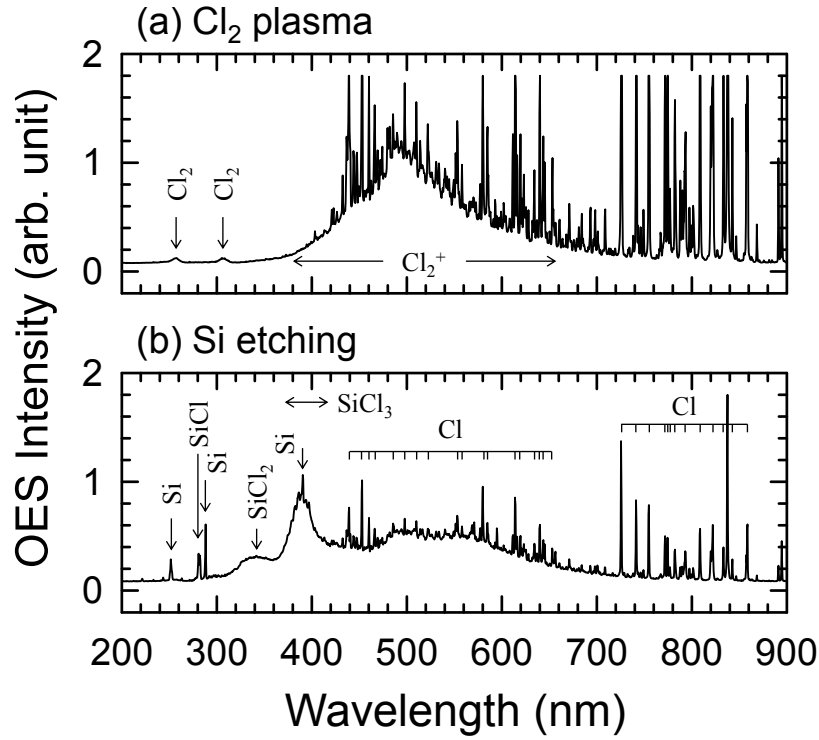


Fig. 2.2. Typical OES spectra in the wavelength range 200–900 nm from ICP Cl_2 plasma (a) in the absence of etching and (b) during Si etching.

Table 2.1. Wavelengths and transitions for atomic and molecular emissions concerned in this study of Cl_2 plasma etching of Si.

Species	Wavelength (nm)	Transition lower–upper	Energy (eV) lower–upper	References
Si	288.1	$3p^2(^1D_2) - 4s(^1P^o_1)$	0.78–5.08 ^(a)	109
SiCl	280.7	$X^2\Pi_r(v'' = 0) - B'^2\Delta(v' = 2)$	0–4.41 ^(b)	110,111,119
SiCl ₂	330	$\tilde{X}^1A_1(v'' = 0) - \tilde{A}^1B_1(v' = 0)$	0–3.76 ^(c)	120–124
SiCl ₂	390	$\tilde{X}^1A_1 - \tilde{A}^1B_1$		121–123
SiCl ₃	390			125,126
Si ₂	390	$X^3\Sigma_g^-(v'' = 0) - H^3\Sigma_u^-(v' = 5)$	0–3.17 ^(d)	110,111,124,127
Cl	837.5	$4s(^4P_{5/2}) - 4p(^4D^o_{7/2})$	8.92–10.40 ^(a)	109
Cl ₂	256.6	$1(^3\Pi_u)[A'^2u(^3\Pi)](v'' = 5) - 2(^3\Pi_g)[D2_g(^3p_2)](v' = 0)$	2.27–7.10 ^(e)	110–115
Cl ₂ ⁺	500.7	$^2\Pi_{3/2}[\tilde{X}^2\Pi_g](v'' = 4) - ^2\Pi_{3/2}[\tilde{A}^2\Pi_g](v' = 0)$	0–2.48 ^(f)	110,111,116–118

^(a) Ref. 109. ^(b) Ref. 111. ^(c) Ref. 122. ^(d) Ref. 127. ^(e) Refs. 113 and 114. ^(f) Refs. 111 and 116.

2.2.2 Quadrupole mass spectrometry

Mass spectrometry is the broadest gas-phase diagnostic method, capable of detecting any neutral or charged species in the plasma. Molecules to be detected enter a small aperture at the chamber wall, pass through the ionizer, and then reach the quadrupole mass spectrometer. Neutral species is detected with ionizer switched on. It is noted that the electron impact energy of the ionizer is high enough to crack the neutrals, and thus, the daughter fragments are detected as well as the parent species. If the cracking patterns for stable species are known, the signals originating in the daughter fragments can be separated from those corresponding to the parent ion of radicals, by recording the signal intensities as a function of the electron impact energy.^[128–130] In addition, it is further noted that in this study, the QMS monitors the species near the chamber wall because the neutral mean free pass λ_n (< 1 cm) is smaller than the chamber diameter (25 cm) under typical condition ($P_0 = 20$ mTorr).

Ions can be directly detected with ionizer switched off, and the intensities give the relative number densities of the ions. Moreover, an ion energy distribution (IED) can be obtained with respect to the mass spectrometer (usually grounded) by sweeping the pass energy with the energy analyzer. The IED is governed by the electron temperature and the product of the ion transit time across the sheath and the frequency of oscillations in the sheath potential.^[16] When it takes many rf cycles for the ion to cross the sheath and no collisions occur, ions will impinge on grounded surfaces with a nearly monoenergetic IED and an energy of the mean sheath potential. Knowing the composition of impinging ions and taking into account the influence of substrate bias, mass spectrometer measurements of ions impacting grounded surfaces at the edge of the plasma can be used to speculate the fluxes of each ion to the sample surface to be etched.^[17]

The QMS employed in this study a quadrupole mass spectrometer with an electrostatic energy analyzer (Hiden HAL EQP 500 with a mass range of $m/e = 1$ –500 amu); the system is differentially pumped down to a base pressure $< 1 \times 10^{-8}$ Torr, and is operated at $< 5 \times 10^{-7}$ Torr in experiments, sampling a portion of the discharge through a 0.1-mm-diam. orifice near the periphery of the wafer stage at ~ 3 cm above the substrate. **Figure 2.3** shows typical QMS spectra measured with the ionizer switched on and off during Cl_2 plasma etching of Si. The spectra are dominated by Si-, Cl-, H-, and O-containing species, where the signals of Si- and Cl-containing species consist of multiple peaks originating from naturally abundant isotopes of Si (^{28}Si , ^{29}Si , ^{30}Si) and Cl (^{35}Cl , ^{37}Cl).

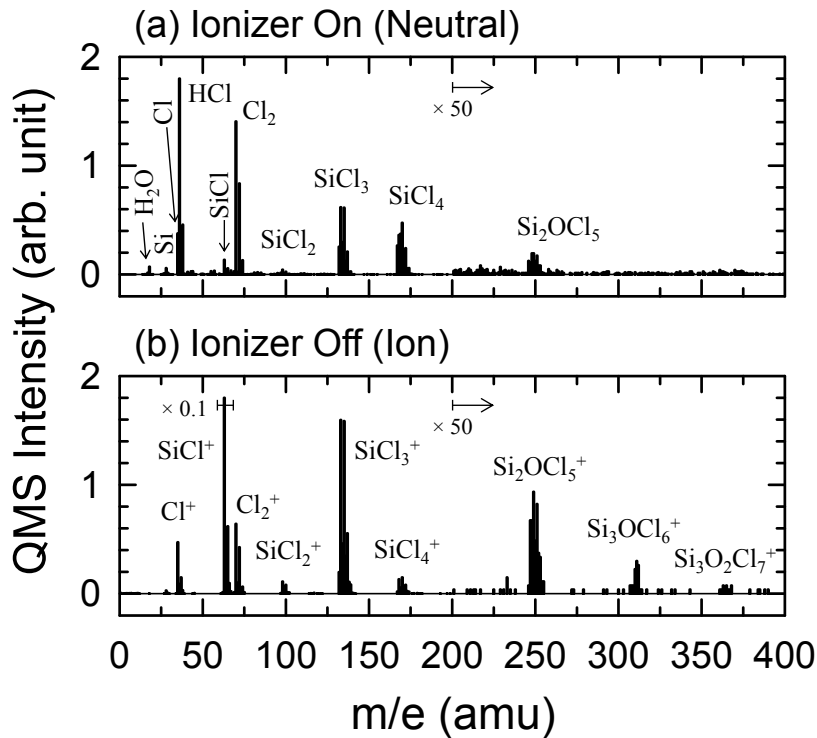


Fig. 2.3. Typical QMS spectra in the mass range $m/e = 1\text{--}400$ amu during ICP plasma etching of Si in Cl_2 , measured with the ionizer (using 70-eV electrons) switched (a) on and (b) off. The spectra are dominated by Si-, Cl-, H-, and O-containing species, where the signals of Si- and Cl-containing species consist of multiple peaks originating from naturally abundant isotopes of Si (^{28}Si , ^{29}Si , ^{30}Si) and Cl (^{35}Cl , ^{37}Cl).

2.2.3 Langmuir probe

A metal probe or Langmuir probe is one of the earliest and still one of the most useful tools for plasma diagnostics, which is inserted in the plasma and biased positively or negatively to draw electron or ion current.^[131] Probes immersed in a plasma produce only minor local perturbations of the plasma, because the probes are much smaller than large electrodes surrounding and controlling the plasma. From the analysis of voltage–current curve measured by the probe, electron density n_e and temperature T_e , ion density n_i and temperature T_i , and plasma potential V_p are obtained.

The Langmuir probe used in this study has a cylindrical tungsten tip 0.5 mm in diameter and 10 mm long, which is positioned horizontally at ~ 3 cm above the center of the substrate. In addition, taking into account the dc self-bias voltage V_{dc} at wafer stage being routinely

monitored by a voltage probe, the ion incident energy $E_i = V_p - V_{dc}$ onto substrates also can be obtained.

2.2.4 Fourier transform infrared absorption spectroscopy

FTIR absorption spectroscopy is utilized to observe etch-related chemical species, such as Si-containing etch products and/or byproducts, in the plasma and also on substrate surfaces.^[132,133]

In this study, the IR optical system consists of an FTIR spectrometer (Thermo Nicolet iS50R with a KBr beam splitter), which is reconfigured for the probe beam to pass through the reactor chamber located outside of the optical bench of the instrument; the system is being purged with dry nitrogen gases to remove the residual carbon dioxide and water vapor therein. In transmission absorption spectroscopy (TAS) for observation of species in the gas phase, the IR beam from the FTIR bench is directed through 4-cm-diam. KBr optical flats into the chamber, ~3 cm above the substrate parallel to its surface. The TAS spectra are observed in single-pass operation with an absorption path length of $l \approx 25$ cm in the chamber, and changes of the IR beam intensity due to the absorption are detected with a liquid-nitrogen-cooled MgCdTe (MCT) detector placed ~40 cm apart from the exit KBr window. In reflection absorption spectroscopy (RAS) for observation of species on the surface, the IR beam from the FTIR bench is passed through a thallium-bromide-iodide (KRS-5) polarizer, and the *p*-polarized beam is then focused onto substrate surfaces, where the RAS spectra are observed in single reflection mode at an incident angle of 80°.

In both of these observations, the FTIR data are recorded in the wavenumber range 4000–450 cm^{-1} at a resolution of 2 or 4 cm^{-1} by averaging over 250–500 scans (taking ~4–8 min), and the Happ–Genzel apodization is applied to the interferogram before carrying out the Fourier transform. Background or reference spectra are collected in the presence of feed gas flows with a wafer being in place on the stage; the sample spectra are then taken with the discharge switched on (or during etching), where the noise level in the spectra is not affected seriously by operating the discharge. The absorbance spectrum is determined by calculating $-\ln(I/I_0)$ as a function of wavenumber, where I and I_0 are the IR beam intensities at the detector corresponding to the sample and reference spectra, respectively. **Figure 2.4** shows typical absorbance spectra measured by FTIR-TAS in the absence of etching and during etching. Here, the peak absorbance of interest is that of SiCl_4 at around 620 cm^{-1} (ν_3 fundamental vibrational

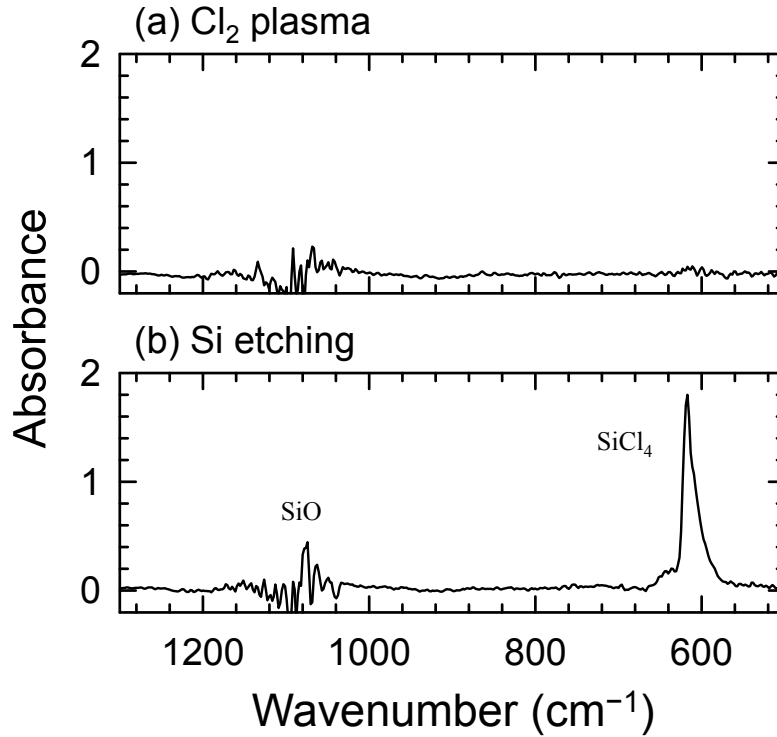


Fig. 2.4. Typical absorbance spectra in the wavenumber range $1300\text{--}500\text{ cm}^{-1}$, measured by FTIR-TAS from ICP Cl_2 plasma (a) in the absence of etching and (b) during Si etching.

band);^[132–134] in addition, the spectra exhibits a weak absorption of SiO at around 1100 cm^{-1} .^[111,132–135] In this study, to derive the absolute concentration of etch product/byproduct neutrals SiCl_4 in the plasma during etching, the calibration was made by filling the ICP reactor chamber with pure SiCl_4 gases at different pressures in the range $P_0 = 0.05\text{--}50\text{ mTorr}$ without discharge.

2.2.5 Stylus profilometry

The sub-micrometer-scale etched surface feature can be measured by stylus profilometry. In this study, the etched depth (d_{etch}), defined as the difference in height after etching between the parts of the sample covered by a mask (h_0) and those uncovered (h_{etch}), is measured by stylus profilometry (Veeco Dektak 6M), where a polyimide film and/or a piece of Si wafer are placed on a sample as a mask during etching. The etch rate is calculated by dividing the etched depth by the etching time

$$\text{ER} = d_{\text{etch}}/t_{\text{etch}} = (h_0 - h_{\text{etch}})/t_{\text{etch}} . \quad (2.1)$$

2.2.6 Atomic force microscopy

The nanometer-scale roughness on the surface can be measured by AFM, which is one of the scanning probe microscopy. In this study, the etched surfaces are examined by AFM (Shimadzu SPM-9600), in tapping mode typically on a scan area of $W_A^2 = 1 \times 1 \mu\text{m}^2$ with the resolution of $N^2 = 256 \times 256$ pixels and a scan rate of 1 Hz, using a microfabricated Si cantilever with a tip radius less than 10 nm. The surface images are depicted from the two-dimensional (2D) data of height or depth (or ordinate) distribution $z(x, y)$. In addition, to evaluate the roughness quantitatively, the root-mean-square (rms) surface roughness is calculated from the rms average or standard deviation of the surface feature ordinates from their mean value

$$\text{RMS} = \sqrt{\frac{1}{N^2} \sum_{m=1}^N \sum_{n=1}^N [z(m, n) - z_{\text{ave}}]^2} , \quad (2.2)$$

where (m, n) denotes the location of the pixel in (x, y) coordinates, and z_{ave} is the arithmetic average of the z value within the surface area of W_A^2 concerned:

$$z_{\text{ave}} = \frac{1}{N^2} \sum_{m=1}^N \sum_{n=1}^N z(m, n). \quad (2.3)$$

To further characterize the roughened surface features, the power spectral density (PSD) distribution as well as rms roughness of feature surfaces is important,^[50,63,64] because the rms surface roughness reflects only the vertical extent of the feature, while the PSD gives the information on both its vertical and lateral (or spatial) extent. In the PSD analysis, the one-dimensional (1D) PSD function along the x axis is calculated from 1D discrete Fourier transform (DFT) of the 1D surface height or depth distribution $z(x, n)$ and averaged over $n = 1-N$

$$P_x(k_x) = \frac{1}{N} \sum_{n=1}^N \left[\left| L_A \sum_{m=1}^N z(m, n) \cdot \exp(-2\pi i \Delta k_x m) \right|^2 \right], \quad (2.4)$$

where i is the imaginary unit, k_x is the spatial frequency in the x -direction, and $L_A = W_A/N$ is the sample distance. 1D PSD function along the y axis $P_y(k_y)$ is also calculated in a similar fashion, where k_y is the spatial frequency in the y -direction. The 1D PSD function has a unit of fourth power to the length. On the other hand, The angular averaged 1D PSD is obtained by the calculation of the 2D PSD function from the 2D DFT of the 2D surface height or depth

distribution^[136–139]

$$P(k_x, k_y) = \frac{1}{W_A^2} \left| L_A^2 \sum_{m=1}^N \sum_{n=1}^N z(m, n) \cdot \exp[-2\pi i L_A (k_x m + k_y n)] \right|^2, \quad (2.5)$$

and the following transition to polar coordinates in frequency space and angular averaging

$$P(k) = \frac{1}{2\pi} \int_0^{2\pi} P_{\text{po}}(k, \varphi) d\varphi, \quad (2.6)$$

where $P_{\text{po}}(k, \varphi)$ is the 2D PSD distribution in (k, φ) coordinates.^[136,139] This angular averaged 1D PSD depends on only one parameter, while it is plotted as a slice of the 2D representation, where it remains a 2D function with a unit of fourth power to length.^[139]

2.2.7 Scanning electron microscopy

In this study, surface images corresponding to the AFM images are also taken by using SEM (JEOL JSM-7500FA). The electron acceleration voltage and current are 15 kV and 10 μA , respectively, and the SEM images are obtained by the detection of secondary electron from sample surfaces.

Chapter 3

Two Modes of Surface Roughening during Plasma Etching of Silicon

This chapter presents details of the experimental results concerned with the nanoscale surface roughening during Si etching in ICP Cl₂ plasmas. Experiments were performed as a function of rf bias power by varying the feed gas flow rate, wafer stage temperature, and etching or plasma exposure time. The experimental setup used is detailed in Chapter 2. The roughness of etched surfaces was quantified by the rms roughness and also in some cases by the PSD distribution to gain information relative to both vertical and lateral extent of it. We observed two modes of surface roughening during plasma etching, roughening and smoothing (or non-roughening) modes, depending on bias power or ion incident energy onto substrate surfaces. The roughening mode may be unavailable in industry. However, studying the mechanisms responsible for the roughening as well as smoothing modes is important in industry as well as in research, because of the following two reasons: a better understanding of the mechanisms for the roughening mode is indispensable for finding the way how to suppress and/or control the evolution of the surface roughness during plasma exposure, because the roughening mode may

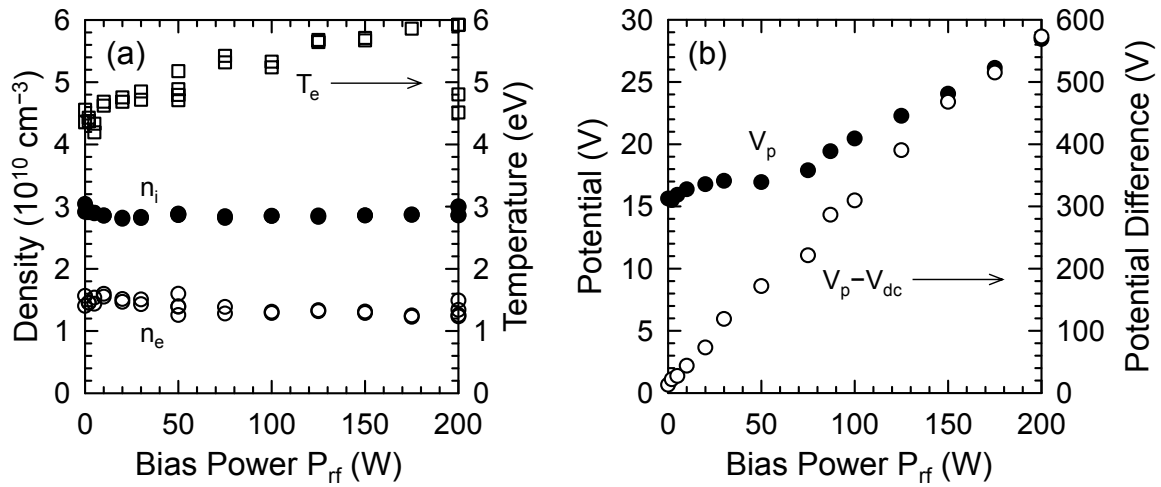


Fig. 3.1. Plasma parameters as a function of rf bias power P_{rf} , measured by Langmuir probes during ICP plasma etching of Si in Cl_2 under typical operating conditions of $P_{ICP} = 450 \text{ W}$, $P_0 = 20 \text{ mTorr}$, $F_0 = 20 \text{ sccm}$, and $T_s = 20^\circ\text{C}$: (a) electron density n_e and temperature T_e , and positive ion density n_i ; (b) plasma potential V_p and potential difference $V_p - V_{dc}$, where V_{dc} is the dc self-bias voltage at the wafer stage, and $E_i = V_p - V_{dc}$ is a measure of the ion incident energy onto substrate surfaces.

be used unconsciously in industry as well as research. The roughening mode may also be used, in some cases, to positively obtain roughened surfaces, or to obtain surface nanostructures, such as nanotextures, nanograsses, nanopillars, and nanocolumns.^[67]

3.1 Plasma Parameters

Figure 3.1 shows the plasma parameters as a function of rf bias power in the range $P_{rf} = 0\text{--}200 \text{ W}$, measured by Langmuir probes during ICP plasma etching of Si in Cl_2 under typical operating conditions of $P_{ICP} = 450 \text{ W}$, $P_0 = 20 \text{ mTorr}$, $F_0 = 20 \text{ sccm}$, and $T_s = 20^\circ\text{C}$: electron density n_e and temperature T_e , positive ion density n_i , plasma potential V_p , and potential difference $V_p - V_{dc}$. The probe data were analyzed assuming an effective ion mass $m_{i,\text{eff}} = \sum_j \chi_j m_j$, where the concentration fraction χ_j of the ion species j with a mass m_j was determined by QMS for each condition. The results indicate that the ion n_i and electron n_e densities remain almost unchanged over the P_{rf} range investigated, while the electron temperature T_e increases slightly with increasing P_{rf} . The corresponding ion flux concerned (or the ion saturation

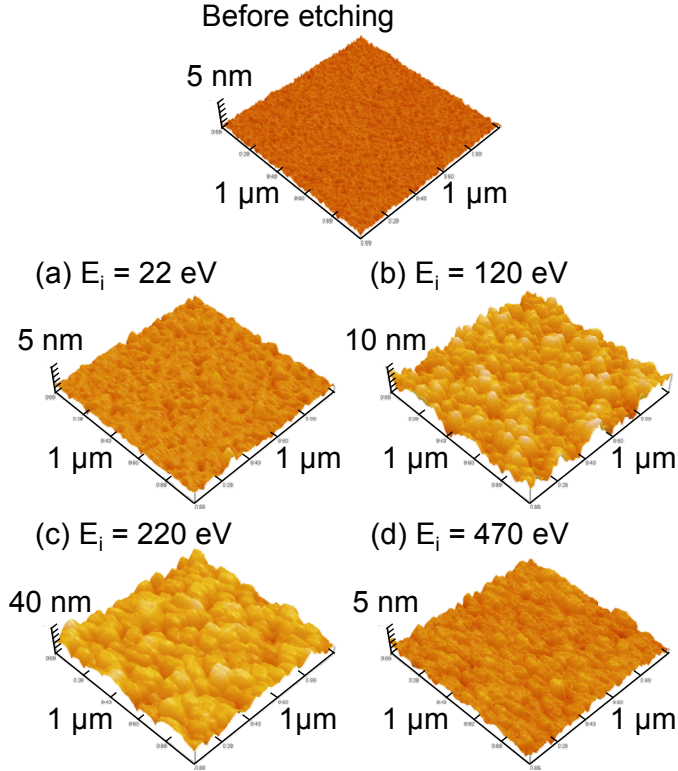


Fig. 3.2. Typical AFM images of the Si surfaces etched in ICP Cl_2 plasmas for $t_{\text{etch}} = 2$ min with four different ion incident energies of $E_i \approx$ (a) 22, (b) 120, (c) 220, and (d) 470 eV under the same conditions as in Fig. 3.1. Inset is an image of wet-cleaned Si surfaces prior to etching for reference.

current to the probe measured) remains almost constant at $\Gamma_i^0 = 0.61n_i(k_B T_e/m_{i,\text{eff}})^{1/2} \approx (0.5\text{--}0.6) \times 10^{16} \text{ cm}^{-2}\text{s}^{-1}$,^[16] where k_B is the Boltzmann constant. Moreover, the plasma potential V_p remains almost unchanged at low P_{rf} , while it increases slightly with increasing $P_{\text{rf}} > 50$ W, corresponding to an increase in T_e . The potential difference $V_p - V_{\text{dc}}$ increases with increasing P_{rf} , owing to the dc self-bias voltage V_{dc} decreased, giving an ion incident energy in the range $E_i \approx 13\text{--}570$ eV for $P_{\text{rf}} = 0\text{--}200$ W. It is noted here that the potential V_p was consistent with the ion energy distribution measured by QMS (not shown), and that the probe data did not depend significantly on gas flow rate F_0 and stage temperature T_s , as well as on the wafer resistivity.

3.2 Etch Rate and Surface Roughness

Figure 3.2 shows typical AFM images of the Si surfaces etched in ICP Cl_2 plasmas for $t_{\text{etch}} = 2$ min with four different ion incident energies of $E_i \approx 22\text{--}470$ eV under the same conditions as in Fig. 3.1. Inset is an image of wet-cleaned Si surfaces prior to etching ($t_{\text{etch}} = 0$) for reference. These surface images and the data on the rms surface roughness were acquired in tapping mode

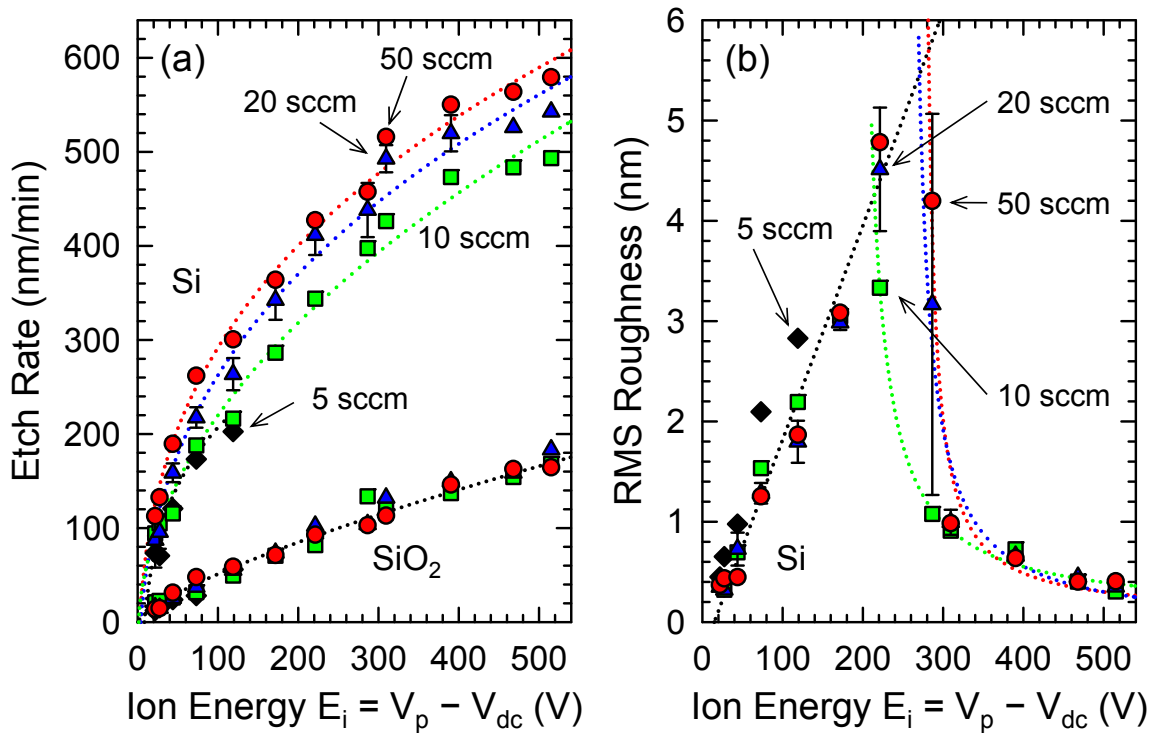


Fig. 3.3. (a) Etch rates of Si and SiO₂ and (b) rms surface roughness of Si as a function of ion incident energy in the range $E_i \approx 22\text{--}520$ eV, obtained in ICP Cl₂ plasma etching ($t_{\text{etch}} = 2$ min) for four different gas flow rates of $F_0 = 5, 10, 20$ and 50 sccm under otherwise the same conditions as in Fig. 3.1. The rms roughness shown is that measured for the AFM scan area of $1 \times 1 \mu\text{m}^2$ as in Fig. 3.2, and the dotted lines are for guiding the eyes only. Note that the experiments for $F_0 = 5$ sccm were restricted to low $E_i < 120$ eV, because the present system with $P_0 = 20$ mTorr and $F_0 = 5$ sccm starves for feed gases at higher E_i , owing to increased Si etch rates.

on a scan area of $1 \times 1 \mu\text{m}^2$ with the resolution of 256×256 pixels and a scan rate of 1 Hz, using a microfabricated Si cantilever with a tip radius less than 10 nm. The AFM images indicate that as the bias power P_{rf} or ion energy E_i is increased, the roughness of etched Si surfaces increases and then decreases.

Figure 3.3 shows the etch rates of Si and SiO₂ and the rms surface roughness of Si as a function of ion incident energy in the range $E_i \approx 22\text{--}520$ eV, obtained in ICP Cl₂ plasma etching ($t_{\text{etch}} = 2$ min) for four different gas flow rates of $F_0 = 5, 10, 20$, and 50 sccm under otherwise the same conditions as in Fig. 3.1. The error bars (shown typically for $F_0 = 20$ sccm) represent the variation in the raw data for more than ten etching experiments using sample wafers with different as well as similar resistivities and cleaning recipes. Note that the experiments for F_0

= 5 sccm were restricted to low $E_i < 120$ eV, because the present system with $P_0 = 20$ mTorr and $F_0 = 5$ sccm starves for feed gases at higher E_i , owing to increased Si etch rates; in practice, the amount of Si etched per minute is estimated to be $(\rho_s ER)S \approx 8.1 \times 10^{19}$ atoms/min for an etch rate $ER = 200$ nm/min of a 4-in.-diam. wafer, corresponding to an inflow rate ≈ 3.0 sccm (1 sccm = 2.686×10^{19} atoms or molecules/min at standard conditions), where ρ_s is the Si atom density and S is the surface area of substrates. The results indicate that for any F_0 , as the bias power P_{rf} or ion energy E_i is increased, the Si and SiO₂ etch rates increase, and the etch selectivity of Si over SiO₂ decreases; on the other hand, the rms roughness of etched Si surfaces increases, peaks at around $E_i = E_p \approx 200$ – 300 eV (depending slightly on F_0), and then decreases substantially down to a low level < 0.4 nm. Thus, it follows that in these experiments, the roughness scales with the etch rate at low $E_i < E_p$, while it does not scale with the etch rate at higher $E_i > E_p$. The increase followed by the decrease in surface roughness with increasing P_{rf} or E_i has so far not been observed in plasma etching experiments of Si: some experiments showed an increase in roughness as well as etch rate with P_{rf} in Cl₂ plasma,^[52] some other experiments showed a decrease in roughness with P_{rf} in SF₆ plasma,^[50] with E_i in the range 20–100 eV in SF₆ plasma,^[64] and with E_i in the range 100–250 eV in Cl₂ plasma,^[63] in contrast to an increase in etch rate.

Moreover, at a given P_{rf} or E_i in Fig. 3.3, the Si etch rate and the selectivity tend to be slightly increased for increased flow rates F_0 , while the SiO₂ etch rate does not depend significantly on F_0 , as has been known to be due to reduced concentrations of etch products/byproducts in the plasma during high-gas-flow-rate or short-gas-residence-time plasma etching of Si.^[140] On the other hand, the rms surface roughness of Si appears to be almost independent of F_0 at low $E_i < 200$ eV and high $E_i > 300$ eV, although the ion energy E_p giving a peak of the rms roughness, together with its peak value, tends to be slightly increased for increased F_0 .

Figure 3.4 shows the etch rates of Si and SiO₂ as a function of the square root $E_i^{1/2}$ of the ion incident energy for four different gas flow rates F_0 , which are the data replotted from the preceding Fig. 3.3(a). The results indicate that for any F_0 , both the Si and SiO₂ etch rates are approximately proportional to $E_i^{1/2}$, which reflects the universal energy dependence of the yield for ion bombardment-induced etch processes such as physical sputtering and ion-enhanced etching.^[141–143] $Y = \rho_s ER / \Gamma_i^0 = A(E_i^{1/2} - E_{th}^{1/2})$, where the yield Y is defined as the total number of Si atoms desorbed from substrate surfaces per ion impact, the Si atom density of substrates is

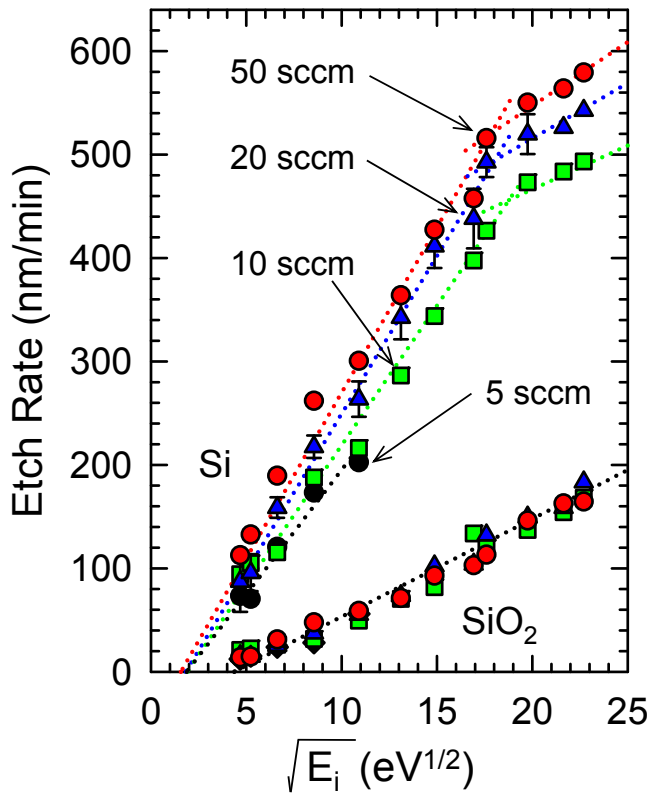


Fig. 3.4. Etch rates of Si and SiO₂ as a function of the square root of the ion incident energy for four different gas flow rates F_0 , which are the data replotted from the preceding Fig. 3.3(a). The dotted lines are linear fits to guide the eyes.

$\rho_s \approx 5.0$ and $2.2 \times 10^{22} \text{ cm}^{-3}$ for Si and SiO₂, respectively,^[2] Γ_i^0 is the ion flux incident on substrate surfaces, A is a proportional constant or scaling factor, and E_{th} is the threshold energy concerned. The linear dependence of the yield Y on $E_i^{1/2}$ implies that the etching is limited by the momentum transfer from energetic ions to substrate atoms through the collision-cascade mechanism.^[141–143] In the present experiments, the ion flux $\Gamma_i^0 \approx (0.5–0.6) \times 10^{16} \text{ cm}^{-2}\text{s}^{-1}$ does not change significantly with E_i (as mentioned earlier with respect to Fig. 3.1), and so the etch rate ER should also be proportional to $E_i^{1/2}$. The threshold is estimated to be $E_{\text{th}} \approx 4$ and 20 eV for Si and SiO₂, respectively, by extrapolating the ER to zero, being almost independent of flow rate F_0 and in agreement with previous plasma etching experiments in Cl₂.^[144] Moreover, the Si etch yield is estimated to be typically $Y \approx 1.3–7.3$ (ER $\approx 80–440$ nm/min) at ion energies in the range $E_i \approx 20–300$ eV, giving the factor $A \approx 0.46$ in $\text{eV}^{-1/2}$, where the Y and thus A depends slightly on F_0 in these experiments. The A factor presently estimated compares relatively well with previous plasma etching experiments of Si in Cl₂ plasmas ($A \approx 0.275$ in Ref. [145], and 0.353 in Ref. [146]). In addition, the SiO₂ etch yield is estimated to be $Y \approx 0.11–1.2$ (ER \approx

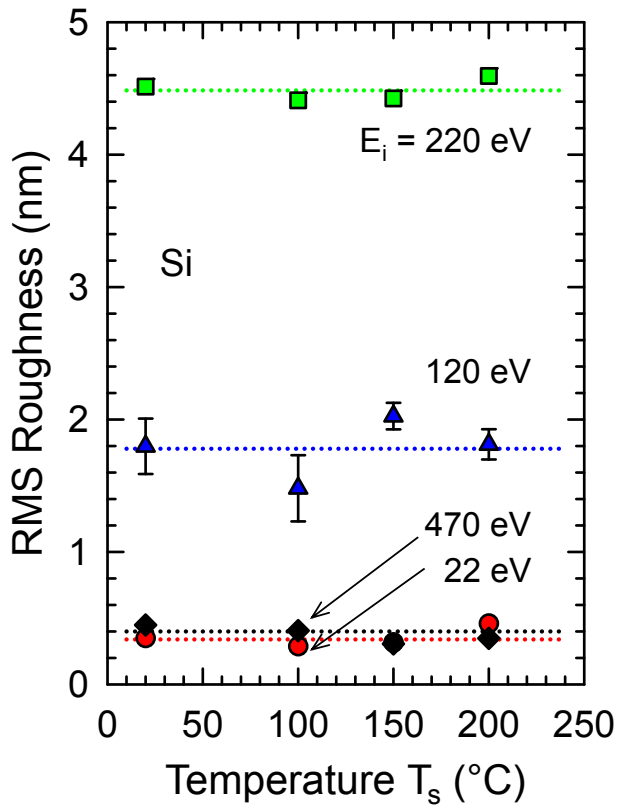


Fig. 3.5. RMS surface roughness of Si as a function of wafer stage temperature in the range $T_s = 20\text{--}200^\circ\text{C}$, obtained under otherwise the same conditions as in Fig. 3.1, in ICP Cl_2 plasma etching ($t_{\text{etch}} = 2$ min) for four different ion incident energies of $E_i \approx 22\text{--}470$ eV. The dotted lines are for guiding the eyes only.

15–160 nm/min) at $E_i \approx 20\text{--}500$ eV, being almost independent of F_0 .

It is further noted in Fig. 3.4 that for any F_0 , the curve of ER or Y versus $E_i^{1/2}$ for Si exhibits a transition point at around $E_i \approx 300\text{--}400$ eV, above which the Y or ER increases more slowly with increasing E_i , although it remains nearly proportional to $E_i^{1/2}$; in practice, the slope or proportional constant A of the curve is estimated to decrease by about a factor of 2–3 above the transition point, implying some change in reaction kinetics on surfaces being etched. A comparison between Figs. 3.3(b) and 3.4 indicates that for Si, the ion energy E_p giving the peak rms roughness corresponds roughly to the transition point for the Y or ER versus $E_i^{1/2}$ curve, although the latter tends to be slightly decreased for increased flow rates F_0 , and the latter is a little higher than the former by about $\Delta E_i \approx 50\text{--}150$ eV.

Figure 3.5 shows the rms surface roughness of Si as a function of wafer stage temperature in the range $T_s = 20\text{--}200^\circ\text{C}$, obtained under otherwise the same conditions as in Fig. 3.1, in ICP Cl_2 plasma etching ($t_{\text{etch}} = 2$ min) for four different ion incident energies of $E_i \approx 22\text{--}470$ eV. The error bars (shown typically for $E_i \approx 120$ eV) have the same properties as those in Fig. 3.3.

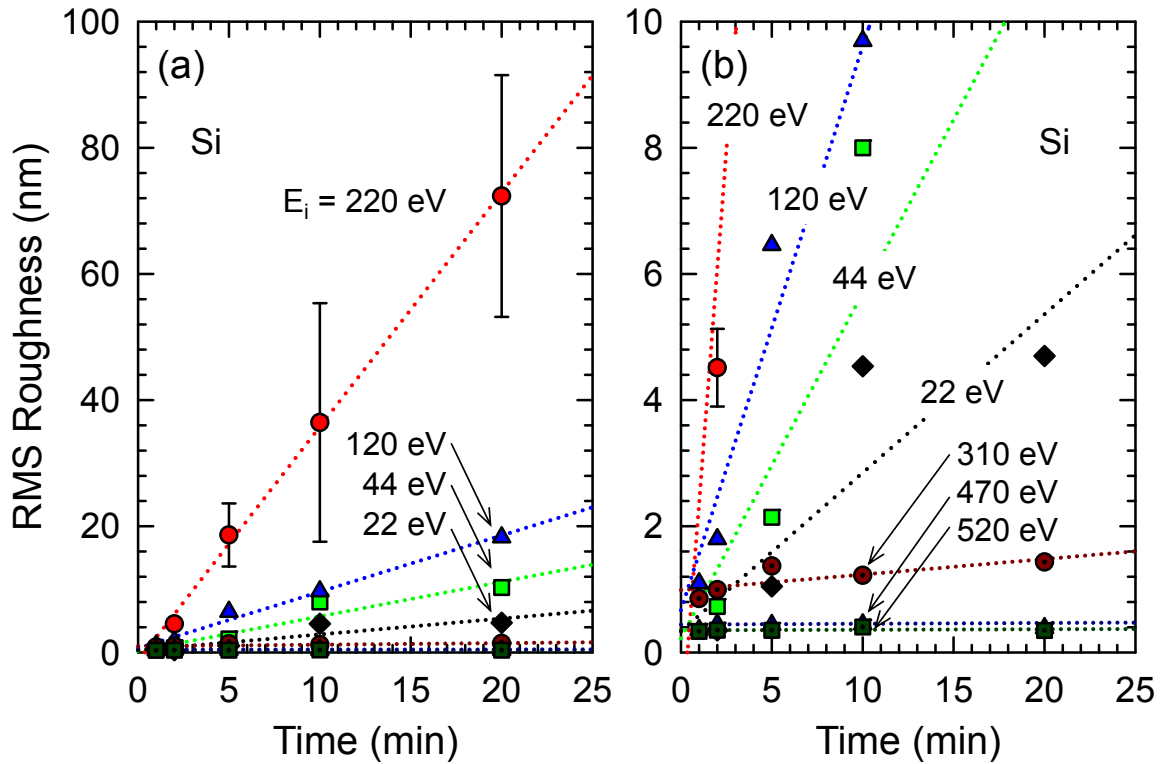


Fig. 3.6. RMS surface roughness of Si as a function of etching or plasma exposure time in the range $t_{\text{etch}} = 1\text{--}20$ min, obtained in ICP Cl_2 plasma etching for seven different ion incident energies of $E_i \approx 22\text{--}520$ eV under the same conditions as in Fig. 3.1. The vertical scale (rms roughness) of the figure ranges from (a) 0 to 100 nm and (b) 0 to 10 nm. The dotted lines are for guiding the eyes only.

The results indicate no significant T_s dependence of the roughness of etched Si surfaces, as well as the Si and SiO_2 etch rates (not shown), although the temperature T_s is expected to modify the surface reaction kinetics during etching. No T_s dependence of both the roughness and etch rate has been observed in plasma etching experiments of Si in SF_6 for $T_s \approx -100\text{--}40^\circ\text{C}$.^[50] This may be attributed partly to the wafer surface temperature that is often different from the stage temperature T_s (usually measured by a thermocouple attached to the stage) during plasma etching; in practice, the surface temperature during etching was measured to be higher than T_s by using FTIR-RAS (increasing with increasing P_{rf} or E_i).^[147]

Figure 3.6 shows the rms surface roughness of Si as a function of etching or plasma exposure time in the range $t_{\text{etch}} = 1\text{--}20$ min, obtained in ICP Cl_2 plasma etching for seven different ion incident energies of $E_i \approx 22\text{--}520$ eV under the same conditions as in Fig. 3.1. The

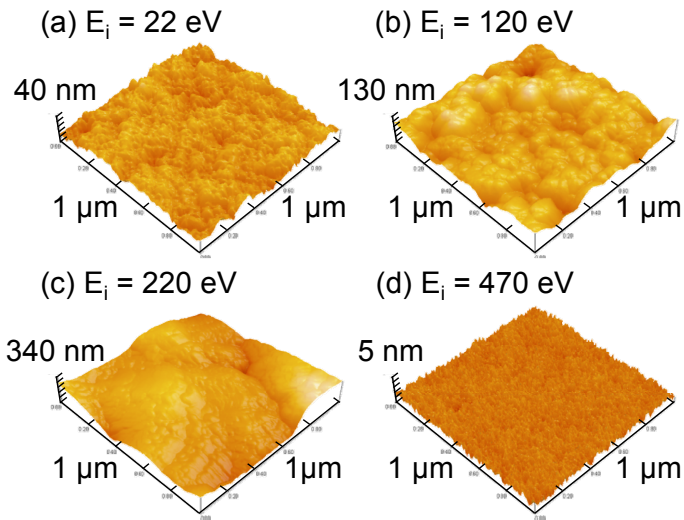


Fig. 3.7. Typical AFM images of the Si surfaces etched in ICP Cl_2 plasmas for $t_{\text{etch}} = 20$ min with four different ion incident energies of $E_i \approx$ (a) 22, (b) 120, (c) 220, and (d) 470 eV under the same conditions as in Fig. 3.1. These images are compared with those for $t_{\text{etch}} = 2$ min in Fig. 3.2.

error bars (shown typically for $E_i \approx 220$ eV) have the same properties as those in Fig. 3.3. Typical AFM images of the Si surfaces etched for $t_{\text{etch}} = 20$ min are also shown in **Fig. 3.7** for reference, which are compared with those for $t_{\text{etch}} = 2$ min in Fig. 3.2. The results indicate that at low $E_i < E_p$ (≈ 250 eV for $F_0 = 20$ sccm), the rms roughness of etched surfaces increases almost linearly with time during etching, where the higher the E_i , the larger is the increase in roughness; in particular, at $E_i \approx 220$ eV, the rms roughness reaches an extraordinarily large value of > 70 nm at $t = 20$ min. In contrast, at higher $E_i > E_p$, the roughness tends to reach quasi-steady state after some increase at the initial stage of etching ($t < 1$ min), where the higher the E_i , the smaller is the roughness at steady state; in particular, at $E_i > 470$ eV, the rms roughness remains at a low level < 0.4 nm, which is only a little larger than the initial value of ~ 0.15 nm prior to etching. It is noted here that over the P_{rf} or E_i range investigated, the etched depth increased almost linearly with time, or the etch rate reached quasi-steady state soon after the start of etching (not shown); thus, it follows that in these experiments, the roughness evolution does not follow that of the etch rate at low $E_i < E_p$. The increase in surface roughness with time during etching, along with quasi-steady etch rates, has been observed in several plasma etching experiments of Si in SF_6 ^[50,61,64,67] and CF_4/O_2 ^[55] while the low-level, quasi-steady roughness has not been reported so far.

Figure 3.8 shows typical SEM images of the time evolution of the Si surfaces etched in ICP Cl_2 plasmas ($t_{\text{etch}} = 1$ –20 min) with four different ion incident energies of $E_i \approx 22$ –470 eV under the same conditions as in Fig. 3.1. Also shown are the images of wet-cleaned Si surfaces prior to etching ($t_{\text{etch}} = 0$) for reference. These SEM images were found to be consistent

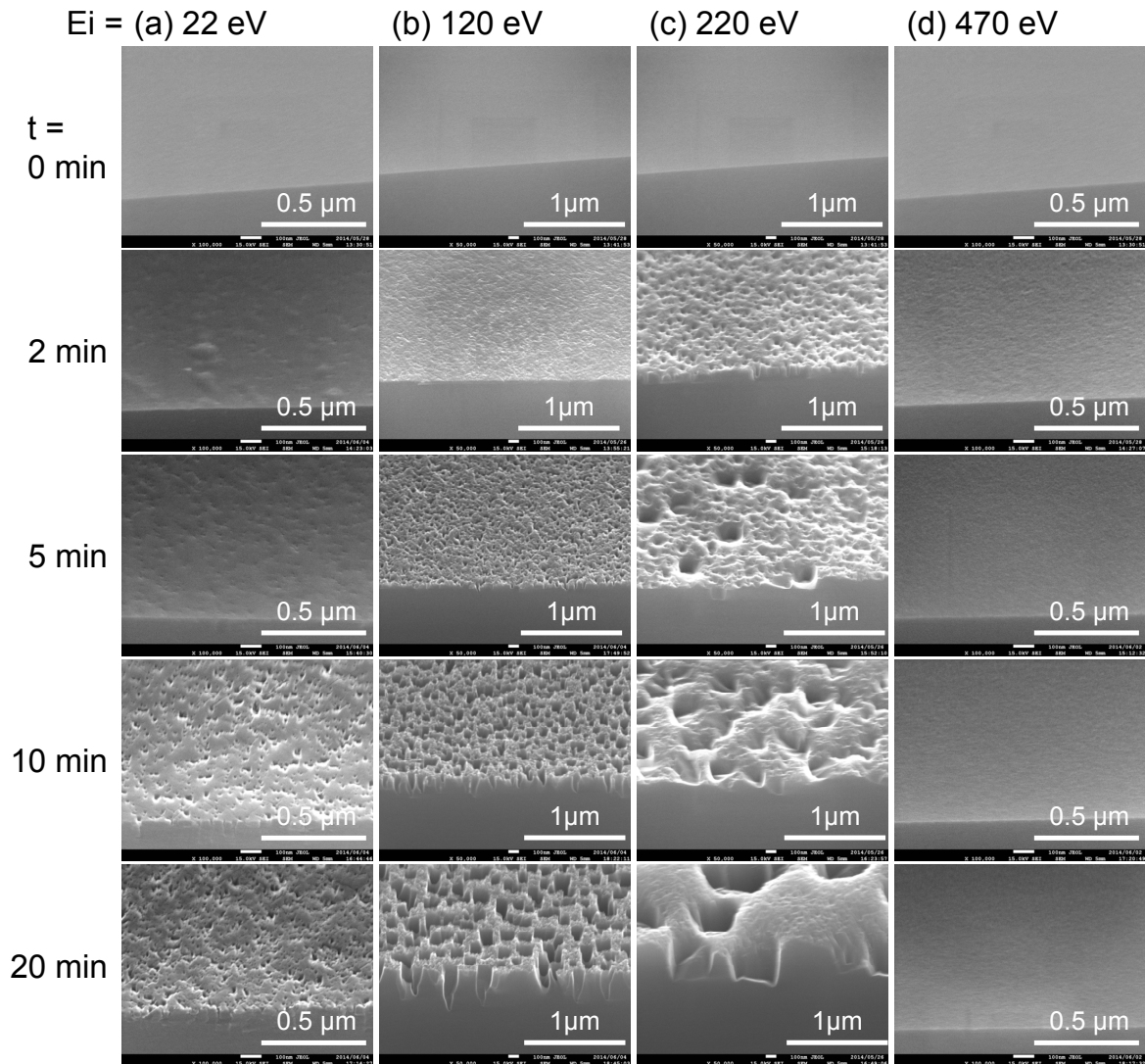


Fig. 3.8. Typical SEM images of the time evolution of the Si surfaces etched in ICP Cl_2 plasmas ($t_{\text{etch}} = 1\text{--}20$ min) with four different ion incident energies of $E_i \approx$ (a) 22, (b) 120, (c) 220, and (d) 470 eV under the same conditions as in Fig. 3.1. Also shown are the images of wet-cleaned Si surfaces prior to etching ($t_{\text{etch}} = 0$) for reference.

visually with the corresponding AFM images (e.g., Figs. 3.2 and 3.7 for $t_{\text{etch}} = 2$ and 20 min), and also with the data of the rms surface roughness measured therefrom [Figs. 3.3(b) and 3.6]: at low $E_i < E_p$ (≈ 250 eV), the surface roughness continues to evolve with time, where the higher the E_i , the more significant is the evolution of roughness, and the roughness at $E_i \approx 220$ eV becomes extraordinarily large in lateral as well as vertical extent at $t = 20$ min. In contrast, at higher $E_i > E_p$, the roughness tends to reach quasi-steady state soon after the start of etching, remaining low at $E_i > 470$ eV. Thus, we may consider that in these experiments, the evolution

of the rms roughness of etched surfaces shown in Fig. 3.6 fully reflects that of the degree of the surface roughness concerned, although the AFM is generally assumed to be no longer appropriate to measure a large rms roughness > 20 nm.

Hence, it is concluded that there are two modes of surface roughening during plasma etching of Si in Cl_2 , which occur depending on rf bias power P_{rf} or ion incident energy E_i : one is the roughening mode at low $E_i < E_p$ ($\approx 200\text{--}300$ eV), where the rms roughness of etched surfaces increases with increasing E_i , scaling with the etch rate (Fig. 3.3), and the etch rate ER or etch yield Y versus $E_i^{1/2}$ curve exhibits a relatively large slope or proportional constant (Fig. 3.4); in this mode, the rms roughness increases almost linearly with time during etching (Fig. 3.6), while the etch rate reaches quasi-steady state soon after the start of etching. The other is the smoothing or non-roughening mode at higher $E_i > E_p$, where the rms surface roughness decreases substantially with increasing E_i down to a low level at $E_i \gg E_p$, not scaling with the etch rate (Fig. 3.3), and the ER or Y versus $E_i^{1/2}$ curve exhibits a decreased proportional constant (Fig. 3.4); in this mode, the rms roughness tends to reach quasi-steady state after some increase at the initial stage of etching (Fig. 3.6), where the roughness evolution follows that of the etch rate in a sense. In the present experiments, the transition from roughening to smoothing modes is sharp with increasing P_{rf} or E_i ; and the transition point E_p for the rms roughness versus E_i curve appears to correspond to that for the ER or Y versus $E_i^{1/2}$ one, although the former is a little lower than the latter by about $\Delta E_i \approx 50\text{--}150$ eV [Figs. 3.3(b) and 3.4].

3.3 Power Spectral Density of Surface Roughness

To further characterize the roughened surface features, the PSD distribution as well as rms roughness of feature surfaces is important,^[50,63,64,88] because the rms surface roughness reflects only the vertical extent of the feature, while the PSD gives the information on both its vertical and lateral (or spatial) extent. In the PSD analysis, the 2D PSD function is calculated from the 2D-DFT of the 2D surface height or depth distribution;^[137,139] the 1D PSD function is then obtained by angularly averaging the 2D-PSD, retaining a 2D function with a unit of fourth power to the length, as mentioned in Sec. 2.2.6.

Figure 3.9 shows the time evolution of the angularly averaged PSD distribution $P(k)$ for three different ion incident energies of $E_i \approx 120, 310,$ and 470 eV, obtained from the PSD analysis of AFM images of the Si surfaces etched in ICP Cl_2 plasmas ($t_{\text{etch}} = 1\text{--}20$ min) as

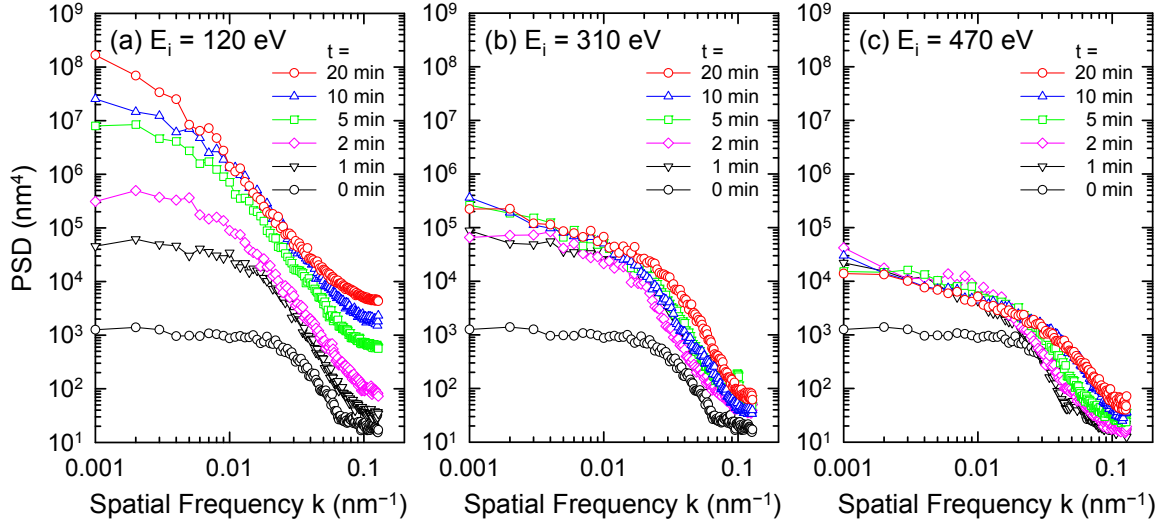


Fig. 3.9. Time evolution of the angularly averaged PSD distribution $P(k)$ for three different ion incident energies of $E_i \approx$ (a) 120, (b) 310, and (c) 470 eV, obtained from the PSD analysis of AFM images of the Si surfaces etched in ICP Cl_2 plasmas ($t_{\text{etch}} = 1\text{--}20$ min) as shown in Figs. 3.2 and 3.7. Also shown is the PSD distribution of wet-cleaned Si surfaces prior to etching ($t_{\text{etch}} = 0$) for reference.

shown in Figs. 3.2 and 3.7. Also shown is the PSD distribution of wet-cleaned Si surfaces prior to etching ($t_{\text{etch}} = 0$) for reference. These $P(k)$ evolutions correspond to the two modes of surface roughening as mentioned above with respect to Figs. 3.3, 3.4, and 3.6. The length scale concerned is the side length $W_A = 1 \mu\text{m}$ of the AFM scan area with the resolution of 256 pixels (a pixel size $L_A = 3.9 \text{ nm}$), which corresponds to the spatial frequency ranging from $k = 0.001$ to 0.128 nm^{-1} in the reciprocal space. It is generally appreciated that for the PSD curve, the parameters of interest are:^[50,63,64,88] the plateau height value w_0 at low k related to the vertical height or depth of roughened surface features [$P(k) \approx w_0$ at $k < k_0$], and the correlation length ζ_0 ($= 1/k_0$) that defines the lateral size of the roughness; moreover, the curve at high k gives a fractal or self-affine nature of the roughness [$P(k) \approx K/k^\eta$ at $k > k_0$],^[139,148–151] where K is the spectral strength, the exponent η is a constant linked to the fractal dimension of the surface, and ζ_0 defines the upper limit of the scale where the surface exhibits the self-affine nature.

The PSD analysis indicates that at $E_i \approx 120 \text{ eV}$ (roughening mode), the plateau value w_0 and correlation length ζ_0 increase monotonically with time during etching, corresponding to the increase in both vertical and lateral roughness; in particular, the correlation length as well as the rms surface roughness increases almost linearly with time (from $\zeta_0 \approx 50 \text{ nm}$ at $t = 0$ to $\approx 200 \text{ nm}$

at $t = 10$ min), as has been observed in several plasma etching experiments of Si in SF_6 ^[50,61] and CF_4/O_2 .^[55] Note that the w_0 and ξ_0 tend to become unclear at $t > 10$ min, probably because the lateral size of the increased roughness tends to exceed the limit length scale $W_A = 1 \mu\text{m}$ or its reciprocal $k = 0.001 \text{ nm}^{-1}$ of the present AFM scan area. Moreover, the $P(k)$ tail at high frequencies ($k > k_0 = 1/\xi_0$) exhibits a slight increase in spectral strength K during etching, when the fractal-linked constant remains almost unchanged at $\eta \approx 3$ (marginal fractal).^[139] Similar evolution of $P(k)$ was observed for different ion energies $E_i < E_p$ (≈ 250 eV), where for a given t_{etch} , the w_0 , ξ_0 , and K values are increased at increased E_i , while that of η remains almost the same. These imply that in the roughening mode, the increase in surface roughness with time during etching arises primarily from an increase in height/depth of low-frequency (or long-wavelength) components, without a significant change in height/depth of high-frequency (or short-wavelength) ones; in effect, the frequency independent regime at low frequencies is attributed to the evolution of hole-like microstructures, evident visually in SEM images of Fig. 3.8, which are randomly situated and separated by roughly similar intervals, and which obviously increase in lateral size as well as vertical depth with time during etching. On the other hand, the high frequency self-affine regime is attributed to the low-level, stochastic roughening originating intrinsically from the temporal as well as spatial uniformity of the incident flux and angle of ions and/or neutral reactants on surfaces at microscale.^[54–57,62,65,88]

In contrast, the evolutions of $P(k)$ at $E_i \approx 310$ and 470 eV (smoothing mode) exhibit markedly different behavior: the $P(k)$ curve remains almost unchanged over time during etching ($t > 1$ min), after some change at the initial stage of etching ($t < 1$ min); concretely, the correlation length ($\xi_0 \approx 50$ nm) remains almost the same as that of wet-cleaned surfaces prior to etching ($t_{\text{etch}} = 0$), and the $P(k)$ tail at high frequencies ($k > k_0 = 1/\xi_0 \approx 0.02 \text{ nm}^{-1}$) remains similar to that of the wet-cleaned surfaces with a fractal-linked constant $\eta \approx 3$, although the $P(k)$ tail exhibits a little increase in spectral strength K with time during etching. On the other hand, at low frequencies ($k < k_0$), the $P(k)$ magnitude increases slightly at the initial stage of etching, and it remains almost unchanged thereafter; then, the plateau value w_0 becomes unclear, and the $P(k)$ curve exhibits a second self-affine surface, remaining almost unchanged with a second spectral strength K' and fractal constant $\eta' \approx 1$ (extreme fractal).^[139] Such multiple self-affine surfaces have been observed in thin film deposition experiments, being correlated to the formation and evolution of film microstructures.^[148–151] Similar evolution of $P(k)$ was observed for different ion energies $E_i > E_p$ (≈ 250 eV), where for a given t_{etch} , the K and K'

values are decreased at increased E_i , while those of ζ_0 , η , and η' remain almost the same, as can be seen from a comparison between the $P(k)$ evolutions at $E_i \approx 310$ and 470 eV. These imply that in the smoothing mode, only the low-level, stochastic roughening occurs on surfaces after some increase in roughness at the initial stage of etching, where the two self-affine fractal regimes at low and high frequencies are attributed to the stochastic roughening associated with the incoming flux of ionic species of different natures for surface reaction kinetics, as will be discussed below in Sec. 4.1 and Sec. 4.2.

3.4 Summary

Atomic- or nanometer-scale surface roughness on etched surfaces has been investigated during Si etching in ICP Cl_2 plasmas. Experiments were performed at a constant pressure ($P_0 = 20$ mTorr) as a function of rf bias power or ion incident energy in the range $E_i \approx 20$ –500 eV, by varying the feed gas flow rate ($F_0 = 5$ –50 sccm), wafer stage temperature ($T_s = 20$ –200°C), and etching or plasma exposure time ($t_{\text{etch}} = 1$ –20 min). The experiments revealed two modes of plasma-induced surface roughening which occur depending on E_i : roughening and smoothing (or non-roughening) modes. In roughening mode at low $E_i < E_p \approx 200$ –300 eV (depending slightly on F_0), the rms roughness of etched surfaces as well as the etch rate increases with increasing E_i , where the etch rate or yield versus $E_i^{1/2}$ curve exhibits a relatively large slope or proportional constant; moreover, the rms roughness increases almost linearly with time during etching ($t < 20$ min), where the higher the E_i , the larger is the increase in roughness. The roughness evolution with time does not follow that of the etch rate at low $E_i < E_p$, because the etch rate reaches quasi-steady state soon after the start of etching in the whole E_i range investigated. On the other hand, in the smoothing mode at higher $E_i > E_p$, the rms surface roughness decreases substantially with increasing E_i down to a low level < 0.4 nm (initially ~ 0.15 nm), while the etch rate continues to increase with E_i , where the etch rate or yield versus $E_i^{1/2}$ curve exhibits a decreased proportional constant; moreover, the rms roughness tends to reach quasi-steady state after some increase at the initial stage of etching ($t < 1$ min), where the higher the E_i , the smaller is the roughness at steady state.

Correspondingly, the power spectral density analysis exhibited two different behaviors of the roughness evolution: the spectral distributions in the roughening mode consist of a frequency independent regime at low spatial frequencies and a high frequency self-affine regime,

where the plateau value and the correlation length increase with time during etching, with the fractal-linked exponent remaining almost unchanged at $\eta \approx 3$; on the other hand, the spectral distributions in the smoothing mode consist of two self-affine regimes at low and high frequencies, where the distributions remain almost unchanged over time ($t > 1$ min) during etching with the fractal exponents of $\eta \approx 1$ and 3.

Chapter 4

Role of Ionized Etch Products for Surface Roughening

In Chapter 3, experiments found two modes of surface roughening which occur depending on E_i : one is the roughening mode at low $E_i < 200\text{--}300$ eV, where the rms roughness of etched surfaces increases with increasing E_i , exhibiting an almost linear increase with time during etching ($t < 20$ min). The other is the smoothing mode at higher E_i , where the rms surface roughness decreases substantially with E_i down to a low level < 0.4 nm, exhibiting a quasi-steady state after some increase at the initial stage ($t < 1$ min). Correspondingly, two different behaviors depending on E_i were also observed in the etch rate versus $E_i^{1/2}$ curve, and in the evolution of the PSD distribution of surfaces. These results imply that the plasma–surface interactions change with increasing E_i .

This chapter presents details of the experiments concerned with the plasma diagnostics during Si etching in ICP Cl_2 plasmas, with attention being placed on the plasma characterization. Experiments were performed under the same conditions as in Chapter 3. The plasma was monitored qualitatively by OES; in addition, SiCl_4 concentration in the plasma and incoming

flux of ions were measured quantitatively by FTIR and QMS, respectively. Moreover, possible mechanisms for the formation and evolution of surface roughness are discussed with the help of ASCeM-3D and classical MD simulations, where effects of the changes in the predominant ion flux caused by increased etch rates at increased E_i are taken into account as observed in experiments.

4.1 Etch Products and Byproducts

4.1.1 Optical emission spectroscopy

Figure 4.1 shows typical OES spectra in the wavelength range 200–900 nm during ICP plasma etching of Si in Cl_2 , observed for four different ion incident energies of $E_i \approx 22\text{--}470$ eV under typical operating conditions of $P_{\text{ICP}} = 450$ W, $P_0 = 20$ mTorr, $F_0 = 20$ sccm, and $T_s = 20^\circ\text{C}$ (the same conditions as in Fig. 3.1). Also shown is an OES spectrum from the Cl_2 plasma in the absence of etching ($P_{\text{rf}} = 0$ W or $E_i \approx 13$ eV without breakthrough step) for reference. In the uv range, atomic lines and molecular bands originating from etch products and/or byproducts become more significant at increased P_{rf} or E_i , corresponding to the increase in etch rate as shown in Fig. 3.3(a) and the resultant increase in their concentration in the plasma:^[115,125,126,152] SiCl bands identified at 280.7 and 282.3 nm,^[110,111,119] a broad band of SiCl_2 around 330 nm,^[120–124] and another broad one of SiCl_2 ,^[121–123] SiCl_3 ,^[125,126] or Si_2 ^[110,111,124,127] around 390 nm, together with Si lines at 251.6, 288.1, and 390.5 nm.^[109] It is noted here that in this study, etch byproducts mean Si-containing species (ions and neutrals) formed through ionization, dissociation, and/or reaction of etch products (primary products) after being desorbed from substrate surfaces during etching. In contrast, spectral lines and bands originating from feed gases become less significant at increased P_{rf} or E_i , corresponding to reduced partial pressures or concentrations of feed gases under the operating conditions of constant pressure P_0 : weak Cl_2 emission bands identified at 256.6 and 306.3 nm in the uv,^[110–115] and broad, prominent bands of Cl_2^+ extending from 380 to 660 nm in the visible,^[110,111,116–118] together with numerous Cl lines (strong peaks at 438.9, 452.6, 579.6, and 614.0 nm)^[109] superimposed thereon, and those in the near-ir range (strong peaks at 725.6, 741.4, 754.7, 837.5, and 858.5 nm).^[109] The Cl^+ ion lines in the visible were not identified in the present experiments, owing to relatively low electron temperatures T_e as compared to ECR plasmas operated at $P_0 < 1$ mTorr.^[132,133,152]

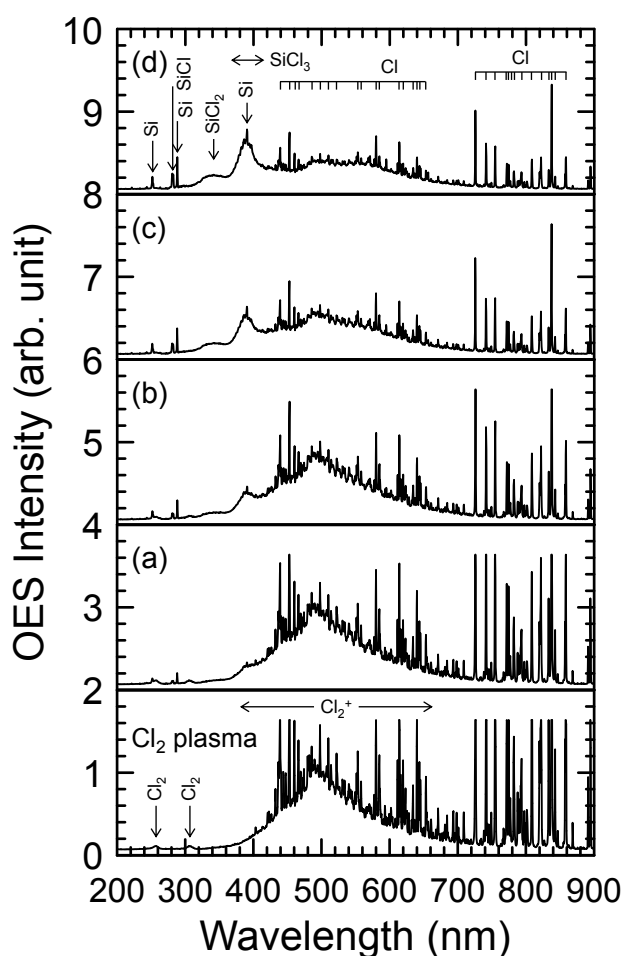


Fig. 4.1. Typical OES spectra in the wavelength range 200–900 nm during ICP plasma etching of Si in Cl_2 , observed for four different ion incident energies of $E_i \approx$ (a) 22, (b) 120, (c) 220, and (d) 470 eV under typical operating conditions of $P_{\text{ICP}} = 450$ W, $P_0 = 20$ mTorr, $F_0 = 20$ sccm, and $T_s = 20^\circ\text{C}$ (the same conditions as in Fig. 3.1). Also shown is an OES spectrum from the Cl_2 plasma in the absence of etching ($P_{\text{rf}} = 0$ W or $E_i \approx 13$ eV without breakthrough step) for reference.

Figure 4.2 shows the OES intensities of seven species SiCl_x ($x = 0\text{--}3$), Cl_x ($x = 1, 2$), and Cl_2^+ as a function of ion incident energy in the range $E_i \approx 13\text{--}570$ eV, measured during ICP plasma etching of Si in Cl_2 under the same conditions as in Fig. 4.1. The wavelengths and transitions for the atomic and molecular emissions concerned are listed in Table 2.1. Note that the actinometry^[153] with a small amount of inert gas (actinometer) added to feed gases was not employed in these measurements, because at increased P_{rf} or E_i , the amount of Si etched per minute is increased and comparable to that of feed gases (as mentioned earlier with respect to Fig. 3.3); thus, the partial pressure of feed gases and so the concentration of the actinometer in the plasma is decreased at increased P_{rf} or E_i , where the optical emission intensity ratio of the target species to the actinometer would not be related to the species concentration therein. In the present experiments, the raw emission intensity was assumed to represent qualitatively the

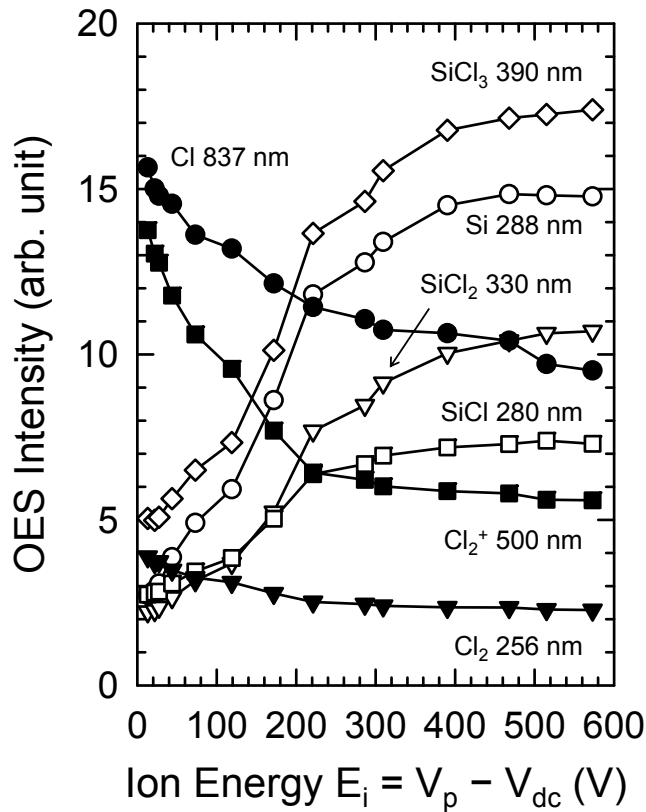


Fig. 4.2. OES intensities of seven species SiCl_x ($x = 0-3$), Cl_x ($x = 1, 2$) and Cl_2^+ as a function of ion incident energy in the range $E_i \approx 13-570$ eV, measured during ICP plasma etching of Si in Cl_2 under the same conditions as in Fig. 4.1. The wavelengths and transitions for the atomic and molecular emissions concerned are listed in Table 2.1.

trend in species concentration in the plasma, because no significant change in electron density and temperature occurred over the operating range investigated (as in Fig. 3.1). The results indicate that as the bias power P_{rf} or ion energy E_i is increased, the intensities or concentrations of etch product/byproduct neutrals SiCl_x ($x = 0-3$) increase and then tend to be saturated, while those of feed gas neutrals Cl_x ($x = 1, 2$) and ions Cl_2^+ decrease monotonically.

Similar behavior of the OES intensities was observed for different gas flow rates F_0 ; in practice, at a given P_{rf} or E_i , the intensities or concentrations of etch product/byproduct species were found to be decreased for increased F_0 , while those of feed gas species were increased, as partly shown in Fig. 4.3 for atomic Si and Cl. The former reflects shortened residence times and thus the reduced concentrations of products/byproducts in the plasma, and the latter reflects the consequently increased partial pressures or concentrations of feed gases under the operating conditions of constant pressure P_0 . It is further noted that the F_0 as well as P_{rf} or E_i dependence of the Cl emission intensity I_{Cl} was very similar to that of the Cl_2 one I_{Cl_2} , implying that the Cl intensity represents the trend in feed Cl_2 gas density in the plasma.

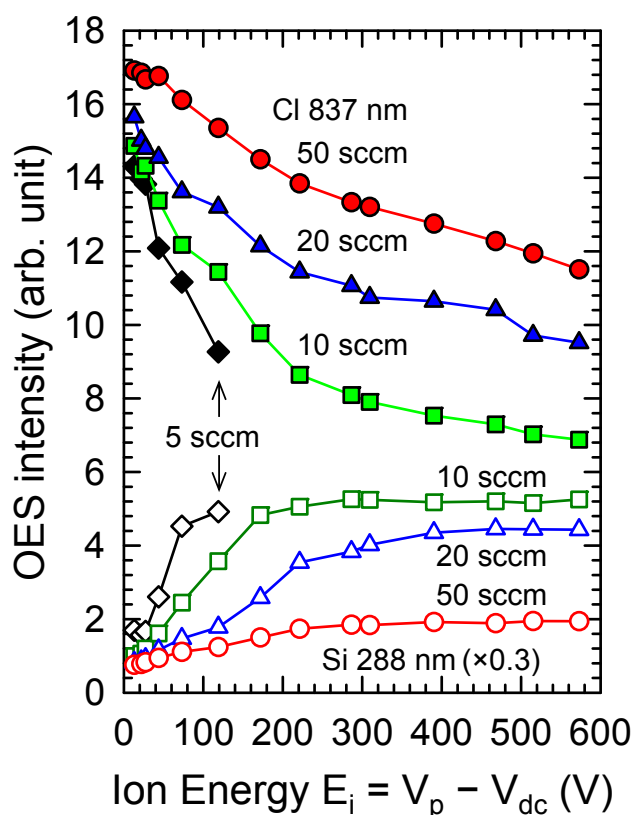


Fig. 4.3. OES intensities of two atomic lines of Si and Cl as a function of ion incident energy in the range $E_i \approx 13$ –570 eV, measured during ICP plasma etching of Si in Cl_2 for four different gas flow rates of $F_0 = 5$ –50 sccm under otherwise the same conditions as in Fig. 4.1.

4.1.2 Infrared absorption spectroscopy

Figure 4.4 shows the peak absorbance of SiCl_4 at around 620 cm^{-1} (ν_3 fundamental vibrational band)^[132–134] as a function of ion incident energy in the range $E_i \approx 13$ –570 eV, measured by FTIR-TAS during ICP plasma etching of Si in Cl_2 for four different gas flow rates of $F_0 = 5$ –50 sccm under otherwise the same conditions as in Fig. 3.1. The calibration was made by filling the ICP reactor chamber with pure SiCl_4 gases at different pressures in the range $P_0 = 0.05$ –50 mTorr without discharge, to derive the absolute concentration of etch product/byproduct neutrals SiCl_4 in the plasma during etching.^[132,133] The results indicate that for any F_0 , the absorbance of the 620-cm^{-1} SiCl_4 band and thus the concentration of SiCl_4 increases and then tends to be saturated with increasing P_{rf} or E_i , corresponding to the increase in etch rate; moreover, at a given P_{rf} or E_i , the absorbance and thus the concentration of SiCl_4 is decreased for increased flow rates F_0 , corresponding to shortened residence times of it. These are consistent with the behavior (E_i and F_0 dependences) of the OES intensities of SiCl_x ($x = 0$ –3) as

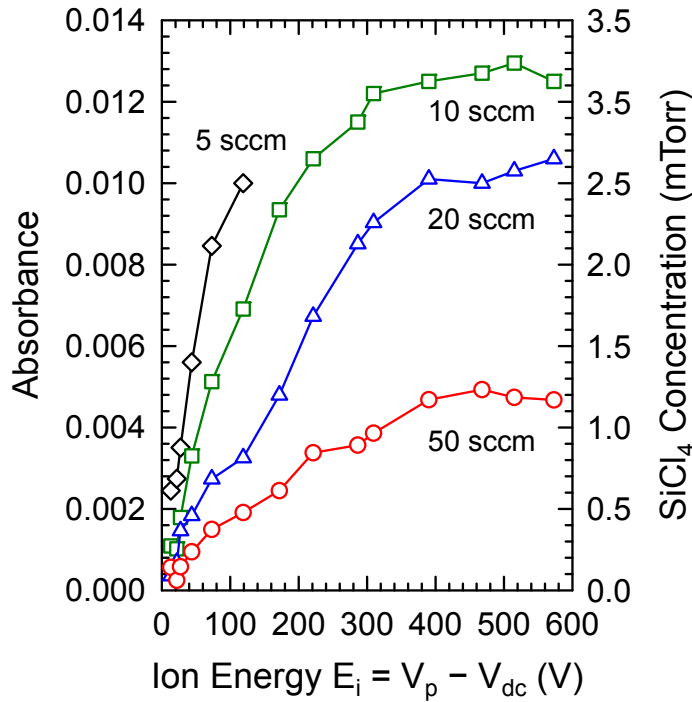


Fig. 4.4. Peak absorbance of SiCl_4 at around 620 cm^{-1} as a function of ion incident energy in the range $E_i \approx 13\text{--}570 \text{ eV}$, measured by FTIR-TAS during ICP plasma etching of Si in Cl_2 for four different gas flow rates of $F_0 = 5\text{--}50 \text{ sccm}$ under otherwise the same conditions as in Fig. 4.1. The calibration was made by filling the ICP reactor chamber with pure SiCl_4 gases at different pressures in the range $P_0 = 0.05\text{--}50 \text{ mTorr}$ without discharge, to derive the absolute concentration of etch product/byproduct neutrals SiCl_4 in the plasma during etching.

shown above in Figs. 4.2 and 4.3. The concentration of SiCl_4 in the plasma during etching is estimated to be more than 10% of the feed Cl_2 gas density, at increased P_{rf} or E_i and for decreased F_0 ; e.g., $[\text{SiCl}_4]/[\text{Cl}_2]_0 > 0.1$ (or $[\text{SiCl}_4] > 6.4 \times 10^{13} \text{ cm}^{-3}$ at $P_0 = 20 \text{ mTorr}$), at $E_i > 250 \text{ eV}$ for $F_0 = 20 \text{ sccm}$ and at $E_i > 150 \text{ eV}$ for $F_0 = 10 \text{ sccm}$, where $[\text{Cl}_2]_0$ denotes the Cl_2 density under plasma-off conditions. The SiCl_4 partial pressure or concentration presently measured is in agreement with previous QMS measurements during plasma etching of Si in Cl_2 .^[154,155]

It is further noted that in a rough approximation, taking account of the recent modeling simulations of ICP plasma etching of Si in Cl_2 that the most common etch product/byproduct neutrals in the plasma are SiCl_x ($x = 2\text{--}4$) with comparable densities,^[156] the total amount of them is estimated to be $\sum_x [\text{SiCl}_x]/[\text{Cl}_2]_0 > 0.3$ under the above conditions. This is consistent with the OES data for feed gas neutrals as shown in Figs. 4.2 and 4.3: $I_{\text{Cl}}/(I_{\text{Cl}})_0 \approx I_{\text{Cl}_2}/(I_{\text{Cl}_2})_0 \approx [\text{Cl}_2]/[\text{Cl}_2]_0 < 0.7$ under these conditions, assuming low degree of dissociation of Cl_2 in the plasma. Here, $(I_{\text{Cl}})_0$ and $(I_{\text{Cl}_2})_0$ denote the Cl and Cl_2 emission intensities in the absence of etching ($P_{\text{rf}} = 0 \text{ W}$ or $E_i \approx 13 \text{ eV}$ without breakthrough step).

4.1.3 Mass spectrometry

Figure 4.5 shows typical QMS spectra in the mass range $m/e = 1\text{--}200$ amu during ICP plasma etching of Si in Cl_2 , measured with the ionizer (using 70-eV electrons) switched on and off, for an ion incident energy of $E_i \approx 120$ eV under the same conditions as in Fig. 4.1. In the spectra, the signals of Si- and Cl-containing species consist of multiple peaks originating from naturally abundant isotopes of Si (^{28}Si , ^{29}Si , ^{30}Si) and Cl (^{35}Cl , ^{37}Cl); in addition, the signal intensities of Si-containing species were found to be lowered by several orders of magnitude in the absence of etching ($P_{\text{rf}} = 0$ W or $E_i \approx 13$ eV without breakthrough), implying that they originate primarily from etch products desorbed from substrate surfaces during etching. The ion mass spectrum with the ionizer off indicates that the predominant ions are ionized etch products/byproducts, SiCl^+ and SiCl_3^+ followed by SiCl_4^+ , which are more abundant than the dominant feed gas ions Cl_2^+ , as has been observed and/or concluded in a few QMS measurements during Cl_2 and Cl_2 -containing plasma etching of Si.^[157–159] This essential feature for the predominant ionic species during etching (SiCl_x^+ , and not Cl_x^+) has been different from most modeling predictions,^[160–162] while has lastly been predicted by the recent modeling simulations.^[156] The neutral mass spectrum with the ionizer on exhibits several peaks of impurity species O, OH, H_2O , and HCl ($m/e = 16, 17, 18,$ and $36/38$), in addition to peaks of etch product/byproduct SiCl_x ($x = 0\text{--}4$) and feed gas Cl_x ($x = 1, 2$) species. In practice, O, OH, and H_2O were detected in the neutral spectrum, even when the ICP reactor chamber was pumped down to a base pressure, and the HCl signal was increased under plasma-on conditions, implying that these impurities detected arise probably from H_2O adsorbed on the QMS chamber walls.

It is further noted that weak signals were detected around $m/e = 44$ (SiO)^[157] and 247 (Si_2OCl_5)^[152,155] in both the ion and neutral mass spectra, and around $m/e = 310$ (Si_3OCl_6) and 361 ($\text{Si}_3\text{O}_2\text{Cl}_7$) in the ion spectrum, while no significant signal was detected around $m/e = 231, 266,$ and 301 (Si_2Cl_x ; $x = 5, 6,$ and 7)^[152,155] in both spectra. These O-containing byproducts detected (silicon oxides and oxychlorides) arise probably from reactions of etch products/byproducts (silicon chlorides) with O impurities sputtered from the dielectric window at the top of the ICP reactor chamber; in practice, a small amount of oxygen was also assumed to occur therein under plasma-on conditions, in view of the FTIR-TAS spectra that exhibited a weak absorption of SiO at around 1100 cm^{-1} ,^[111,132–135] although the O line emissions (e.g., peaks at $777.1\text{--}777.5$ and 844.6 nm)^[109] were not detected in the OES observations. In the present experiments, only the ion mass spectrum was analyzed to investigate the composition of

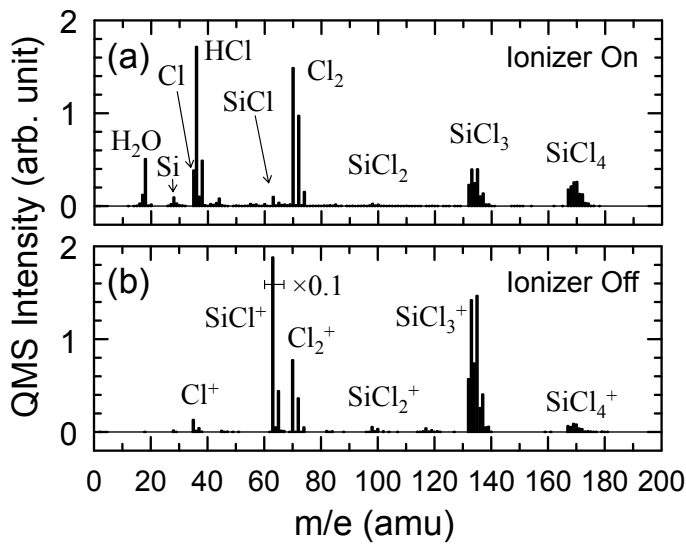


Fig. 4.5. Typical QMS spectra in the mass range $m/e = 1\text{--}200$ amu during ICP plasma etching of Si in Cl_2 , measured with the ionizer (using 70-eV electrons) switched (a) on and (b) off, for an ion incident energy of $E_i \approx 120$ eV under the same conditions as in Fig. 4.1. In the spectra, the signals of Si- and Cl-containing species consist of multiple peaks originating from naturally abundant isotopes of Si (^{28}Si , ^{29}Si , ^{30}Si) and Cl (^{35}Cl , ^{37}Cl).

the ion flux entering the mass spectrometer and similarly incident on substrate surfaces from the plasma, because the neutral spectrum requires careful attention and differential pumping systems to gain quantitative information on incoming neutral fluxes.^[128,129,154,155,163]

Figure 4.6 shows the integrated QMS intensities of seven ionic species SiCl_x^+ ($x = 0\text{--}4$) and Cl_x^+ ($x = 1, 2$) as a function of ion incident energy in the range $E_i \approx 13\text{--}570$ eV, measured with the ionizer off during ICP plasma etching of Si in Cl_2 under the same conditions as in Fig. 4.1. Note that in these measurements, the raw signal intensity (counts/s) of ionic species was corrected, taking into account the transmission and detection efficiency of the spectrometer depending on ion mass,^[157] then, the corrected signal intensities of isotopic components of the respective ions were integrated to estimate the incoming flux of the ionic species concerned. The results indicate that as the bias power P_{rf} or ion energy E_i is increased, the intensities or fluxes of ionized etch products/byproducts SiCl_x^+ ($x = 0, 1, 2, 4$) increase and then tend to be saturated, corresponding to the increase in etch rate, while SiCl_3^+ exhibits a little different behavior that its flux increases, peaks, and then decreases. This is ascribed presumably to etch product species desorbed depending on E_i ; in practice, the primary etch products desorbed from substrate surfaces during Si etching in Cl_2 plasmas are generally assumed to be saturated SiCl_4 at low $E_i < 100$ eV, while unsaturated SiCl_x ($x = 1, 2$) at higher E_i .^[36,164–166] Under plasma electron-impact ionization in the energy range concerned ($E_e < \text{a few tens of eV}$), we may consider that SiCl_4 molecules predominantly fragment into SiCl_3^+ , followed by SiCl_4^+ and

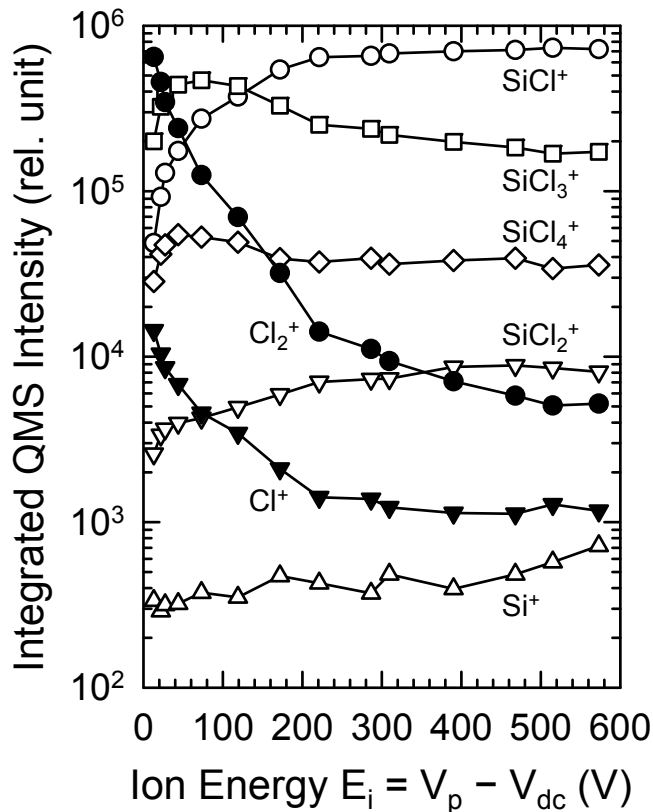


Fig. 4.6. Integrated QMS intensities of seven ionic species SiCl_x^+ ($x = 0-4$) and Cl_x^+ ($x=1, 2$) as a function of ion incident energy in the range $E_i \approx 13-570$ eV, measured with the ionizer switched off during ICP plasma etching of Si in Cl_2 under the same conditions as in Fig. 4.1. In these measurements, the raw signal intensity (counts/s) of ionic species was corrected, taking into account the transmission and detection efficiency of the spectrometer depending on ion mass; then, the corrected signal intensities of isotopic components of the respective ions were integrated to estimate the incoming flux of the ionic species concerned.

SiCl^+ ,^[167-169] and that SiCl_2 and SiCl yield predominantly SiCl_2^+ and SiCl^+ , respectively.^[170,171] These situations appear to lead to the present QMS measurements that SiCl_3^+ is the predominant Si-containing ion flux at low $E_i < 120$ eV, followed by SiCl^+ and SiCl_4^+ , while SiCl^+ is that at higher E_i , followed by SiCl_3^+ and SiCl_4^+ .

On the other hand, the intensities or fluxes of feed gas ions Cl_x^+ ($x = 1, 2$) decrease monotonically with increasing E_i , corresponding to the increase in etch rate and the consequent reduced partial pressures or concentrations of feed gases under the operating conditions of constant pressure P_0 ; in practice, Cl_2^+ is much more abundant than Cl^+ , probably because Cl_2 molecules yield predominantly Cl_2^+ under electron-impact ionization in the plasma concerned.^[172,173] As a result, the predominant ion fluxes during etching are those of ionized feed gas molecules Cl_2^+ at low $E_i < 30$ eV, while those of ionized etch products/byproducts SiCl_3^+ at higher $E_i > 30$ eV and those of SiCl^+ at further increased $E_i > 120$ eV. It should be noted here that at $E_i \approx 30$ eV for $F_0 = 20$ sccm [where the Si etch rate is $\text{ER} \approx 100$ nm/min as in Fig. 3.3(a)], e.g., the respective ion fluxes and concentrations concerned are estimated from the

QMS data of Fig. 4.6 (calibrated by the probe ion saturation current) as: $\Gamma(\text{SiCl}_3^+) \approx 1.9 \times 10^{15} \text{ cm}^{-2}\text{s}^{-1}$, $\Gamma(\text{SiCl}^+) \approx 0.64 \times 10^{15} \text{ cm}^{-2}\text{s}^{-1}$, and $\Gamma(\text{Cl}_2^+) \approx 1.7 \times 10^{15} \text{ cm}^{-2}\text{s}^{-1}$ (total ion flux $\Gamma_i^0 \approx 5.0 \times 10^{15} \text{ cm}^{-2}\text{s}^{-1}$); $n(\text{SiCl}_3^+) \approx 1.1 \times 10^{10} \text{ cm}^{-3}$, $n(\text{SiCl}^+) \approx 0.37 \times 10^{10} \text{ cm}^{-3}$, and $n(\text{Cl}_2^+) \approx 1.0 \times 10^{10} \text{ cm}^{-3}$ (total ion density $n_i \approx 2.9 \times 10^{10} \text{ cm}^{-3}$). Thus, it is concluded that under most conditions in these experiments, the fluxes and concentrations of etch products/byproduct ions SiCl_x^+ account for more than half of the total ion flux and density, although their neutrals SiCl_x represent a small fraction of the total species density in the reactor chamber; e.g., under the above conditions, $[\text{SiCl}_4]/[\text{Cl}_2]_0 \approx 0.019$ and $\Sigma_x[\text{SiCl}_x]/[\text{Cl}_2]_0 \approx 0.057$, as estimated from the FTIR-TAS data of Fig. 4.4. These situations have so far been indicated in only a few QMS measurements^[157–159] and modeling calculations,^[156] being ascribed partly to the difference between the total electron ionization cross sections for SiCl_x ($x = 1–4$)^[167,170,171,174,175] and Cl_2 ^[173,176–178] molecules; in effect, the former is about 2–3 times larger than that the latter.

Similar behavior of the integrated QMS intensities was observed for different gas flow rates F_0 ; in practice, at a given P_{rf} or E_i , the intensities or fluxes of ionized etch products/byproducts were found to be decreased for increased F_0 , while those of feed gas ions were increased. The E_i and F_0 dependences of the QMS intensities of SiCl_x^+ ($x = 0–4$) and Cl_x^+ ($x = 1, 2$) ions are consistent with those of the OES intensities of SiCl_x ($x = 0–3$), Cl_x ($x = 1, 2$), and Cl_2^+ as shown in Figs. 4.2 and 4.3, and also with those of the FTIR-TAS absorbance of SiCl_4 as in Fig. 4.4. **Figure 4.7** shows the total integrated QMS intensity of SiCl_3^+ , SiCl_4^+ , Cl^+ , and Cl_2^+ ions and that of Si^+ , SiCl^+ , and SiCl_2^+ ions as a function of ion incident energy in the range $E_i \approx 13–570$ eV, measured with the ionizer off during ICP plasma etching of Si in Cl_2 for four different flow rates of $F_0 = 5–50$ sccm under otherwise the same conditions as in Fig. 4.1. These data are those obtained by summing the respective ion intensities as shown in the preceding Fig. 4.6, and inset is an enlarged view of the figure in the range $0 \leq E_i \leq 300$ eV. It should be noted here that the former four ions (dominated by Cl_2^+ at low E_i , while SiCl_3^+ at high E_i) are reactive on Si, while the latter three (dominated by SiCl^+) are depositive,^[96] as demonstrated by using classical MD simulations in Sec. 4.2.

The results indicate that as the bias power P_{rf} or ion energy E_i is increased, the total intensity or flux of reactive ions decreases, while that of depositive ones increases; consequently, the change in the predominant ion flux from reactive to depositive occurs at increased E_i , where the transition point is increased for increased F_0 , being at around $E_i \approx 30, 70, 150,$ and 500 eV for $F_0 = 5, 10, 20,$ and 50 sccm, respectively. Such a change in the predominant ion flux

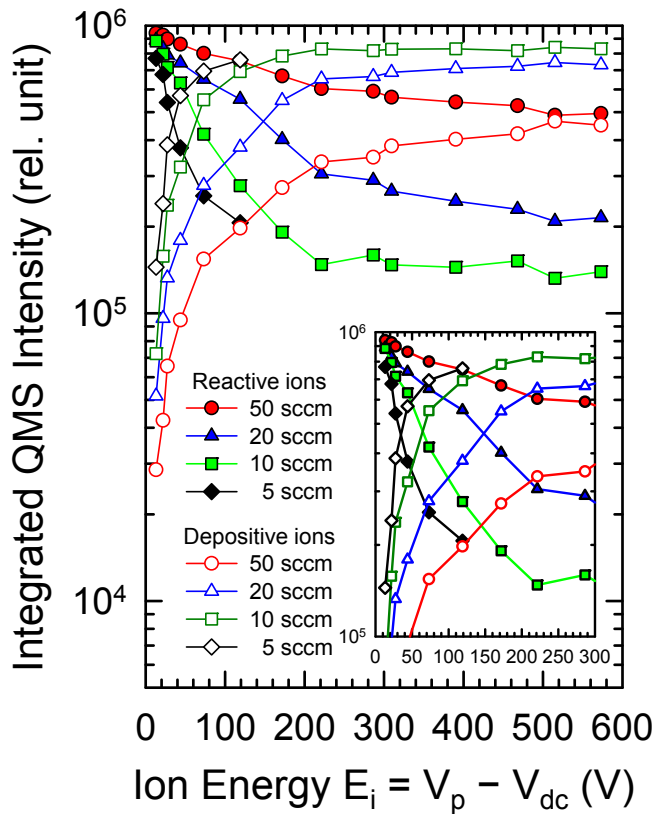


Fig. 4.7. Total integrated QMS intensity or incoming flux of SiCl_3^+ , SiCl_4^+ , Cl^+ , and Cl_2^+ ions and that of Si^+ , SiCl^+ , and SiCl_2^+ ions as a function of ion incident energy in the range $E_i \approx 13\text{--}570$ eV, measured with the ionizer off during ICP plasma etching of Si in Cl_2 for four different gas flow rates of $F_0 = 5\text{--}50$ sccm under otherwise the same conditions as in Fig. 4.1. These data are those obtained by summing the respective ion intensities as shown in the preceding Fig. 4.6, and inset is an enlarged view of the figure in the range $0 \leq E_i \leq 300$ eV. Note that the former four ions (dominated by SiCl_3^+ at low E_i , while Cl_2^+ at high E_i) are reactive on Si, while the latter three (dominated by SiCl^+) are depositive.

appears to be related to the two modes of surface roughening that occur depending on E_i , as shown and discussed above in Sec. 3.2 and Sec. 3.3, although the transition point concerned does not fully agree with the transition point E_p for the rms roughness versus E_i curve [Fig. 3.3(b)] and that for the ER or Y versus $E_i^{1/2}$ curve (Fig. 3.4).

4.2 Etch Fundamentals of Ionized Etch Products

Figure 4.8 shows side views of the Si(100) surface at after 2000 impacts of Cl_x^+ ($x = 1, 2$) and SiCl_x^+ ($x = 0\text{--}4$) beam ion thereon, obtained through the classical MD simulation with different beam energies $E_i = 20\text{--}500$ eV at $\theta_i = 0^\circ$ (normal incidence). The MD is our original simulation for reaction kinetics (or plasma–surface interactions) and the etching fundamentals during plasma etching of Si in Cl-based plasmas, as detailed in Appendix B; briefly, an improved interatomic potential form of the Stillinger–Weber (SW) type^[94,95] is employed for

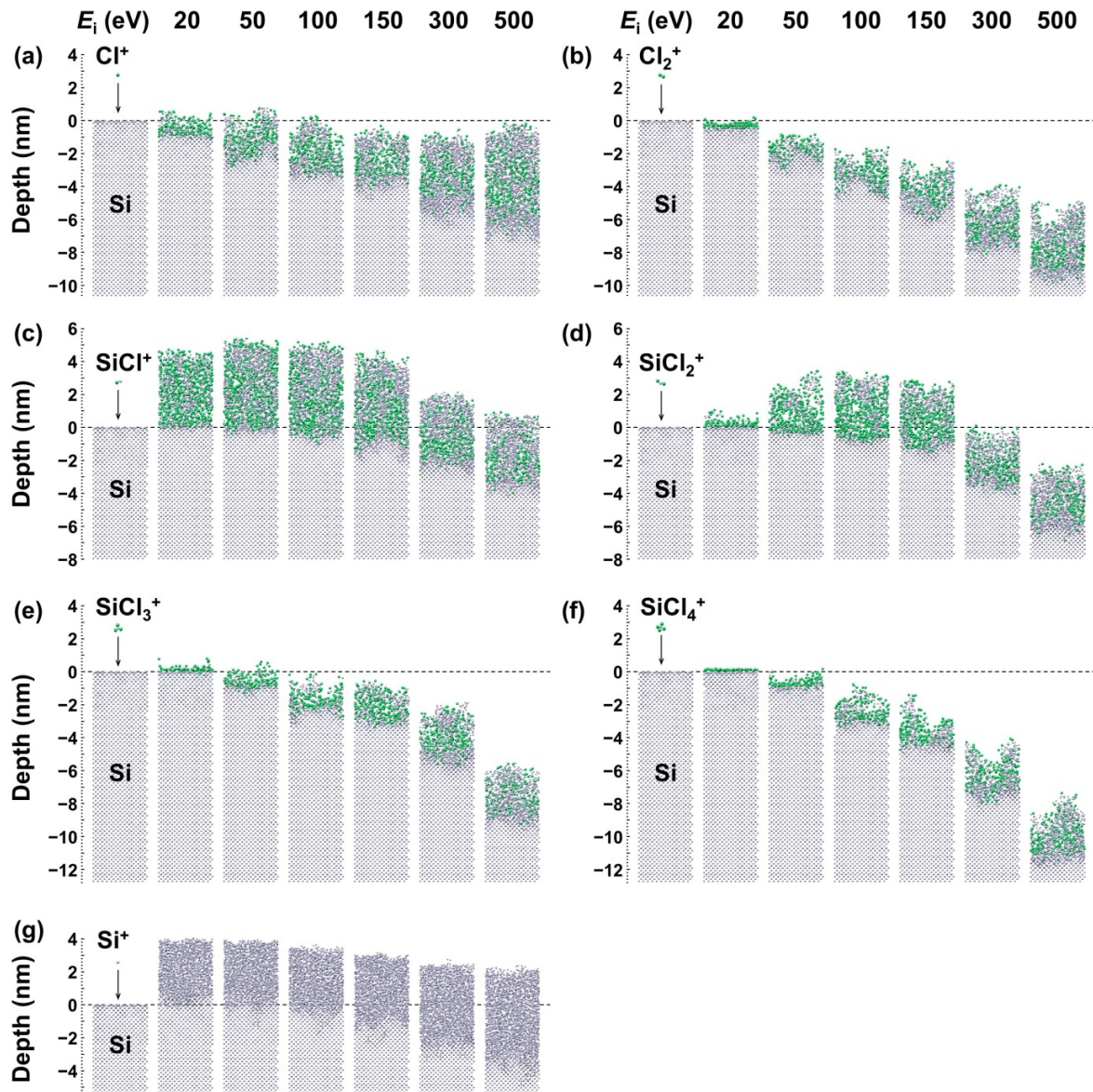


Fig. 4.8. Side views of the Si(100) surface, obtained through the classical MD simulation of (a) Cl^+ , (b) Cl_2^+ , (c)–(f) SiCl_x^+ ($x = 1$ –4), and (g) Si^+ ion incidences with different energies of $E_i = 20$ –500 eV at $\theta_i = 0^\circ$ (normal incidence), where some mimic Si substrate layers are added to the bottom for adjustment of the depth. Note that these are snapshots taken after 2000 impacts, and the ions are assumed to be charge-neutral species with high translational energies.

Si/Cl systems. The ions of interest are Cl_x^+ ($x = 1, 2$) and SiCl_x^+ ($x = 0$ –4) with translational energies in the range $E_i = 20$ –500 eV, being incident on Si(100) surfaces at incident angles in the range $\theta_i = 0^\circ$ – 85° . Calculations were performed for square substrates 32.58 \AA on a side with an initial depth of 26.0 \AA (1440 Si atoms initially contained in the simulation cell), in the

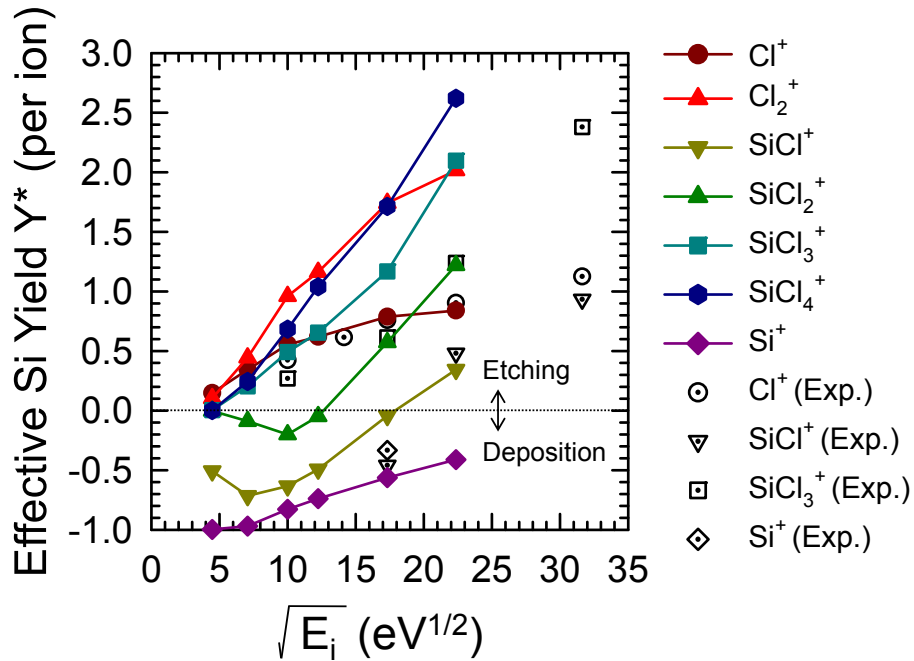


Fig. 4.9. Effective Si Yield Y^* per ion impact as a function of the square root of the incident energy, $E_i^{1/2}$, obtained through the MD simulation under the same conditions as in Fig. 4.8. Also shown are the recent experimental data on sputtering yield for Cl^+ , Si^+ , SiCl^+ , and SiCl_3^+ ion beam impacts on poly-Si.^[179]

absence of incoming neutrals ($\Gamma_n^0/\Gamma_i^0 = 0$); in addition, the substrate was artificially cooled down to initial temperature ($T_s = 300$ K) after every injection of an energetic ion. The results indicate that in Cl^+ , Cl_2^+ , SiCl_3^+ , and SiCl_4^+ incidences, the etch depth and surface reaction SiCl_x layer thickness increases with increasing E_i . On the other hand, in SiCl^+ and SiCl_2^+ incidences, the deposition dominates at low E_i , being more significant for SiCl^+ than for SiCl_2^+ , while the etching appears to dominate over deposition at further increased E_i , where the bottom of disordered Si substrate layers deepens with increasing E_i , and the SiCl_x layer thickness decreases and then increases slightly with increasing E_i . In Si^+ incidence, the deposition of Si atoms dominates at low E_i , while the competition between deposition and etching (or sputtering) appears to occur at further increased E_i .

Figure 4.9 shows the effective Si yield Y^* per ion impact as a function of the square root of the ion incident energy, $E_i^{1/2}$, obtained through the MD simulation averaged over more than 1000 impacts under the same conditions as in Fig. 4.8. Also shown are the recent experimental data on sputtering yield for Cl^+ , Si^+ , SiCl^+ , and SiCl_3^+ beam impacts on poly-Si.^[179] Here, in

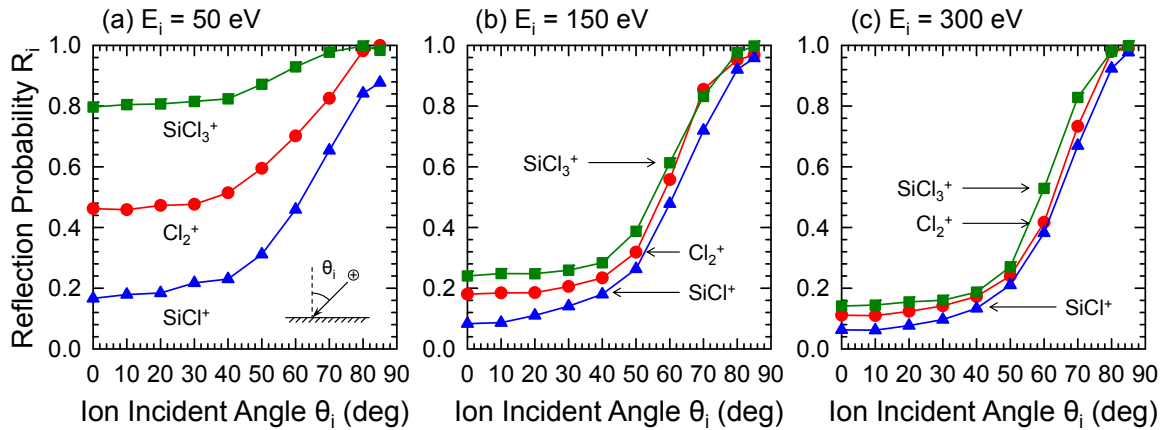


Fig. 4.10. Reflection probability on Si(100) surfaces of Cl_2^+ , SiCl^+ , and SiCl_3^+ ions as a function of the ion incident angle in the range $\theta_i = 0^\circ\text{--}85^\circ$, obtained through the MD simulation with three different ion incident energies of $E_i =$ (a) 50, (b) 150, and (c) 300 eV.

Cl_x^+ incidences, the effective Si yield Y^* (per ion) equals the Si yield Y (per ion), which is defined as the total number of Si atoms desorbed from substrate surfaces per ion impact; on the other hand, the effective yield is $Y^* = Y - 1$ in SiCl_x^+ incidences, because one Si atom is incident on surfaces per SiCl_x^+ impact. Thus, the positive Y^* indicates the situation of etching and gives the etch yield (or the total number of Si atoms desorbed per incident ion), while the negative Y^* indicates the situation of deposition and its absolute value gives the deposition yield (or the total number of Si atoms deposited per incident ion). The results indicate that in Cl^+ , Cl_2^+ , SiCl_3^+ , and SiCl_4^+ incidences, the etching occurs in the whole E_i range investigated, where the yield Y^* increases with increasing E_i . On the other hand, in SiCl^+ and SiCl_2^+ incidences, transition from deposition to etching occurs at around $E_i \approx 300$ and 150 eV, respectively, where the yield Y^* increases with increasing E_i ; moreover, in Si^+ incidence, the deposition occurs in the whole E_i range investigated, where the absolute value of the yield Y^* decreases or the deposition is reduced with increasing E_i . These are consistent with the results of beam experiments previously reported: SiCl_x^+ ($x = 1\text{--}3$) beams of $E_i = 30$ eV (Ref. [180]) and Cl^+ and SiCl_x^+ ($x = 0, 1, 3$) beams of $E_i = 100\text{--}500$ eV (Ref. [179]) incident on Si surfaces. Thus, it is concluded that incident ions concerned can be classified into the reactive ones (Cl^+ , Cl_2^+ , SiCl_3^+ , SiCl_4^+) and the depositive ones (Si^+ , SiCl^+ , SiCl_2^+), as mentioned above with respect to Fig. 4.7.

Figure 4.10 shows the reflection probability on Si(100) surfaces of Cl_2^+ , SiCl^+ , and SiCl_3^+ ions as a function of the ion incident angle in the range $\theta_i = 0^\circ\text{--}85^\circ$, obtained through the MD

simulation with three different ion incident energies of $E_i = 50, 150, \text{ and } 300 \text{ eV}$. The results indicate that for any E_i , the reflection probability on surfaces increases with increasing incidence angle, where it is significantly lowered for depositive SiCl^+ ion as compared to that for reactive Cl_2^+ and SiCl_3^+ ions. Thus, it is implied that in experiments, the reflection probabilities of the incident ions reduce with increasing E_i , corresponding to the changes in the predominant ion flux from reactive ions (dominated by Cl_2^+ at low E_i , while SiCl_3^+ at high E_i) to depositive ones (dominated by SiCl^+) thereat.

4.3 Mechanisms for Surface Roughening

Figure 4.11 shows the etch rate and rms surface roughness of Si as a function of ion incident energy in the range $E_i = 20\text{--}500 \text{ eV}$, obtained through ICP Cl_2 plasma etching experiments and ASCeM-3D simulations ($t_{\text{etch}} = 2 \text{ min}$). The experimental data shown are those for $F_0 = 20 \text{ sccm}$ in Fig. 3.3, and the ASCeM-3D results are those calculated with normal ion incidence ($\theta_i = 0^\circ$) assuming similar plasma conditions. Note that the ASCeM-3D is our original 3D Monte Carlo-based simulation model for plasma–surface interactions and the feature profile evolution during plasma etching of Si in Cl_2 and Cl_2/O_2 ,^[88] as detailed in Appendix A; briefly, the model takes into account the behavior (transport and surface reactions) of Cl^+ ions, Cl and O neutrals, and etch products and byproducts of SiCl_x and SiCl_xO_y in microstructures and on feature surfaces therein. The surface chemistry and kinetics included are: surface chlorination, chemical etching, ion-enhanced etching, sputtering, surface oxidation, redeposition of etch products desorbed from feature surfaces being etched, and deposition of etch products/byproducts coming from the plasma. The model also takes into account the ion reflection or scattering from feature surfaces on incidence and/or the ion penetration into substrates, along with geometrical shadowing of the feature and surface reemission of neutrals. The simulation domain consists of small cubic cells of atomic size ($L = 2.7 \text{ \AA}$), and the evolving interfaces are represented by removing Si atoms from and/or allocating them to the cells concerned. Calculations were performed for square substrates $W = 50 \text{ nm}$ on a side, with an incoming ion flux and neutral reactant-to-ion flux ratio of $\Gamma_i^0 = 1.0 \times 10^{16} \text{ cm}^{-2}\text{s}^{-1}$ and $\Gamma_n^0/\Gamma_i^0 = 100$, respectively, in the absence of incoming oxygen and etch products/byproducts ($\Gamma_o^0 = \Gamma_p^0 = 0$);^[88] in addition, the ion and neutral (or gas) temperatures were assumed to be $k_B T_i = 0.5 \text{ eV}$ and $T_g = 500 \text{ K}$, respectively, together with the dopant concentration $N_d = 1.0 \times 10^{18} \text{ cm}^{-3}$ and

surface temperature $T_s = 320$ K of substrates.

A comparison between experiments and simulations indicates that the ASCeM-3D reproduces well the increase in Si etch rate with increasing E_i in the whole range investigated, and the increase in rms roughness of etched Si surfaces at low $E_i < E_p \approx 250$ eV (roughening mode); in contrast, it does not reproduce the decrease in rms surface roughness of Si at higher $E_i > E_p$ (smoothing mode), where the rms roughness in experiments decreases substantially with increasing E_i down to a low level < 0.4 nm, while it continues to increase with E_i in simulations. Some difference in magnitude of the rms roughness between experiments and simulations at low $E_i < E_p$ is ascribed to the known behavior that the larger the scan area, the larger is the roughness;^[181] in practice, the rms roughness in experiments is that measured for the AFM scan area of $1 \times 1 \mu\text{m}^2$ (as mentioned earlier with respect to Fig. 3.2), while the rms roughness in simulations is that acquired for the ASCeM-3D domain of $50 \times 50 \text{ nm}^2$.

4.3.1 Smoothing mode

Also shown in Fig. 4.11 are the ASCeM-3D results for Si etching in Cl_2 plasmas obtained with the ion reflection switched off in the simulation. The results indicate that in the absence of ion reflection (or assuming all the ions incident on surfaces to penetrate into substrates without reflection), the rms surface roughness is reduced substantially to a low level < 0.4 nm, almost independently of ion energy in the whole E_i range investigated, and surprisingly it is in agreement with the experiments at high $E_i > 400$ eV. It is noted that the etch rate is slightly increased with the ion reflection off, owing to the increased ion energy deposited on surfaces, which is more significant at increased E_i . Such a substantial decrease in rms roughness and slight increase in etch rate with the ion reflection off were also observed in the ASCeM-3D simulations taking into account of incoming oxygen and etch products/byproducts (as will be partly shown later). These imply that the ion reflection or scattering from microscopically roughened feature surfaces on incidence plays a crucial role in plasma-induced surface roughening, particularly in the evolution of surface roughness with time during etching; in effect, the reflection of energetic ions from feature surfaces tends to concentrate them onto the bottom (or the valley) of the feature,^[87] thus resulting in an increase in roughness to its vertical as well as lateral extent, where the increase in lateral extent of the roughness is attributed to the uniformity of the incident flux and angle of ions and/or neutral etchants on surfaces at microscale. Thus, at increased $E_i > E_p$ (smoothing mode) in the present experiments, some

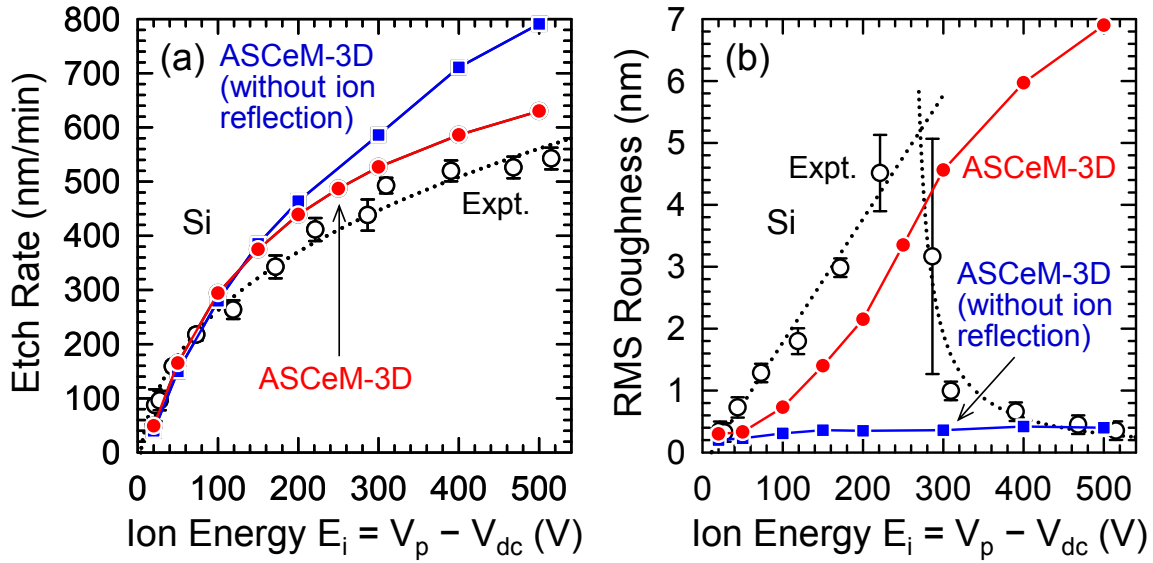


Fig. 4.11. (a) Etch rate and (b) rms surface roughness of Si as a function of ion incident energy in the range $E_i = 20\text{--}500$ eV, obtained through ICP Cl_2 plasma etching experiments and ASCeM-3D simulations ($t_{\text{etch}} = 2$ min). Also shown are the ASCeM-3D results obtained with the ion reflection switched off in the simulation. The experimental data shown are those for $F_0 = 20$ sccm in Fig. 3.3, and the ASCeM-3D results are those calculated with the simulation domain of 50×50 nm² under normal ion incidence ($\theta_i = 0^\circ$) assuming similar plasma conditions [see the text for the calculation conditions ($\Gamma_o^0 = \Gamma_p^0 = 0$)].

plasma environments (or parameters of incoming ions) may be changed, to significantly reduce the effects of ion reflection and thus substantially reduce the surface roughness down to the low level of stochastic roughening. A promising change of interest is that in the predominant flux of ionic species from feed gas ions Cl_x^+ to ionized etch products/byproducts SiCl_x^+ at increased E_i , caused by the increased etch rates, as shown in Figs. 4.6 and 4.7; more precisely, the change in the predominant ion flux from reactive ions (dominated by Cl_2^+ at low E_i , while SiCl_3^+ at high E_i) to depositive ones (dominated by SiCl^+) at increased E_i .

In practice, our recent MD simulations of SiCl_x^+ ($x = 0\text{--}4$) and Cl_x^+ ($x = 1, 2$) ion incidences on Si(100) surfaces with translational energies of $E_i = 20\text{--}500$ eV have demonstrated that: for any E_i , the reflection probability on surfaces increases with increasing incidence angle in the range $\theta_i = 0^\circ\text{--}85^\circ$ investigated, where it is significantly lowered for depositive ions (Si^+ , SiCl^+ , SiCl_2^+) as compared to that for reactive ones (SiCl_3^+ , SiCl_4^+ , Cl^+ , Cl_2^+),^[98] as partly shown in Fig. 4.10; particularly, at grazing incidence ($\theta_i \geq 80^\circ$), the reflection probability was estimated to be in the range 0.6–0.95 for depositive ions (depending on species and E_i), while it was to be

approximately unity for reactive ones (almost independently of species and E_i). For example, the reflection probability at $\theta_i = 80^\circ$ was estimated to be about 0.99, 0.96, and 0.83 for SiCl_3^+ , Cl_2^+ , and SiCl^+ with $E_i = 50$ eV, respectively, and it was to be about 0.99, 0.99, and 0.90 for SiCl_3^+ , Cl_2^+ , and SiCl^+ with $E_i = 500$ eV, respectively. Moreover, our recent ASCeM-3D simulations have demonstrated that with the reflection of at least 10–20% of the incident ions switched off (or assuming at least 10–20% of the ions incident on surfaces to penetrate into substrates without reflection), the rms surface roughness of Si is reduced substantially to a low level < 0.4 nm, almost independently of E_i , similarly as in Fig. 4.11.^[89] These would support our proposed mechanisms as mentioned above, for the phenomena presently observed at increased $E_i > E_p$ (smoothing mode) in experiments.

4.3.2 Roughening mode

Figures 4.12(a) and 4.12(b) show the etch rate and rms surface roughness of Si as a function of etching or plasma exposure time in the range $0 \leq t \leq 2$ min for five different ion incident energies of $E_i = 20$ –500 eV, obtained through ASCeM-3D simulations with the ion reflection switched on and off for Si etching in Cl_2 plasmas. These are the respective typical runs, corresponding to the ASCeM-3D results in the preceding Fig. 4.11. For any E_i , the etch rate exhibits a significant increase immediately after the start of etching and then maintains an almost constant value, in both the presence and absence of the effects of ion reflection; on the other hand, the rms roughness increases with time for a while ($t < 20$ s) and then tends to reach quasi-steady state in the presence of ion reflection, while it reaches quasi-steady state immediately after the start of etching, remaining at a low level < 0.4 nm in the absence of ion reflection. Thus, it follows that the ASCeM-3D does not reproduce the almost linear increase in rms surface roughness of Si with time during etching, presently observed at low $E_i < E_p \approx 250$ eV (roughening mode) in experiments as shown in Fig. 3.6, although it reproduces well the increase in Si etch rate and rms roughness with E_i thereat as in Fig. 4.11. In addition, it may also follow that in a sense, the ASCeM-3D with the ion reflection off reproduces the quasi-steady rms surface roughness of Si at a low level, observed at higher $E_i > E_p$ (smoothing mode) in experiments as shown in Fig. 3.6, along with the continuous increase in Si etch rate with E_i and its substantially decreased rms roughness thereat as in Fig. 4.11.

An increase in rms surface roughness with time during etching, along with quasi-steady etch rates, has been observed in several plasma etching experiments of Si in SF_6 ^[50,61,64,67] and

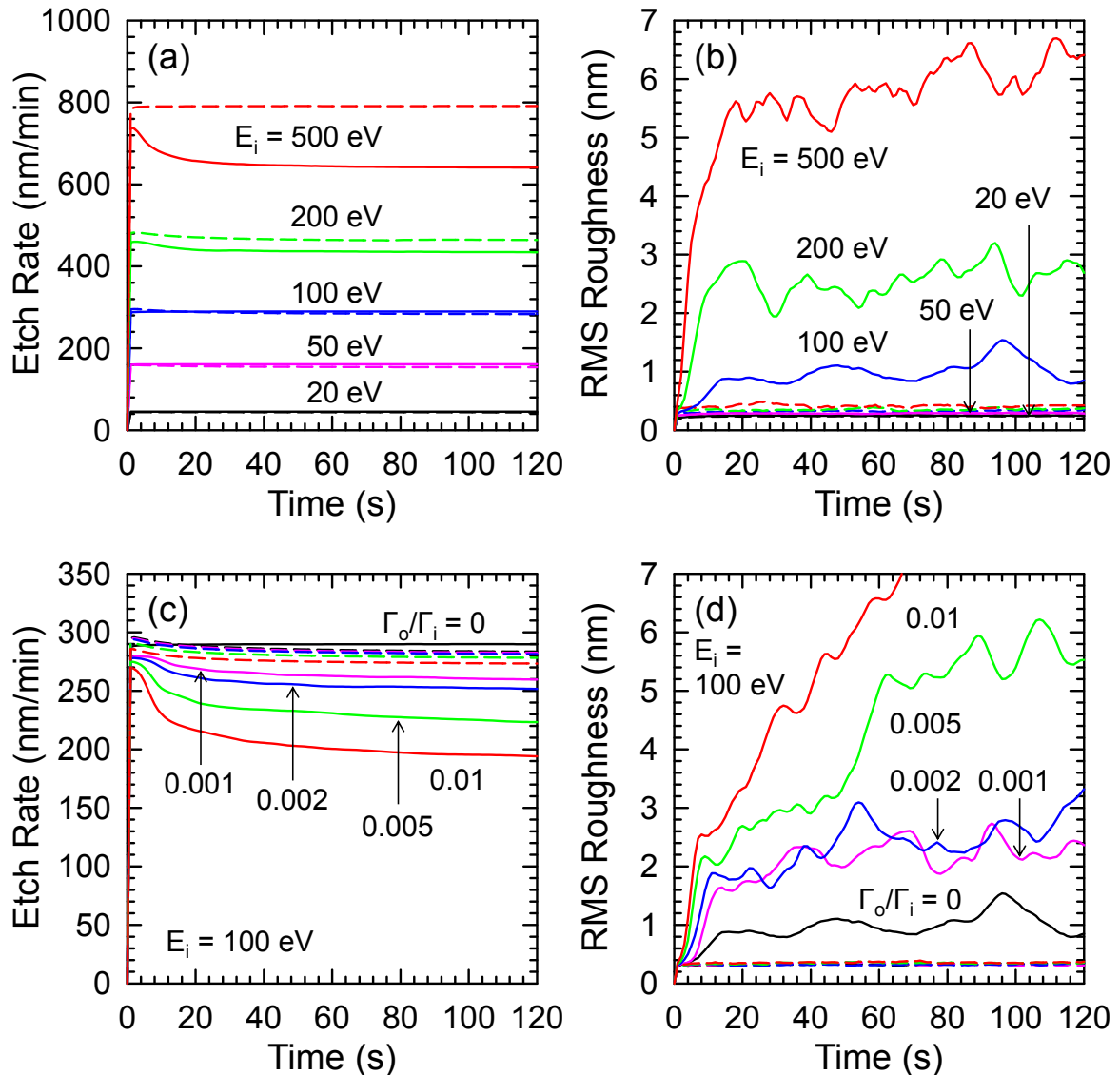


Fig. 4.12. (a) Etch rate and (b) rms surface roughness of Si as a function of etching or plasma exposure time in the range $0 \leq t \leq 2$ min for five different ion incident energies of $E_i = 20$ –500 eV, obtained through ASCeM-3D simulations with the ion reflection switched on (solid lines) and off (broken lines) for Si etching in Cl_2 plasmas. These are the respective typical runs, corresponding to the ASCeM-3D results shown in the preceding Fig. 4.11. Also shown are the (c) etch rate and (d) rms roughness of Si as a function of time, which are typical runs in the range $0 \leq t \leq 2$ min for $E_i = 100$ eV and five different incoming oxygen-to-ion flux ratios of $\Gamma_o^0/\Gamma_i^0 = 0$ –0.01, obtained through ASCeM-3D simulations with the ion reflection on (solid lines) and off (broken lines) for Si etching in Cl_2/O_2 plasmas under otherwise the same calculation conditions as in Fig. 4.11. Note that the data for $\Gamma_o^0/\Gamma_i^0 = 0$ in (c) and (d) are the same as those for $E_i = 100$ eV in (a) and (b).

CF_4/O_2 ,^[55] being attributed to the effects of etch inhibitors coming from the plasma.^[61,67] The

corresponding 2D and 3D Monte Carlo simulations of the surface feature evolution reproduced an almost linear increase in rms roughness and correlation length with time, assuming the origins for inhibitors to be materials of the reactor walls, electrodes, and etching masks (hard inhibitors), in addition to less volatile etch products/byproducts and feed gas fragments (soft inhibitors).^[61,67] Similarly, the ASCeM-3D simulations taking into account incoming inhibitor fluxes of oxygen ($\Gamma_o^0 \neq 0$) exhibited an increase in rms surface roughness of Si with increasing oxygen flux added, along with a significant decrease in etch rate,^[88] reproducing roughly an increase in rms roughness with time, as below.

Figures 4.12(c) and 4.12(d) show the Si etch rate and rms surface roughness as a function of time in the range $0 \leq t \leq 2$ min for $E_i = 100$ eV and five different oxygen-to-ion flux ratios of $\Gamma_o^0/\Gamma_i^0 = 0-0.01$, obtained through ASCeM-3D simulations with the ion reflection switched on and off for Si etching in Cl_2/O_2 plasmas under otherwise the same calculation conditions as in Fig. 4.11. Note that the data for $\Gamma_o^0/\Gamma_i^0 = 0$ in Figs. 4.12(c) and 4.12(d) are the same as those for $E_i = 100$ eV in Figs. 4.12(a) and 4.12(b). The etch rate behavior with incoming oxygen added is similar to that without oxygen, in both the presence and absence of the effects of ion reflection, where the decrease in Si etch rate with oxygen added is ascribed to surface oxidation that occurs,^[88] in addition, the slightly increased etch rate with the ion reflection off is more significant for increased Γ_o^0/Γ_i^0 , because the increased ion energy deposited on surfaces would increase the sputtering of oxides off the surface. On the other hand, the behavior of the rms roughness with incoming oxygen added is different from that without oxygen in the presence ion reflection: the rms surface roughness of Si tends to increase with time with oxygen added, which is more significant for increased Γ_o^0/Γ_i^0 . In addition, it is noted that the rms roughness is reduced substantially with the ion reflection switched off, remaining at a low level < 0.4 nm, whether there are incoming oxygen fluxes or not. A small amount of oxygen of the order of $\Gamma_o^0/\Gamma_i^0 \approx 10^{-3}$ (or $\Gamma_o^0/\Gamma_n^0 \approx 10^{-5}$) concerned here is ascribed to O impurities sputtered from the dielectric window at the top of the ICP reactor chamber under plasma-on conditions, as mentioned in Sec. 4.1.3 with respect to Fig. 4.5.

The ASCeM-3D simulations taking into account incoming inhibitor fluxes of etch products/byproducts ($\Gamma_p^0 \neq 0$) also exhibited an increase in rms surface roughness of Si with increasing product/byproduct flux added, along with a little decrease in etch rate,^[88] while they did not reproduce an increase in rms roughness with time; in these calculations, the time evolution of the rms surface roughness of Si was similar to that in the absence of incoming etch

inhibitors as in Fig. 4.12(b), or the rms roughness was found to increase for a while after the start of etching and then soon reach quasi-steady state. The decrease in Si etch rate with incoming products/byproducts added is ascribed to deposition of products/byproducts on surfaces being etched.^[88] It should be noted that the two kinds of incoming etch inhibitors concerned here, oxygen and etch products/byproducts, are assumed to play a similar role in surface chemistry and kinetics during etching of Si:^[88] they stick and/or deposit on surfaces being etched, to form passivation layers and inhibit etching thereon; in particular, on microscopically roughened feature surfaces, they are expected to stick and/or deposit preferentially on the top (or the hill) of roughened surface features, owing to the effects of neutral shadowing of the feature, and so tend to locally form passivation layers (or micromasks) and inhibit etching thereon, which leads to an increase in roughness with time during etching. The surface inhibitor or passivation layers thus formed (by surface oxidation and deposition of products/byproducts) are being removed by sputtering through energetic ion bombardment thereon. It should be further noted that in these situations, the sputter yields for energetic ions incident are assumed to be significantly (typically one order of magnitude) smaller on oxidized surfaces of SiO_x than on deposited ones of SiCl_x and SiCl_xO_y ,^[88] which in turn would lead to the difference in the evolution of roughness between the two kinds of inhibitor species concerned: an increase in roughness as well as a decrease in etch rate with incoming inhibitor fluxes added is more significant for oxygen than for products/byproducts. Hence, these imply that the almost linear increase in rms roughness of Si with time during etching, presently observed at low $E_i < E_p$ (roughening mode) in experiments, is caused presumably by a small amount of impurity oxygen contained.

4.3.3 Overview of mechanisms

Figure 4.13 shows a schematic of the mechanisms responsible for surface roughening during plasma etching of Si discussed and proposed above: (a) The low-level surface roughening occurs during etching, owing to the stochastic roughening that originates intrinsically from the temporal as well as spatial uniformity of the incident flux and angle of ions and/or neutral etchants on surfaces at microscale.^[54–57,62,65,88] (b) The ion reflection or scattering from microscopically roughened feature surfaces on incidence is responsible for the evolution of surface roughness with time during etching, because it tends to concentrate incident ions onto the bottom (or the valley) of the feature,^[87] thus resulting in an increase in roughness to its

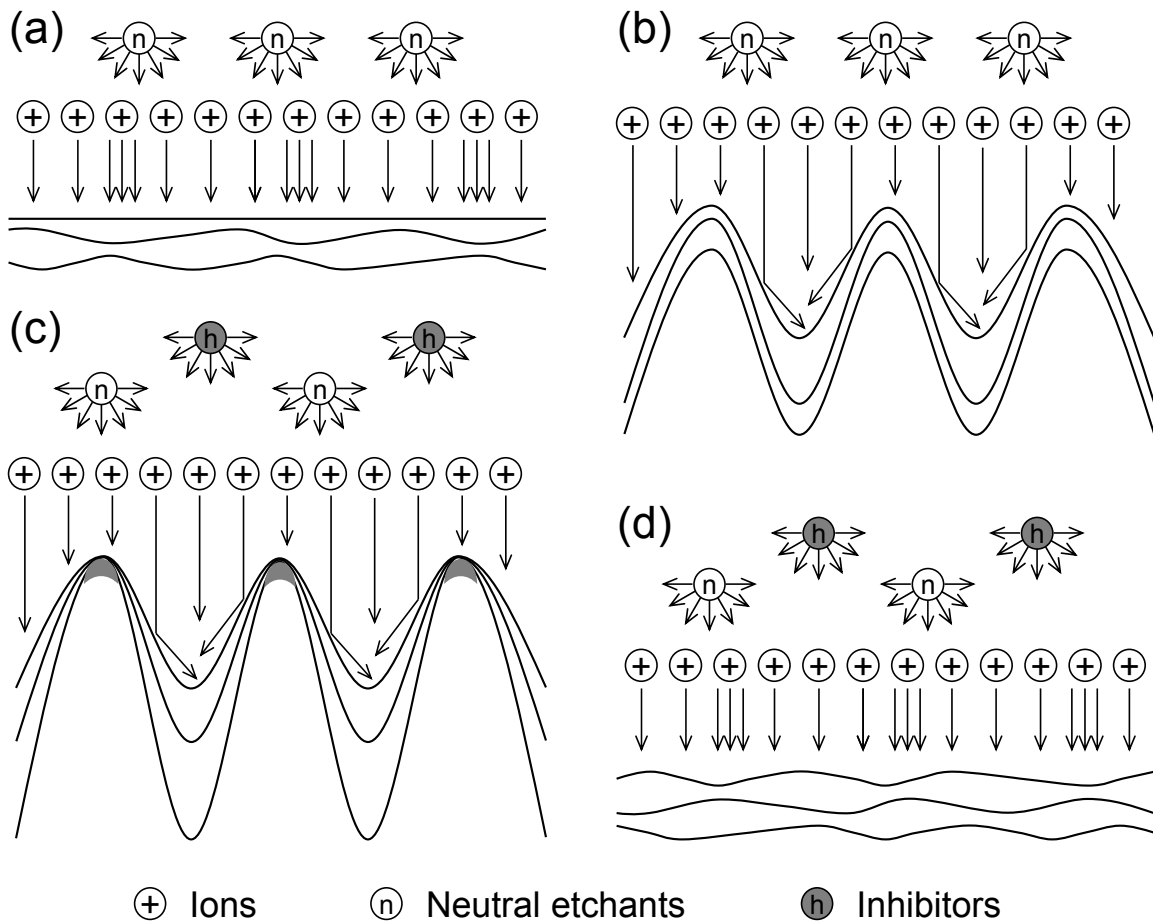


Fig. 4.13. Schematic of the mechanisms responsible for surface roughening during plasma etching of Si discussed and proposed: (a) the low-level stochastic roughening occurs during etching, owing intrinsically to the temporal as well as spatial uniformity of the incident flux and angle of ions and/or neutral etchants on surfaces at microscale. (b) The ion reflection or scattering from microscopically roughened feature surfaces on incidence is responsible for the evolution of surface roughness with time during etching, which tends to be limited by the shadowing effects of the feature for neutral etchants. (c) The continuous increase of the roughness with time (roughening mode) is attributed to the effects of a small amount of incoming etch inhibitors such as oxygen, which tend to locally form surface passivation layers (or micromasks) and inhibit etching thereon, owing to the shadowing for neutral inhibitors. (d) In situations where the predominant ion fluxes are those with reduced reflection probabilities on surfaces, the roughness tends to remain at a low level of stochastic roughening (smoothing or non-roughening mode), whether there are incoming etch inhibitor fluxes or not. Note that in these illustrations [particularly in (a) and (d)], the cross section is not in scale and the vertical scale is much less than the lateral one, and that in (b) and (c), the increase of the lateral extent of the roughness with time is not illustrated for simplicity.

vertical as well as lateral extent. However, the evolution of the roughness would be limited by the shadowing effects of the feature for neutral etchants, where the deeper the feature, the lower

is the etchant flux onto the bottom of the feature. (c) The continuous increase of the roughness with time (roughening mode) is attributed to the effects of a small amount of incoming etch inhibitors, such as oxygen and etch products/byproducts: they stick and/or deposit preferentially on the top (or the hill) of the feature, owing to the shadowing for neutral inhibitors, and so tend to locally form surface passivation layers (or micromasks) and inhibit etching thereon. Such effects of inhibitors are expected to be highly significant for oxygen, because the sputter yields for energetic ions incident are typically one order of magnitude smaller on oxidized than on deposited surfaces. Note that in these illustrations [particularly, in Figs. 4.13(a) and 4.13(d)], the cross section is not in scale and the vertical scale is much less than the lateral one, and that in Figs. 4.13(b) and 4.13(c), the increase of the lateral extent of the roughness with time is not illustrated for simplicity.

On the other hand, (d) in situations where the predominant ion fluxes are those with reduced reflection probabilities on surfaces, the roughness tends to remain at a low level of stochastic roughening (smoothing or non-roughening mode), whether there are incoming etch inhibitor fluxes or not. In practice, the transition from roughening to smoothing modes was found to occur at increased E_i in the present experiments of Si etching in Cl_2 plasmas, corresponding to changes in the predominant ion flux from reactive ions (dominated by Cl_2^+ at low E_i , while SiCl_3^+ at high E_i) to depositive ones (dominated by SiCl^+) thereat.

4.4 Summary

Plasma diagnostics has been performed during Si etching in ICP Cl_2 plasmas at a constant pressure ($P_0 = 20$ mTorr) as a function of rf bias power or ion incident energy in the range $E_i \approx 20$ –500 eV, by varying the feed gas flow rate ($F_0 = 5$ –50 sccm). The changes in surface roughening from the roughening to smoothing modes with increasing E_i were found to correspond approximately to changes in the predominant ion flux from feed gas ions Cl_x^+ to ionized etch products SiCl_x^+ caused by increased etch rates at increased E_i , in view of the results of plasma diagnostics such as OES, FTIR, and QMS to characterize the plasma during etching; more precisely, the changes in the predominant ion flux from reactive ions (dominated by Cl_2^+ at low E_i , while SiCl_3^+ at high E_i) to depositive ones (dominated by SiCl^+) at increased E_i .

The low-level surface roughening during plasma etching, usually giving self-affine fractal surfaces, is generally ascribed to the stochastic roughening that originates intrinsically from the

temporal as well as spatial uniformity of the incident flux and angle of ions and/or neutral etchants on surfaces at microscale.^[54–57,62,65,88] Possible mechanisms for the evolution of surface roughness during etching were further discussed with the help of Monte Carlo-based ASCeM-3D simulations of the surface feature evolution and classical MD simulations of etch fundamentals for Si etching in Cl₂ plasmas. A comparison of the etch rate and rms surface roughness between experiments and ASCeM-3D simulations indicated that the ASCeM-3D reproduces well the increase in etch rate and rms roughness with increasing E_i at low $E_i < E_p$ (roughening mode) in experiments, while it does not reproduce the almost linear increase in rms roughness with time during etching thereat; on the other hand, the ASCeM-3D does not reproduce the substantial decrease in rms roughness with increasing E_i at higher $E_i > E_p$ (smoothing mode) in experiments, although it reproduces well the continuous increase in etch rate with E_i thereat, and in a sense, it reproduces the quasi-steady rms roughness soon after the start of etching thereat.

In these situations, the ASCeM-3D with the ion reflection switched off in the simulation exhibited a substantial decrease in rms surface roughness of Si down to a low level < 0.4 nm (almost independently of E_i) without a significant change in etch rate, which is in agreement with experiments at high $E_i > E_p$. These imply that the ion reflection or scattering from microscopically roughened feature surfaces on incidence plays a crucial role in plasma-induced surface roughening, particularly in the evolution of surface roughness with time during etching; correspondingly, the change in the predominant ion flux from reactive to depositive ions at increased E_i is probably responsible for the change in surface roughening from the roughening to smoothing modes with increasing E_i , because the ion reflection probability on surfaces is significantly lowered for depositive ions as compared to that for reactive ones, as indicated by the MD simulations concerned. Moreover, the ASCeM-3D simulations taking into account incoming etch inhibitor fluxes of oxygen exhibited a continuous increase in rms surface roughness of Si with time, where the rms roughness is increased and the etch rate is decreased with increasing oxygen flux added; the decrease in etch rate is attributed to the surface oxidation that occurs, while the increase in roughness is to local surface oxidation or the local formation of oxide micromasks on Si surfaces during etching. These imply that a small amount of impurity oxygen of the order of $\Gamma_o^0/\Gamma_i^0 \approx 10^{-3}$ (or $\Gamma_o^0/\Gamma_n^0 \approx 10^{-5}$) is presumably responsible for the almost linear increase in rms roughness with time during etching in experiments at low $E_i < E_p$; in practice, the origin of oxygen concerned is attributed to O impurities sputtered from the

dielectric window of the ICP reactor chamber under plasma-on conditions, and the effects of oxygen may be reduced at increased $E_i > E_p$, owing to the increased removal yields for O adsorbed through energetic ion bombardment as well as to the reduced effects of ion reflection thereat.

Chapter 5

Surface Smoothing and Threshold for Initial Surface Roughness

In Chapter 4, we revealed the mechanisms for two modes of surface roughening during ICP etching of blank (or planar) Si substrates in Cl_2 with the help of several plasma diagnostics, ASCeM-3D simulations, and classical MD simulations, where the results indicated that the mode transition from the roughening to smoothing modes is ascribed primarily to reduced effects of the ion reflection on surfaces owing to a change of incident ion species. In these three decades, a number of experimental^[49,50,52,53,55,58,59,61–64,67] and theoretical/numerical^[51,54–57,60,61,66,67,86–88,182] studies have also been performed to interpret the mechanisms for the roughness formation and evolution during plasma etching of blank (or planar) Si substrates. However, these studies were concerned with initially planar substrate surfaces.

In fabrication processes of advanced 3D device structures such as FinFETs, more plasma etch steps are required than in those of conventional planar FETs,^[15,17] where LER and LWR^[76,77] occur on the fin sidewalls in fin etch processes,^[15,80] and the conducting channel of

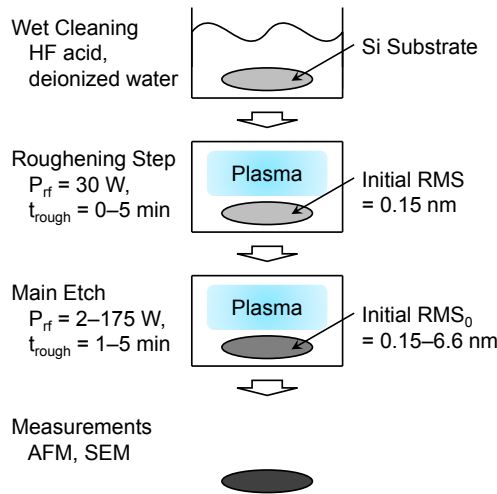


Fig. 5.1. Experimental procedure in this chapter, including a surface-roughening step at $P_{rf} = 30$ W (or $E_i \approx 120$ eV) prior to the main etch. The plasma exposure time of the roughening step was varied in the range $t_{rough} = 0-5$ min, to vary the initial surface roughness of Si substrates in the range $RMS_0 \approx 0.15-6.6$ nm.

FinFETs is formed on top and sidewall surfaces of the fin, which leads to the variability in transistor performance;^[78] moreover, in the following gate etch processes, the surface roughness is formed at the feature bottom, in addition to LER and LWR formed on the gate sidewalls, which is responsible for recess and damage in substrates,^[81] and in turn, also leads to the variability in transistor performance. Therefore, to suppress and minimize the surface roughness of FinFETs by more precise control of plasma etching, a deeper understanding of plasma–surface interactions is required for the formation and evolution of it.

In this chapter, we report on the evolution of the roughness on pre-etched or pre-roughened Si substrates during ICP Cl_2 plasma etching, with attention being placed on the effects of the initial surface roughness. Experiments were performed under the same conditions as in previous ones, except that pre-roughened substrates were used as the etching samples; in addition, the roughness of etched surfaces was quantified by the rms roughness and PSD distribution.

5.1 Experimental Procedure

Figure 5.1 shows an experimental procedure in this chapter. To achieve the plasma etching of pre-roughened substrates, we employed a surface-roughening step prior to the main etch, where planar substrates were roughened by Cl_2 plasmas in the roughening mode at $P_{rf} = 30$ W (or $E_i \approx 120$ eV). The plasma exposure time of the roughening step was varied in the range $t_{rough} = 0-5$

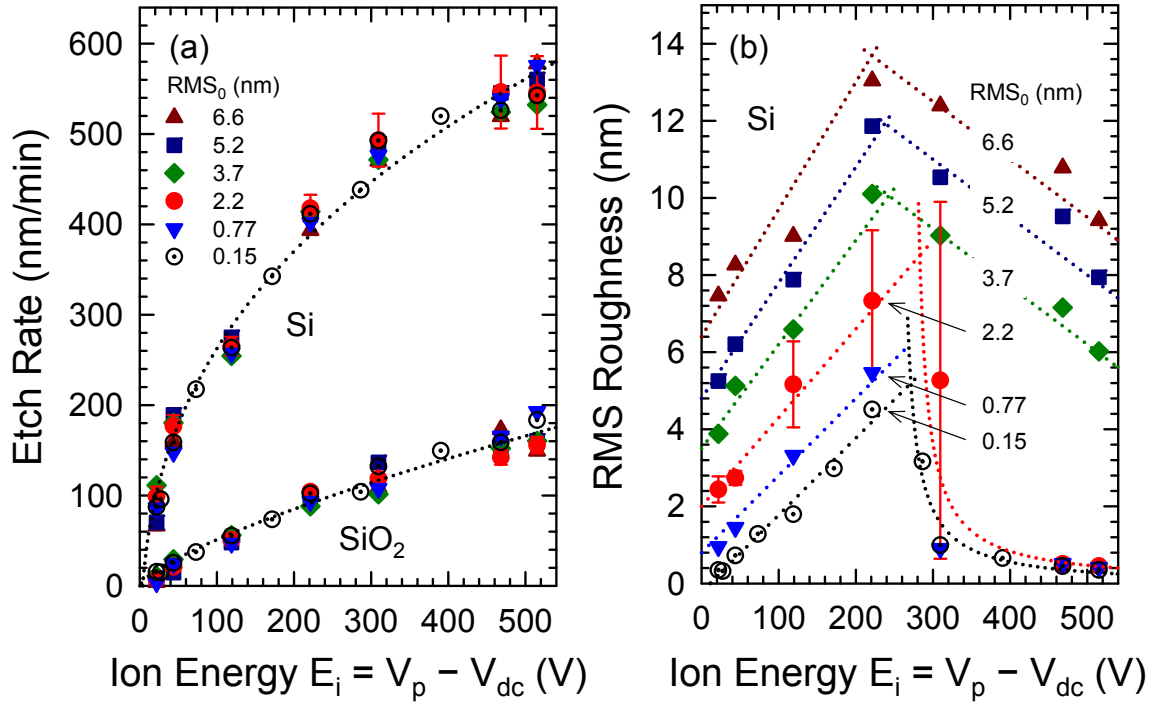


Fig. 5.2. (a) Etch rates of Si and SiO₂ and (b) rms surface roughness of Si as a function of ion incident energy in the range $E_i \approx 22\text{--}520$ eV, obtained in ICP Cl₂ plasma etching ($t_{\text{etch}} = 2$ min) for six different initial roughnesses of $\text{RMS}_0 \approx 0.15\text{--}6.6$ nm, under typical operating conditions of $P_{\text{ICP}} = 450$ W, $P_0 = 20$ mTorr, $F_0 = 20$ sccm, and $T_s = 20^\circ\text{C}$ (the same conditions as in Fig. 3.1). The rms roughness shown is that measured for the AFM scan area $1 \times 1 \mu\text{m}^2$, and the dotted lines are for guiding the eyes only. Note that the data for $\text{RMS}_0 \approx 0.15$ nm are same as those for $F_0 = 20$ sccm in Fig. 3.3.

min, to vary the initial surface roughness of Si substrates in the range $\text{RMS}_0 \approx 0.15\text{--}6.6$ nm, as shown in Fig. 3.6.

5.2 Roughness Evolution on Pre-roughened Surfaces

Figure 5.2 shows the etch rates of Si and SiO₂ and the rms surface roughness of Si as a function of ion incident energy in the range $E_i \approx 22\text{--}520$ eV, obtained in ICP Cl₂ plasma etching ($t_{\text{etch}} = 2$ min) for six different initial roughnesses of $\text{RMS}_0 \approx 0.15\text{--}6.6$ nm. The error bars (shown typically for $\text{RMS}_0 = 2.2$ nm) represent the variation in the raw data for more than ten etching experiments using sample wafers with different as well as similar resistivities, where the data

point at $E_i = 310$ eV has a large error bar, corresponding to a transition from roughening to smoothing mode. The results indicate that for any RMS_0 , as E_i is increased, the Si and SiO_2 etch rates increase, and the etch selectivity of Si over SiO_2 decreases, where the etch rates are independent of RMS_0 , implying that the surface reaction kinetics are not affected by surface roughness; on the other hand, the rms roughness of etched Si surfaces increases, peaks at $E_i = E_p \approx 220$ eV (where the higher the RMS_0 , the larger the increase in roughness), and then decreases. It should be noted that at high $E_i > 470$ eV, the rms roughness is decreased down to a low level of stochastic roughening (< 0.4 nm) for $\text{RMS}_0 < 2.2$ nm; in particular, it becomes lower than RMS_0 for weakly roughened surfaces ($0.77 < \text{RMS}_0 < 2.2$ nm), while it is higher than RMS_0 for highly roughened surfaces ($\text{RMS}_0 > 3.7$ nm). It further noted that at a given low $E_i < E_p$ (roughening mode), the rms roughness is higher for increased RMS_0 ; on the other hand, at a given high $E_i > E_p$ (smoothing mode), the rms roughness remains almost unchanged for varying $\text{RMS}_0 < 2.2$ nm, while it is higher for increased $\text{RMS}_0 > 3.7$ nm. These imply that smoothing of initially roughened surfaces is achieved by plasma etching or plasma exposure in the smoothing mode, and that a threshold $\text{RMS}_{0,\text{th}} \approx 3$ nm exists for the surface smoothing.

Figure 5.3 shows typical AFM and SEM images of the Si surfaces etched in ICP Cl_2 plasmas ($t_{\text{etch}} = 2$ min) with two different $E_i \approx 220$ and 470 eV and three different $\text{RMS}_0 \approx 0.15$, 2.2, and 6.6 nm, corresponding to the data of Fig. 5.2. Note that images of initial Si surfaces ($t_{\text{etch}} = 0$ or before etching) are also shown for reference. In the smoothing mode ($E_i = 470$ eV), both AFM and SEM images indicate visually surface smoothing for weakly roughened surfaces ($\text{RMS}_0 = 2.2$ nm). On the other hand, the images for highly roughened surfaces ($\text{RMS}_0 = 6.6$ nm) are significantly different from those for wet cleaned ($\text{RMS}_0 = 0.15$ nm) and weakly roughened surfaces, exhibiting the roughness of significantly large lateral extent; in particular, the SEM image exhibits large hole or crater like structures (~ 300 nm in diameter).

Figure 5.4 shows the angularly averaged PSD distributions $P(k)$ for three different $\text{RMS}_0 \approx 0.15$, 2.2, and 6.6 nm, obtained from the PSD analysis of AFM images of the Si surfaces etched in ICP Cl_2 plasmas ($t_{\text{etch}} = 2$ min) at four different $E_i \approx 22$ –470 eV. Also shown is the PSD distribution of initial Si surfaces ($t_{\text{etch}} = 0$) for reference. Note that the AFM images for this PSD analysis are acquired on a scan area of $5 \times 5 \mu\text{m}^2$ with the resolution of 512×512 pixels (a pixel size of 9.8 nm), which corresponds to the spatial frequency ranging from $k = 0.0002$ to 0.0512 nm^{-1} in the reciprocal space. It is generally appreciated that for the PSD curve, the parameters of interest are:^[50,63,64,88] the plateau height value w_0 at low k related to the vertical

5.2 Roughness Evolution on Pre-roughened Surfaces

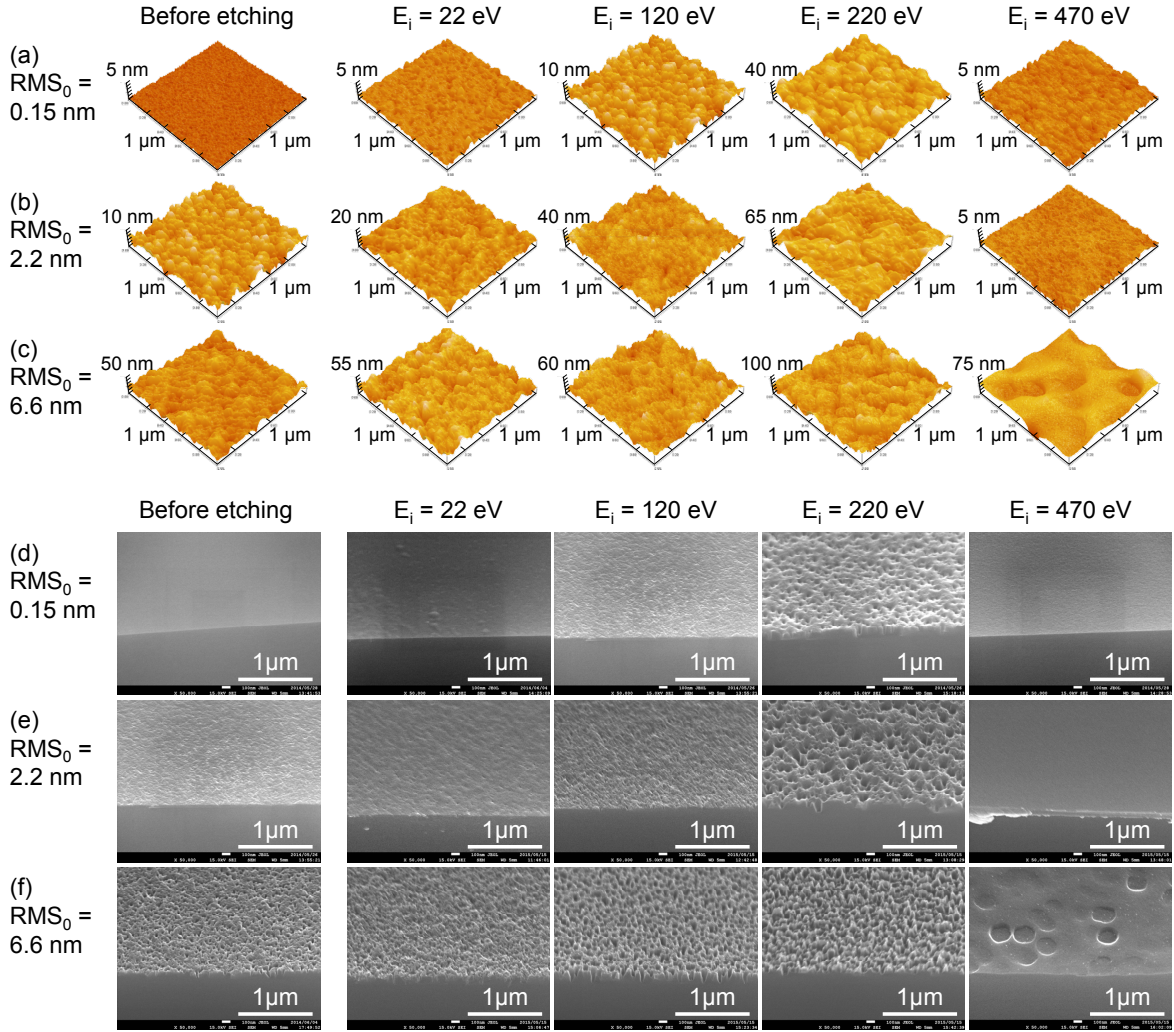


Fig. 5.3. Typical (a)–(c) AFM and (d)–(f) SEM images of the Si surfaces etched in ICP Cl_2 plasmas ($t_{\text{etch}} = 2$ min) with four different ion incident energies of $E_i \approx 22$ –470 eV and three different initial surface roughnesses of $\text{RMS}_0 \approx 0.15$, 2.2, and 6.6 nm, corresponding to the data of Fig. 5.2. Inset is an image of initial Si surfaces prior to etching ($t_{\text{etch}} = 0$) for reference. Note that the data for $\text{RMS}_0 \approx 0.15$ nm are same as those for $t_{\text{etch}} = 2$ min in Fig. 3.8.

height or depth of roughened surface features [$P(k) \approx w_0$ at $k < k_0$], and the correlation length ξ_0 ($= 1/k_0$) that defines the lateral size of the roughness; moreover, the curve at high k gives a fractal or self-affine nature of the roughness [$P(k) \approx K/k^\eta$ at $k > k_0$],^[139,148–151] where K is the spectral strength and the exponent η is a constant linked to the fractal dimension of the surface.

In the PSD analysis for wet cleaned surfaces ($\text{RMS}_0 = 0.15$ nm), the $P(k)$ curves indicate that the plateau value w_0 , spectral strength K , and correlation length ξ_0 increase monotonically with increasing $E_i < 220$ eV (roughening mode), corresponding to the increase in both vertical

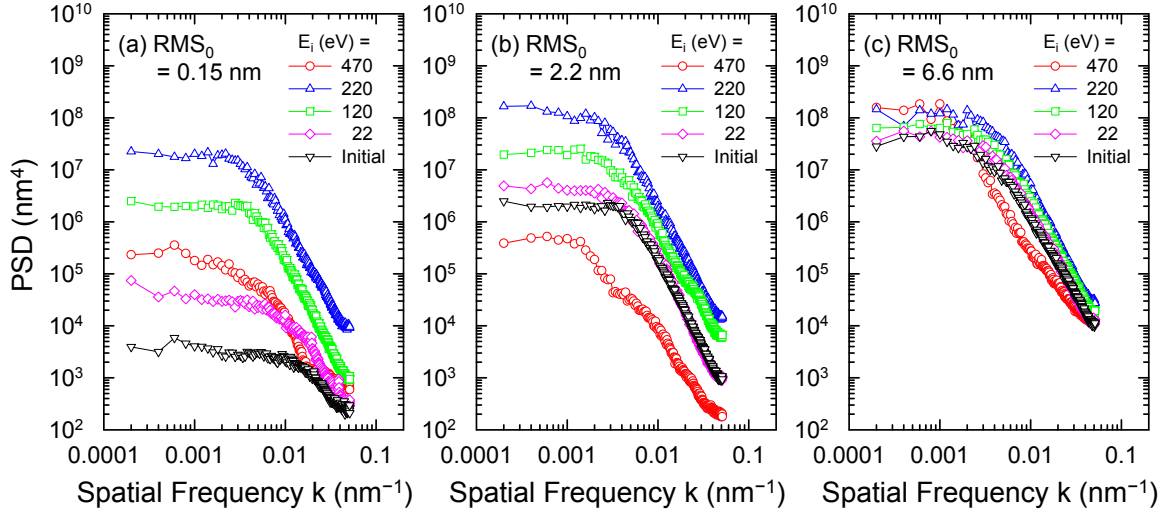


Fig. 5.4. Angular averaged PSD distributions $P(k)$ for three different initial surface roughnesses of $\text{RMS}_0 \approx$ (a) 0.15, (b) 2.2, and (c) 6.6 nm, obtained from the PSD analysis of AFM images of the Si surfaces etched in ICP Cl_2 plasmas ($t_{\text{etch}} = 2$ min) with four different ion incident energies of $E_i \approx 22$ –470 eV under the same conditions as in Fig. 5.2. Also shown is the PSD distribution of initial Si surfaces prior to etching ($t_{\text{etch}} = 0$) for reference. Note that the AFM images for the PSD analysis were acquired on a scan area of $5 \times 5 \mu\text{m}^2$ with the resolution of 512×512 pixels (a pixel size of 9.8 nm).

and lateral roughness; on the other hand, at further increased $E_i = 470$ eV (smoothing mode), the w_0 and K are decreased down to a low level of stochastic roughening, where the ξ_0 is further increased. Moreover, at low $E_i < 220$ eV, the $P(k)$ tail at high frequencies ($k > k_0 = 1/\xi_0$) exhibits a self-affine surface similar to that of the initial surface with the fractal-linked constant of $\eta \approx 3$ (marginal fractal),^[139] while at high $E_i = 470$ eV, the $P(k)$ exhibits a similar self-affine surface of $\eta \approx 3$ at high frequencies ($k > k_0' \approx 0.01 \text{ nm}^{-1}$) in addition to a second self-affine surface of $\eta \approx 1$ (extreme fractal)^[139] at middle frequencies ($k_0' > k > k_0 = 1/\xi_0 \approx 0.002 \text{ nm}^{-1}$).

In the PSD analysis for weakly roughened surfaces ($\text{RMS}_0 = 2.2$ nm), the $P(k)$ curves exhibit the similar E_i dependence to those for wet cleaned surfaces ($\text{RMS}_0 = 0.15$ nm) as mentioned above, where the w_0 and K increase and then decrease and the ξ_0 increases with increasing E_i . It should be noted here that at high $E_i = 470$ eV (smoothing mode), the $P(k)$ magnitude becomes lower than that of the initial surface, corresponding to the surface smoothing as shown in Figs. 5.2 and 5.3; moreover, the $P(k)$ curve is similar to that for $\text{RMS}_0 = 0.15$ nm at $E_i = 470$ eV, and thus, the smoothed surface has the same properties (RMS and

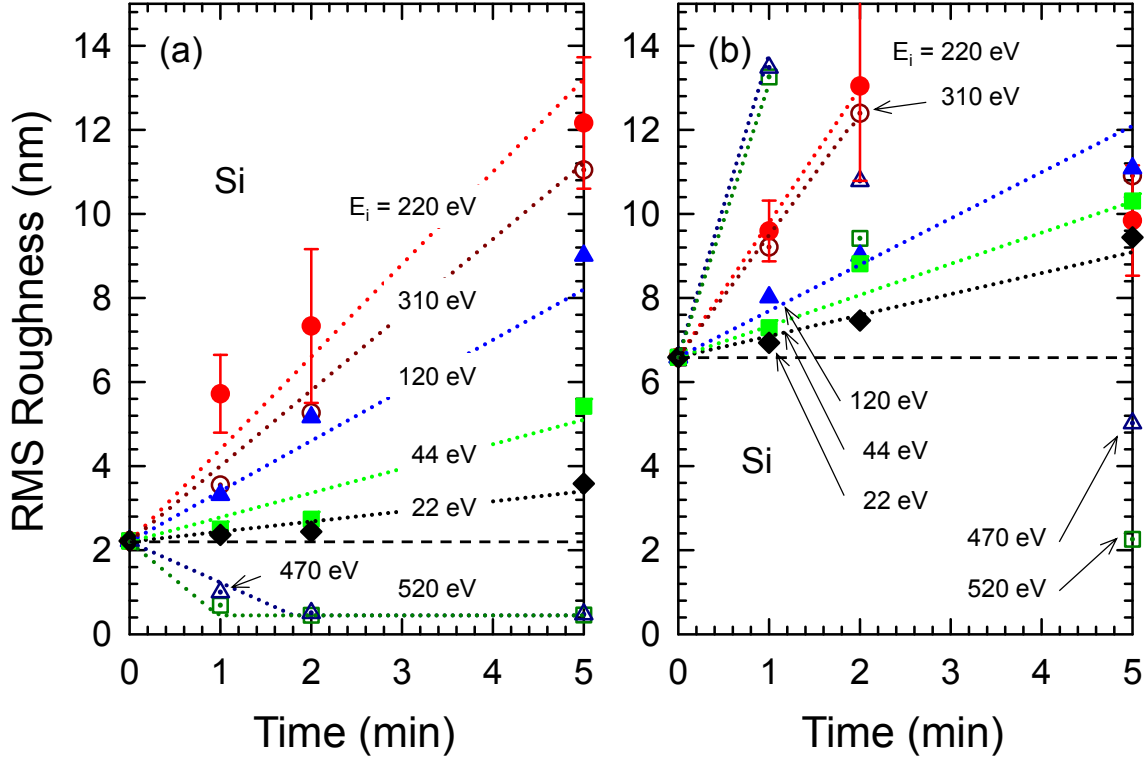


Fig. 5.5. RMS surface roughness of Si as a function of etching or plasma exposure time in the range $t_{\text{etch}} = 0\text{--}5$ min, obtained in ICP Cl_2 plasma etching for two different initial surface roughnesses of $\text{RMS}_0 \approx$ (a) 2.2 and (b) 6.6 nm at seven different ion incident energies of $E_i \approx 22\text{--}470$ eV under the same conditions as in Fig. 5.2. Note that the corresponding results for $\text{RMS}_0 \approx 0.15$ nm is shown in Fig. 3.9. The rms roughness shown is that measured for the AFM scan area of $1 \times 1 \mu\text{m}^2$ as in Fig. 5.2, and the dotted lines are for guiding the eyes only.

PSD) as the stochastically roughened surface. In the PSD analysis for highly roughened surfaces ($\text{RMS}_0 = 6.6$ nm), at $E_i < 220$ eV, the similar E_i dependence is observed as mentioned above for $\text{RMS}_0 = 0.15$ and 2.2 nm; on the other hand, at $E_i = 470$ eV, the behaviors of the $P(k)$ curve are significantly different, where the w_0 becomes larger than that for the initial surface, while the K at high frequencies ($k > k_0 \approx 1/\xi_0 = 0.002 \text{ nm}^{-1}$) becomes slightly lower. These results imply that the large lateral roughness ($\xi_0 > 500$ nm) cannot be smoothed by the plasma etching, and so a threshold for initial correlation length of the roughness ($\xi_{0,\text{th}} \approx 500$ nm), as well as initial rms roughness, may exist for the surface smoothing.

Figure 5.5 shows the rms roughness of Si as a function of etching or plasma exposure time in the range $t_{\text{etch}} = 0\text{--}5$ min, obtained in ICP Cl_2 plasma etching for two different $\text{RMS}_0 \approx 2.2$

and 6.6 nm at seven different $E_i \approx 22\text{--}470$ eV. Note that the corresponding results for wet cleaned surfaces ($\text{RMS}_0 = 0.15$ nm) is shown in Fig. 3.9. In this figure, the rms roughness at $t_{\text{etch}} = 0$ corresponds to the RMS_0 and the error bars (shown typically for $E_i = 220$ eV) have the same properties as those in Fig. 5.2. The results indicate that for weakly roughened surfaces ($\text{RMS}_0 = 2.2$ nm), at low $E_i < E_p \approx 220$ eV (roughening mode), the rms roughness increases almost linearly with time, where the higher the E_i , the larger is the increase in roughness; in addition, at $E_i = 310$ eV (transition point from the roughening to smoothing mode), it also increases almost linearly with time. On the other hand, at higher $E_i > 470$ eV (smoothing mode), the RMS decreases to a low level of stochastic roughening (< 0.4 nm), where the higher the E_i , the larger is the decrease in roughness; and then reaches quasi-steady state ($t_{\text{etch}} > 1\text{--}2$ min). In contrast, for highly roughened surfaces ($\text{RMS}_0 = 6.6$ nm), at any E_i investigated, the RMS increases almost linearly with time. Note that the decreases of RMS ($t_{\text{etch}} = 5$ min at $220 < E_i < 310$ eV and $t_{\text{etch}} > 2$ min at $E_i > 470$ eV) may occur owing to the extremely large lateral roughness, where the extent of roughness is larger than the AFM scan area of $1 \times 1 \mu\text{m}^2$, and thus, the roughness cannot be captured by the AFM measurements; in practice, the extremely large hole or crater like structures ($\sim 1 \mu\text{m}$ in diameter) are observed by the SEM measurements (not shown).

5.3 Mechanisms for Surface Smoothing

As mentioned in Sec. 4.4.1, in etching of planar substrate, it was considered that smooth surfaces of stochastic roughening were achieved by reduced effects of the ion reflection on surfaces. **Figure 5.6** shows the rms roughness of Si as a function of etching or plasma exposure time in the range $0 \leq t \leq 30$ s for $\text{RMS}_0 \approx 3$ nm at $E_i = 500$ eV, obtained through ASCeM-3D simulations with a reduced ion reflection probability of $R_i = 0.8$.^[89] Inset are typical surface features of Si at $t_{\text{etch}} = 0, 5,$ and 25 s after the start of etching in Cl_2 plasmas. Calculations were performed for square substrates 50 nm on a side, with an incoming ion flux and a neutral reactant-to-ion flux ratio of $\Gamma_i^0 = 1.0 \times 10^{16} \text{ cm}^{-2}\text{s}^{-1}$ and $\Gamma_n^0/\Gamma_i^0 = 100$, respectively, in the absence of incoming oxygen and etch products/byproducts ($\Gamma_o^0 = \Gamma_p^0 = 0$);^[88] in addition, the ion and neutral (or gas) temperature were assumed to be $k_B T_i = 0.5$ eV and $T_g = 500$ K, respectively, together with the dopant concentration $N_d = 1.0 \times 10^{18} \text{ cm}^{-3}$ and surface temperature $T_s = 320$ K of substrates. The results indicate that the rms roughness decreases

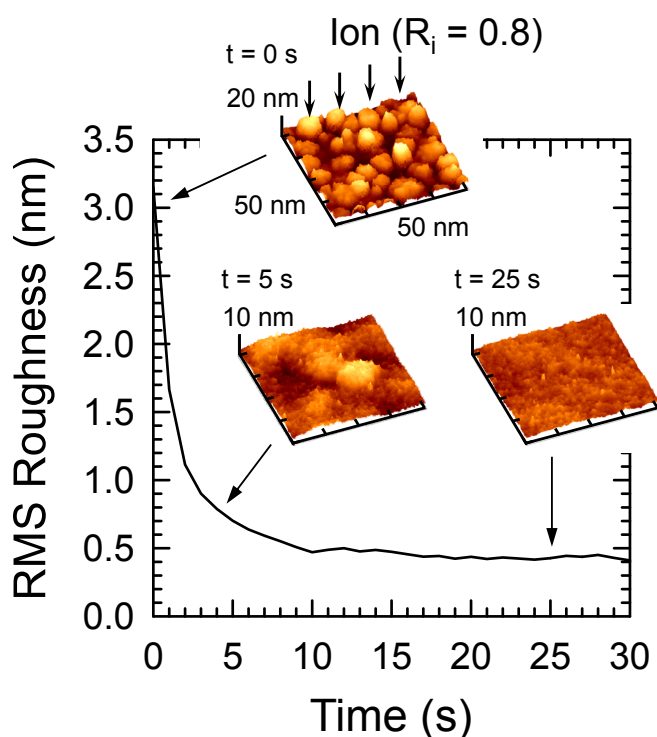


Fig. 5.6. RMS surface roughness of Si as a function of etching or plasma exposure time in the range $0 \leq t \leq 30$ s for an ion incident energy of $E_i = 500$ eV and an initial surface roughness $RMS_0 \approx 3.0$ nm, obtained through ASCeM-3D simulations with an ion reflection probability of $R_i = 0.8$.^[89] Inset are typical surface features of Si at $t = 0, 5,$ and 25 s after the start of etching in Cl_2 plasma.

down to a low level of stochastic roughening (< 0.4 nm) and then reaches the quasi-steady state, being well consistent with the results of etching experiments for weakly roughened surfaces ($RMS_0 = 2.2$ nm) in the smoothing mode ($E_i > 470$ eV) as shown in Fig. 5.5(a). Thus, it is concluded that the surface smoothing of the weakly roughened surfaces is achieved with the same mechanisms proposed in Chapter 4.

5.4 Summary

Evolution of the roughness on pre-roughened surfaces has been investigated during Si etching in ICP Cl_2 plasmas, with emphasis being placed on the effects of initial roughness. Experiments were performed as a function of ion incident energy in the range $E_i \approx 22$ – 470 eV, by varying the initial rms surface roughness of Si surfaces in the range $RMS_0 \approx 0.15$ – 6.6 nm (or the plasma exposure time in the surface-roughening step prior to the main etch in the range $t_{rough} = 0$ – 5 min). The experimental results indicated that the etch rate of Si was independent of RMS_0 , implying that the surface reaction kinetics were not affected by surface roughness. The RMS increased

with increasing $E_i < E_p \approx 220$ eV (roughening mode) for a whole RMS_0 range investigated, where at a given E_i , it increased with increasing RMS_0 ; on the other hand, it decreased with increasing $E_i > E_p$ (smoothing mode) for a whole RMS_0 range investigated, where at a given E_i , it was decreased down to a low level of stochastic roughening (< 0.4 nm) for the weakly roughened surfaces ($0.77 < RMS_0 < 2.2$ nm), while it is higher than RMS_0 for the highly roughened surfaces ($RMS_0 > 3.7$ nm). In particular, at $E_i = 470$ eV, the PSD distribution for $RMS_0 = 2.2$ nm exhibited the same curve as the stochastically roughened surface, where the magnitude became lower than that of initial surface; on the other hand, it for $RMS_0 = 6.6$ nm exhibited the different behaviors, where the plateau value became larger than that of the initial surface, while the spectral strength at high frequencies ($k > k_0 \approx 1/\xi_0 = 0.002$ nm⁻¹) became slightly lower. These results implied that surface smoothing can be achieved by plasma etching, and that a threshold for initial rms roughness or vertical roughness ($RMS_{0,th} \approx 3$ nm) and/or initial correlation length of the roughness or lateral roughness ($\xi_{0,th} \approx 500$ nm) exists for the surface smoothing. In addition, for weakly roughened surfaces ($RMS_0 = 2.2$ nm), at low $E_i < 310$ eV, the RMS increased almost linearly with the plasma exposure time, while at high $E_i > 470$ eV, it decreased down to a low level of stochastic roughening (< 0.4 nm) and then became a quasi-steady state ($t_{etch} > 1-2$ min), being well consistent with ASCeM-3D simulation for $RMS_0 \approx 3$ nm with reduced effects of ion reflection ($R_i = 0.8$); on the other hand, for highly roughened surfaces ($RMS_0 = 6.6$ nm), at any E_i investigated, the RMS increased with time, where large hole or crater like structures were formed on the etched surfaces at high $E_i > 220$ eV. These results implied that the ion reflection on microscopically roughened feature surfaces owing to a change of incident ion species plays a crucial role in the surface smoothing as well as roughening.

Chapter 6

Surface Rippling by Oblique Ion Incidence during Plasma Etching

When low energy ion beams bombard materials, the surface often develops a periodic pattern or ripple structure, depending on ion incident angle θ_i , ion flux, and surface conditions.^[183] The phenomenon of sputtering by off-normal ion beams has been known for more than a hundred years,^[184] and used to modify surface morphology. The mechanisms for surface rippling in response to ion incidence angle θ_i have so far been studied to interpret the experiments of the interaction of keV ion beams with surfaces, using a continuum model^[183,185–191] and Monte Carlo simulation.^[183,192,193] The ripple orientation and wavelength depending on θ_i were first predicted by a continuum model of Bradley and Harper (B–H),^[185] taking into account a competition between roughening caused by surface curvature-dependent sputtering and smoothing caused by surface diffusion of atoms. The B–H model was then extended by adding a few mechanisms such as ion reflection or scattering,^[186] ion-induced surface diffusion,^[188] geometrical shadowing,^[187] and redeposition of sputtered atoms,^[190] to further interpret the ripple wavelength and amplitude depending on ion energy, ion flux, and surface temperature,

along with the evolution of ion-sputtered surface features. The Monte Carlo simulation of beam–surface interactions was also utilized to interpret the experiments, including all the mechanisms taken in the B–H model.^[183,192,193]

In ULSI and MEMS device fabrications, the surface ripple structure caused by off-normal ion incidence during plasma etching corresponds the sidewall roughness such as LER and LWR,^[76,77] while the formation mechanisms are not exactly similar to those for ion beam sputtering, because of the lower ion incident energy $E_i < 1$ keV and the existence of reactive neutrals. Moreover, in pattern transfer by plasma etching, ions scattered from feature sidewalls contribute to undesirable profile anomalies such as undercutting, bowing, and microtrench.^[194,195] Several experimental studies concerned with off-normal ion incidence during etching have been performed by using plasma beam,^[62,68,69,75] while the experiments of plasma etching with off-normal ion incidence are not yet achieved, where the ions are injected to the substrate surfaces at off-normal angles directly through the sheath with reactive neutrals. In addition, some Monte Carlo-based feature profile simulations have been performed taking into account reactive neutrals, and found that at $\theta_i = 45^\circ$ or oblique ion incidence, periodic or ripple structure are formed on surfaces perpendicularly to the direction of ion incidence; in contrast, at $\theta_i > 75^\circ$ or grazing incidence, small ripples or slitlike grooves are formed on surfaces parallel to the direction of ion incidence.^[65,69,87,88] The simulation results further indicated that such surface roughening and rippling in response to ion incidence angle depend significantly on ion energy and incoming fluxes of neutral reactants, oxygen, and etch byproducts.^[88] However, the mechanisms are not yet fully understood because of the lack of the data of etching fundamentals as a function of ion incident angle to precisely capture the effects of off-normal incidence on surface reaction kinetics.

In this chapter, ripple formation is experimentally demonstrated by plasma etching with off-normal ion incidence. Experiments were performed by using sheath control plates^[196] for achieving off-normal ion incidences, and the other experimental setup is same as in previous Chapters 3–5. In Sec. 6.1, the detail of the sheath control plates is described and the ion incidence angle onto the sample surface to be etched is estimated by using an electrostatic particle-in-cell (PIC) simulation.^[197] In Sec. 6.2, ripple formation by off-normal ion incidence during plasma etching is experimentally demonstrated and the PSD analysis of the surfaces is performed for characterization of the ripple structures. Moreover, in Sec. 6.3, the Si etch yield as a function of ion incident angle is measured for a better understanding of plasma–surface

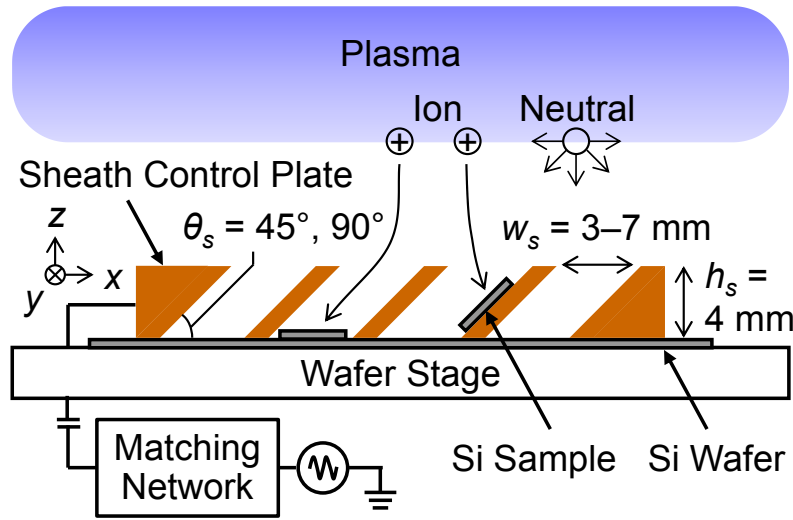


Fig. 6.1. Schematic of the sheath control plate made of metal, used for achieving the off-normal ion incidence on sample Si surfaces during plasma etching. The sheath control plate has slits (width $w_s = 3\text{--}7$ mm, height $h_s = 4$ mm, and angle $\theta_s = 45^\circ$ and 90°) to vary the sheath structures thereon and thus to vary the ion trajectories from the plasma onto sample surfaces, where reactive neutrals also diffuse to the surfaces.

interactions that are responsible for the nanoscale surface roughening and rippling during plasma etching.

6.1 Sheath Control Plate for Off-Normal Ion Incidence

Figure 6.1 shows a schematic of the sheath control plate made of metal,^[196] used for achieving the off-normal ion incidence on sample Si surfaces during plasma etching. The sheath control plate has slits (width $w_s = 3\text{--}7$ mm, height $h_s = 4$ mm, and angle $\theta_s = 45^\circ$ and 90°) to vary the sheath structures thereon and thus to vary the ion trajectories from the plasma onto sample surfaces, where reactive neutrals also diffuse to the surfaces. In the experiments, the sheath control plate set on the wafer was electrically connected to the wafer stage, and samples were placed on the bottom and/or side of the slits.

Figure 6.2 shows the typical 2D electrostatic potential distribution and ion trajectories under typical conditions ($w_s = 7$ mm, $\theta_s = 45^\circ$, and $V_{dc} = -500$ V), calculated by using the 2D [Cartesian coordinates ($x\text{--}z$)] electrostatic PIC method,^[197] where the particles considered were Cl_2^+ ions only and the electron density distribution was assumed to be determined by the

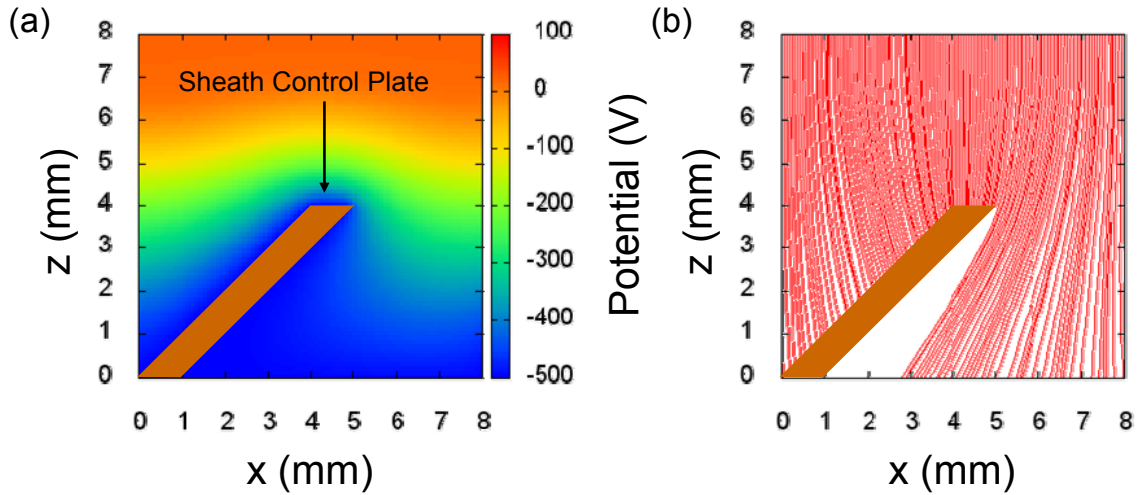


Fig. 6.2. Typical (a) 2D electrostatic potential distribution and (b) ion trajectories under typical conditions ($w_s = 7$ mm, $\theta_s = 45^\circ$, and $V_{dc} = -500$ V), calculated by using the 2D [Cartesian coordinates (x - z)] electrostatic PIC method.

Boltzmann relation. It is noted that a negative dc bias voltage is applied to the wafer stage and sheath control plate in this calculation, while an rf one is applied to there in experiments. The calculation method is detailed in Appendix C. The calculations indicated that the electrostatic potential distribution is varied by the sheath control plate, and that the off-normal ion incidence is achieved onto the bottom and side of the slits. **Figure 6.3** shows the ion incidence angle θ_i on the slit sides as a function of the dc bias voltage on the wafer stage and sheath control plates in the range $|V_{dc}| = 100$ – 500 V, obtained through the PIC calculations with three different slit widths of $w_s = 3, 5,$ and 7 mm for two different slit angles of $\theta_s = 45^\circ$ and 90° . Note that the plot points and error bars indicate the average and the maximum/minimum of the ion incident angles through the whole area of the slit sides, respectively, and that $\theta_i = 0^\circ$ corresponds to normal incidence onto sample surfaces. The results indicate that for both θ_s , the average ion incident angle increases with decreasing bias voltage, and the difference of the maximum and minimum decreases. The results further indicate that the incident angle increases with decreasing slit width. Therefore, it is implied that the ion incident angle onto the sample surfaces can be controlled by the geometries of the sheath control plates.

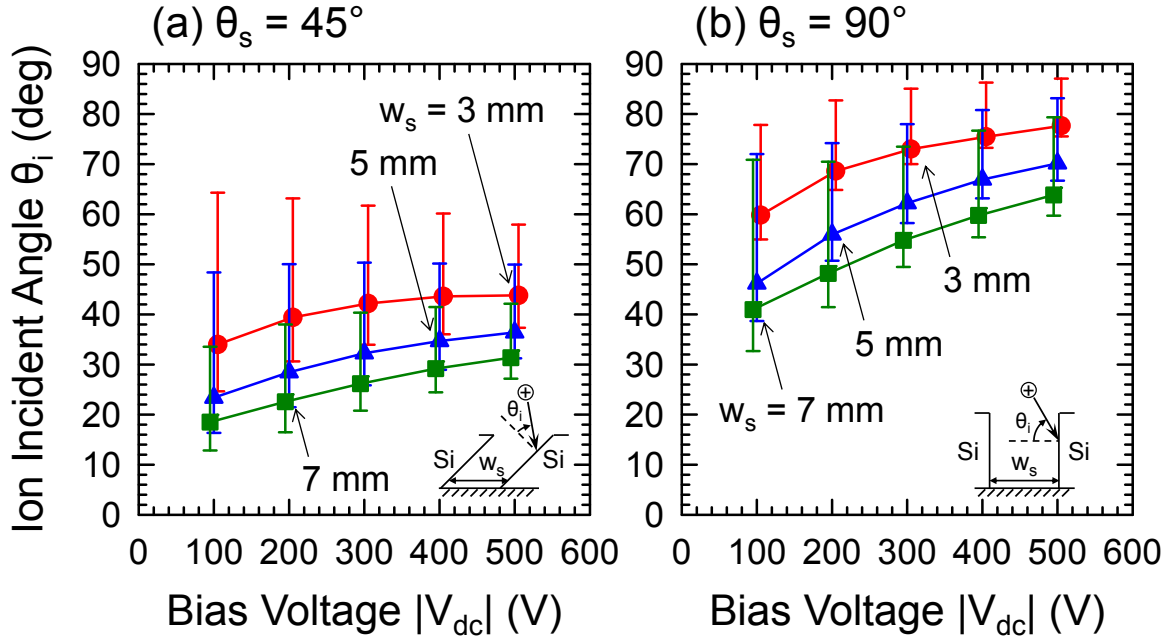


Fig. 6.3. Ion incidence angle θ_i on the slit sides as a function of the dc bias voltage on the wafer stage and sheath control plates in the range $|V_{dc}| = 100\text{--}500$ V, obtained through the PIC calculations for three different slit widths of $w_s = 3, 5,$ and 7 mm and two different slit angles of $\theta_s =$ (a) 45° and (b) 90° . Note that the plot points and error bars indicate the average and the maximum/minimum of the ion incident angles through the whole area of the slit sides, respectively, and that $\theta_i = 0^\circ$ corresponds to normal incidence onto sample surfaces.

6.2 Experimental Demonstration of Surface Rippling

Figure 6.4 shows the typical AFM and SEM images (top view) of Si surfaces etched, measured after 3- and 5-min etching in ICP Cl_2 plasmas at $P_{rf} = 150$ W (or an ion incident energy $E_i = V_p - V_{dc} \approx 500$ eV) under typical operating conditions of $P_{ICP} = 450$ W, $P_0 = 20$ mTorr, $F_0 = 20$ sccm, and $T_s = 20^\circ\text{C}$ (the same conditions as in Fig. 3.1). The geometries of the sheath control plates used are $(w_s, \theta_s) = (5 \text{ mm}, 45^\circ)$ and $(3 \text{ mm}, 90^\circ)$, where ion incident angles estimated are $\theta_i \approx 40^\circ$ and 80° , respectively. These results indicate that at $\theta_i \approx 40^\circ$ or oblique ion incidence, ripple structures are formed on surfaces perpendicularly to the direction of ion incidence; on the other hand, at $\theta_i \approx 80^\circ$ or grazing incidence, small ripples or slit like grooves are formed on surfaces parallel to the direction of ion incidence. These results are qualitatively consistent with our ASCeM-3D simulations for Si etching in Cl_2 plasmas,^[87–89] Monte Carlo-based profile simulations for Ar^+ sputtering of polysilicon and SiO_2 etching in $\text{C}_4\text{F}_8/\text{Ar}$ plasma,^[65] MD

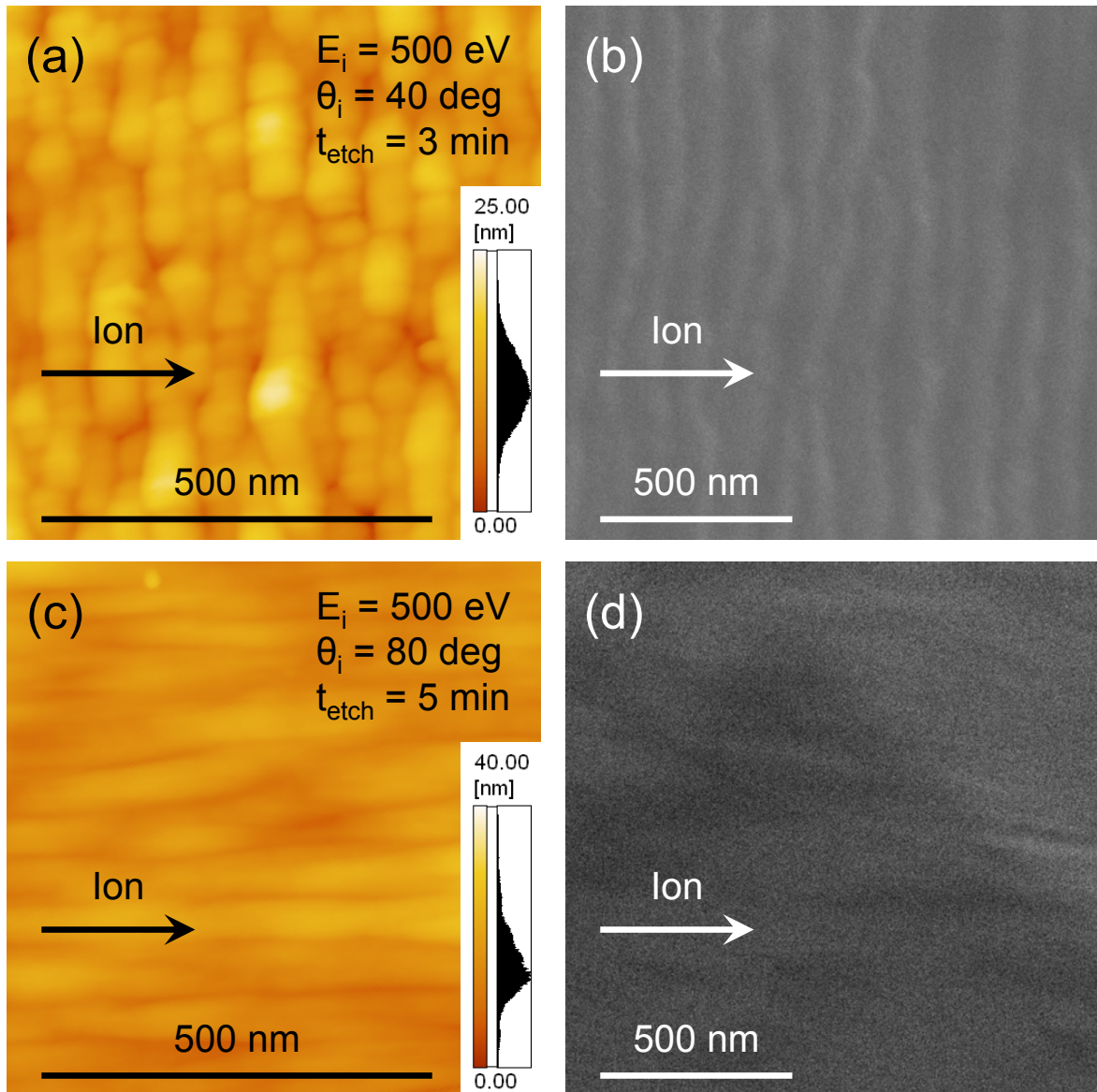


Fig. 6.4. Typical AFM and SEM images (top view) of Si surfaces, measured after (a), (b) 3- and (c), (d) 5-min etching in ICP Cl_2 plasmas at $P_{\text{rf}} = 150$ W (or an ion incident energy $E_i = V_p - V_{\text{dc}} \approx 500$ eV) under typical operating conditions of $P_{\text{ICP}} = 450$ W, $P_0 = 20$ mTorr, $F_0 = 20$ sccm, and $T_s = 20^\circ\text{C}$ (the same conditions as in Fig. 3.1). The geometries of the sheath control plates used are $(w_s, \theta_s) = (5 \text{ mm}, 45^\circ)$ and $(3 \text{ mm}, 90^\circ)$, where ion incident angles estimated are $\theta_i \approx 40^\circ$ and 80° , respectively.

simulations for CF_3^+ ion beam etching of Si,^[66] and Si, SiO_2 , and low- k film etching by Ar plasma beam experiments.^[62]

To further characterize the ripple structures formed on Si surfaces, PSD analysis is performed. **Figure 6.5** shows 1D PSD distributions $P_x(k_x)$ and $P_y(k_y)$ in the x - and y -directions,

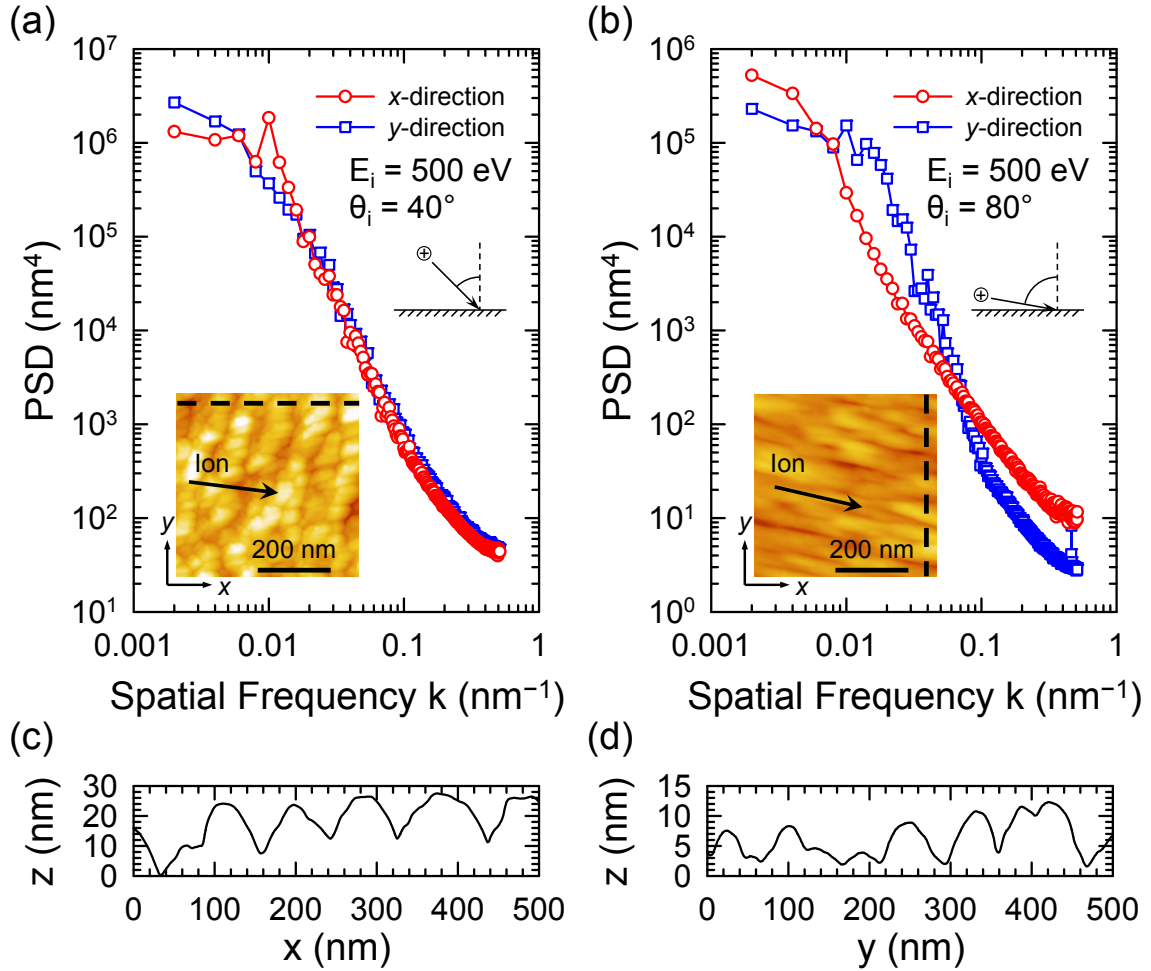


Fig. 6.5. (a), (b) 1D PSD distributions $P_x(k_x)$ and $P_y(k_y)$ in the x - and y -directions, which roughly correspond to parallel and perpendicular directions of the ion incidence, respectively, obtained from the PSD analysis of inset AFM images of the Si surfaces etched in ICP Cl₂ plasma under the same conditions as in Fig. 6.4. Note that the AFM images for the PSD analysis were acquired on a scan area of $0.5 \times 0.5 \mu\text{m}^2$ with the resolution of 512×512 pixels. (c), (d) Cross sectional height distribution along the dashed line indicated in the inset AFM image.

which roughly correspond to parallel and perpendicular directions of the ion incidence, respectively, obtained from the PSD analysis of inset AFM images of the Si surfaces etched in ICP Cl₂ plasma under the same conditions as in Fig. 6.4. The length scale concerned is the side length $W_A = 0.5 \mu\text{m}$ of the AFM scan area with the resolution of 512×512 pixels (a pixel size $L_A = 0.98$ nm), which corresponds to the spatial frequency ranging from $k = 0.002$ to 0.51 nm⁻¹ in the reciprocal space. Also shown is the cross sectional height distribution along the dashed line indicated in the inset AFM image. The analysis indicates that at $\theta_i \approx 40^\circ$ or oblique

ion incidence, $P_x(k_x)$ exhibits a local apparent maximum at the spatial frequency $k_x \approx 0.01 \text{ nm}^{-1}$, corresponding to the periodic or ripple structures of wavelength $\lambda_x = 1/k_x \approx 100 \text{ nm}$ that evolve perpendicularly to the direction of ion incidence. This result is in good agreement qualitatively in our ASCeM-3D simulations^[88] and ion beam sputtering experiments,^[198] while the wavelength of ripple structures obtained in this study is about third larger than in these previous studies. The analysis further indicates that at $\theta_i \approx 80^\circ$ or grazing incidence, $P_y(k_y)$ exhibits several small maxima at frequencies in the range $0.01 < k_y < 0.05 \text{ nm}^{-1}$, corresponding to small ripples or slit like grooves of wavelength in the range $20 < \lambda_y < 100 \text{ nm}$ that evolve parallel to the direction of ion incidence. This result is also consistent with ASCeM-3D simulations.^[88]

6.3 Ion Incident Angle Dependence of Etch Rate

Figure 6.6(a) shows the etch rate of Si as a function of ion incident angle in the range $\theta_i \approx 0^\circ\text{--}50^\circ$, obtained in ICP Cl_2 plasma etching with sheath control plates of $w_s = 3, 5, \text{ and } 7 \text{ mm}$ and $\theta_s = 45^\circ$ for three different ion incident energies of $E_i \approx 100, 200, \text{ and } 500 \text{ eV}$ under otherwise the same conditions as in Fig. 6.4. The results indicate that for any E_i , the etch rate decreases with increasing $\theta_i \approx 0^\circ\text{--}50^\circ$, and at a given θ_i , it is larger for higher E_i as in normal ion incidence. **Figure 6.6(b)** shows the Si yield Y per ion as a function of ion incident angle in the range $\theta_i \approx 0^\circ\text{--}50^\circ$ for three different ion incident energies E_i , which are the data replotted from the preceding Fig. 6.6(a). The yield Y is defined as the total number of Si atoms desorbed from substrate surfaces per ion impact: $Y = \rho_s ER / \Gamma_i$, where the Si atom density of substrate is $\rho_s \approx 5.0 \times 10^{22} \text{ cm}^{-3}$.^[2] It is noted that in the present experiments, the ion flux Γ_i incident on substrate surfaces changes from that at sheath edge $\Gamma_i^0 \approx (0.5\text{--}0.6) \times 10^{16} \text{ cm}^{-2}\text{s}^{-1}$ (mentioned earlier with respect to Fig. 3.1), and thus, it is estimated by using the 2D PIC simulations in this study. The results indicate that for any E_i , the Si yield remains almost unchanged in the whole θ_i range investigated. This angular dependence of the etch yield does not agree with a physical sputtering model,^[62,145,199] where the maximum yield is achieved at $\theta_i \approx 50^\circ\text{--}70^\circ$ owing to increased momentum transfer efficiency in the oblique ion incidence.^[200] On the other hand, it is consistent with a result of reactive ion etching systems,^[145,200–204] where the maximum yield is observed at normal ion incidence, and the yield remains almost unchanged as the incident angle increases and then starts to decrease at $\theta_i \approx 50^\circ\text{--}70^\circ$, because the near normal incident ions create thicker reaction layers on the surface and enhance the generation of volatile etch products.

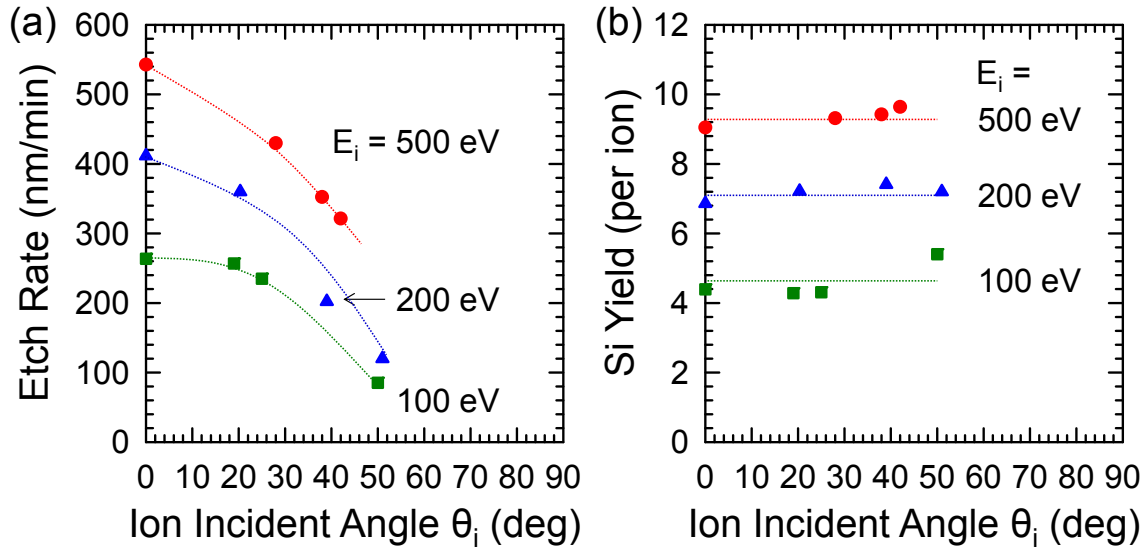


Fig. 6.6. (a) Etch rate of Si as a function of ion incident angle in the range $\theta_i \approx 0^\circ$ – 50° , obtained in ICP Cl_2 plasma etching with sheath control plates of $w_s = 3, 5,$ and 7 mm and $\theta_s = 45^\circ$ for three different ion incident energies of $E_i \approx 100, 200,$ and 500 eV under otherwise the same conditions as in Fig. 6.4. The dotted lines are for guiding eyes only. (b) Si yield per ion as a function of ion incident angle in the range $\theta_i \approx 0^\circ$ – 50° for three different ion incident energies $E_i \approx 100, 200,$ and 500 eV, which are the data replotted from (a).

These angular dependences of etch yield in ion beam etching and plasma etching are demonstrated in our MD simulations.^[97,98,205] **Figure 6.7** shows the Si yield per ion as a function of ion incident angle in the range $\theta_i = 0^\circ$ – 90° , obtained through the MD simulation for Cl^+ ion incidence on Si(100) with different ion energies of $E_i = 20$ – 300 eV and neutral-to-ion flux ratios of $\Gamma_n^0/\Gamma_i^0 = 0$ and 100 , which correspond to ion beam etching and typical plasma etching environment, respectively.^[132,133,206,207] The results indicate that in ion beam etching, at lower $E_i < 100$ eV, the yield remains almost unchanged as ion incident angle increases and decreases at further increased θ_i ; while at higher $E_i > 150$ eV, it increases with increasing θ_i , peaks at $\theta_i = 60^\circ$ – 70° , and then decreases, implying that the physical sputtering dominates the surface reaction kinetics. On the other hand, in plasma etching, at any E_i , as θ_i is increased, the yield remains almost unchanged for $\theta_i < 50^\circ$ – 60° and then decreases at further increased θ_i , being consistent with the experimental results shown in Fig. 6.6(b). Therefore, it is implied that the plasma etching with oblique ion incidence is achieved in the present experiments with the sheath control plates.

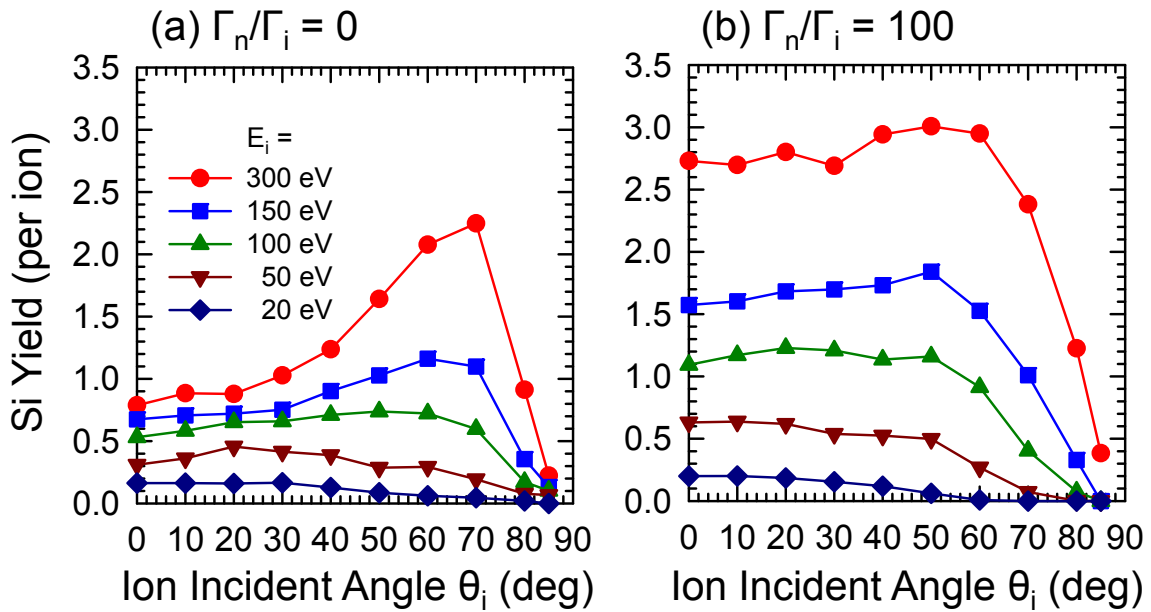


Fig. 6.7. Si yield per ion impact as a function of ion incident angle in the range $\theta_i \approx 0^\circ$ – 90° , obtained through the MD simulation of Cl^+ ion incidence with different ion energies of $E_i = 20$ – 300 eV and neutral-to-ion flux ratios of $\Gamma_n^0/\Gamma_i^0 =$ (a) 0 and (b) 100.

6.4 Summary

Off-normal ion incidence during ICP etching of Si in Cl_2 have been achieved by using sheath control plates made of metal, and the ripple structures formed on the etched surfaces have been demonstrated and analyzed. In the experiments, the sheath control plates were electrically connected to the wafer stage, and Si samples were placed on the side and bottom of the slits. Electrostatic potential distributions thereon and ion trajectories from plasma onto the slits were calculated by 2D PIC simulations, and the ion incident angle and flux onto the sample surfaces were estimated. The experiments demonstrated that at $\theta_i \approx 40^\circ$ or oblique ion incidence, periodic or ripple structures were formed on surface perpendicularly to the direction of ion incidence; on the other hand, at $\theta_i \approx 80^\circ$ or grazing incidence, small ripples or slit like grooves were formed on surfaces parallel to the direction of ion incidence, as predicted in our ASCeM-3D simulations.^[87] Moreover, for any E_i , the Si yield remains almost unchanged in the whole θ_i range investigated ($\theta_i \approx 0^\circ$ – 50°), implying the plasma etching with oblique ion incidence is achieved by using the sheath control plates.

Chapter 7

Concluding Remarks

7.1 Conclusions

Atomic- or nanometer-scale plasma-induced surface roughness and ripple formation have been investigated during Si etching in ICP Cl_2 plasmas, with emphasis being placed on a deeper understanding of plasma–surface interactions that are responsible for. Experiments were performed at a constant pressure ($P_0 = 20$ mTorr) as a function of rf bias power or ion incident energy in the range $E_i \approx 20\text{--}500$ eV, by varying the feed gas flow rate ($F_0 = 5\text{--}50$ sccm), wafer stage temperature ($T_s = 20\text{--}200^\circ\text{C}$), initial surface roughness ($\text{RMS}_0 \approx 0.15\text{--}6.6$ nm), and etching or plasma exposure time ($t_{\text{etch}} = 1\text{--}20$ min), including several plasma and surface diagnostics. Further experiments were performed to achieve the oblique ion incidence during plasma etching with sheath control plates made of metal. Moreover, numerical simulations were also performed to interpret the experimental results by using ASCeM-3D and classical MD. The key findings revealed in this study are listed below.

1. Two modes of plasma-induced surface roughening which occur depending on ion incident energy E_i are found. One of the modes observed is the roughening mode at low

$E_i < 200\text{--}300$ eV, where the rms roughness of etched surfaces increases with increasing E_i , exhibiting an almost linear increase with time during etching ($t < 20$ min); the other is the smoothing mode (or non-roughening mode) at higher E_i , where the rms roughness decreases substantially with E_i down to a low level of RMS < 0.4 nm, reaching a quasi-steady state after some increase at the initial stage ($t < 1$ min). In addition, the transition from the roughening to smoothing modes with increasing E_i are found to correspond approximately to changes in the predominant ion flux from reactive ions (dominated by Cl_2^+ at low E_i , while SiCl_3^+ at high E_i) to depositive ones (dominated by SiCl^+) at increased E_i , which causes the reduced effects of the ion reflection on surfaces.

2. Possible mechanisms for the evolution of surface roughness is summarize as follows: (a) the low-level stochastic roughening occurs during etching, owing intrinsically to the temporal as well as spatial uniformity of the incident flux and angle of ions and/or neutral etchants on surfaces at microscale. (b) The ion reflection or scattering from microscopically roughened feature surfaces on incidence is responsible for the evolution of surface roughness with time during etching, which tends to be limited by the shadowing effects of the feature for neutral etchants. (c) The continuous increase in the roughness with time (roughening mode) is attributed to the effects of a small amount of incoming etch inhibitors, such as oxygen, which tend to locally form surface passivation layers (or micromasks) and inhibit etching thereon, owing to the shadowing for neutral inhibitors. (d) In situations, where the predominant ion fluxes are those with reduced reflection probabilities on surfaces, the roughness tends to remain at a low level of stochastic roughening (smoothing or non-roughening mode), whether there are incoming etch inhibitor fluxes or not.
3. Surface smoothing of pre-roughened substrates is achieved by plasma etching in the smoothing mode ($E_i > 300$ eV); in addition, a threshold for the rms roughness and/or correlation length of initial surfaces is found. For the weakly-roughened surfaces (RMS₀ < 2.2 nm), the roughness decreases with time down to a low level of stochastic roughening (RMS < 0.4 nm) and reaches a quasi-steady state, where the reduced effects of the ion reflection on surfaces contributes the surface smoothing as in etching of blank or planar substrate. On the other hand, for the strongly-roughened surfaces (RMS₀ $>$

3.7 nm), it increases with time, where the large hole or basin like structures (>300 nm in a diameter) are formed on the surfaces.

4. Oblique ion incidence is achieved during plasma etching by using sheath control plates, and the ripple formation on the etched sample surfaces is demonstrated. For $E_i \approx 500$ eV, at $\theta_i \approx 40^\circ$ or oblique ion incidence, periodic or ripple structures are formed on surface perpendicularly to the direction of ion incidence; on the other hand, at $\theta_i \approx 80^\circ$ or grazing ion incidence, small ripples or slit like grooves are formed on surfaces parallel to the direction of ion incidence, as predicted in ASCeM-3D simulations. In addition, the angular dependence of Si yield is in good agreement with that of ion-enhanced etch yield obtained in plasma beam experiments and MD simulations.

7.2 Future Outlooks

Plasma etching technology has continued to evolve from when it became an essential method of pattern transfer for silicon ICs in the 1970s, with developments of advanced equipment and diagnostics techniques which gave a better understanding of plasma–surface interactions. Although plasma etching has become to be able to be applied to processes of various materials and nanometer-scale 3D structures, strict requirements concerned with higher selectivity and less damage/roughness are still imposed on it. To establish plasma processes which satisfy such needs, novel techniques including pulsed-plasma etching,^[208–211] atomic layer etching,^[212–214] and neutral beam etching^[215,216] are studied actively, but a more comprehensive understanding of plasma–surface interactions are required for further developments of them. We believe that the findings in this study concerned with atomic- or nanometer-scale plasma–surface interactions assist the evolution to more sophisticated plasma etching technology for next-generation device fabrications.

Appendix A

Atomic-Scale Cellular Model

Three-dimensional atomic-scale cellular model (ASCeM-3D) is a surface profile simulation model with a cell removal method. For surface advancement or the evolution of interfaces between vacuum and substrate surfaces, any profile simulation needs the dominant reaction mechanisms, or surface chemistry and kinetics of the etching process including ion-induced etching and ion reflection, which control the etching rate. Cell removal methods have a huge advantage over other methods due to their ease of incorporation of the surface processes, which are given by removal and/or addition of particles to the cells concerned.^[182,217] In this appendix, the concepts and techniques of ASCeM-3D for simulating the surface evolution during Si etching in Cl_2/O_2 plasmas are described, which include the simulation domain, particle injection and transport, surface chemistry and kinetics, and surface advancement. The main scheme of the ASCeM has been developed by Osano and co-workers for 2D model^[218–220] and by Tsuda and co-workers from 2D to 3D model.^[84–89]

A.1 Simulation Domain

Figure A.1 shows a schematic of the ASCeM-3D model for Si etching in Cl_2 and Cl_2/O_2 plasmas, together with the coordinate system (x, y, z) presently employed. The simulation domain is a square $W = 50$ nm on a side with a depth of 630 nm, consisting of a number of small cubic cells of atomic size $L = \rho_s^{-1/3} = 2.7 \text{ \AA}$ ($185 \times 185 \times 2333 \approx 8 \times 10^7$ cells in total), where $\rho_s = 5.0 \times 10^{22} \text{ cm}^{-3}$ is the atomic density of Si substrates.^[2] The substrates initially occupy a lower 620-nm-deep layer therein (the substrate surfaces are initially flat, being located 10 nm downward from the top of the domain). The cells are assumed to be rigid, and Si atoms are allocated at the center of substrate cells as a point mass. It should be noted that the atomic-scale cell size L presently employed is one of the prominent features characterizing the ASCeM, being about an order of magnitude smaller than that of other cell-based simulation models.^[60,61,65,67,69] In addition, the ASCeM cannot reproduce phenomena depending on the crystallinity of substrates, because it is not taken in the model.

A.2 Particle Transportation

Energetic ions (Cl^+), neutral reactants or etchants (Cl), reactive neutrals (O), and etch and/or sputter byproducts (SiCl_x , SiCl_xO_y) are considered, which are randomly allocated at the top of the simulation domain, being successively injected therefrom (or from the plasma) onto substrates with given energies, fluxes, and angular distributions; concretely, incoming ions are taken to have a Gaussian-like anisotropic angular distribution around the incident angle θ_i .^[221–223]

$$d\Gamma_i = \Gamma_i^0 G_i(\Theta) \cos \Theta d\Theta, \quad (\text{A.1})$$

where Γ_i^0 is the ion flux onto the substrate and

$$G_i(\Theta) \cos \Theta = \frac{\exp(R)}{\sqrt{\pi}} \left[\frac{\sqrt{R}}{\cos \Theta} \exp\left(-\frac{R}{\cos^2 \Theta}\right) + \frac{\sqrt{\pi}}{2} \operatorname{erf}\left(-\frac{\sqrt{R}}{\cos \Theta}\right) \right] \cos \Theta. \quad (\text{A.2})$$

Here, Θ is the incident angle, $R = eV_s/k_B T_i$ is the ratio of the ion incident energy $E_i = eV_s$ accelerated through the sheath to the ion temperature $k_B T_i$ ($= 0.5$ eV in this study), and

$$\operatorname{erf}(x) = \frac{2}{\sqrt{\pi}} \int_x^\infty \exp(-t^2) dt. \quad (\text{A.3})$$

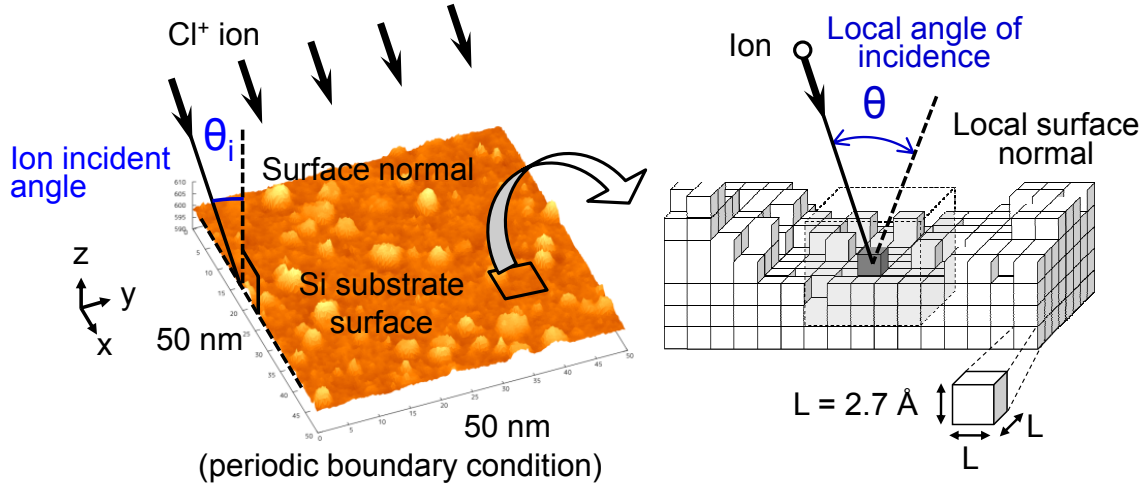


Fig. A.1. Schematic of ASCeM-3D model for simulating plasma–surface interactions and the feature profile evolution during plasma etching, together with the coordinate system (x , y , z) presently employed. The simulation domain is a square 50 nm on a side with an initial depth of 630 nm, which is divided into a number of small cubic cells of atomic size $L = 2.7 \text{ \AA}$. In the figure, θ_i is the ion incidence angle onto substrate surfaces, while θ is the local ion incidence angle on microscopically roughened feature surfaces thereon. The local surface normal on feature surfaces is calculated by the extended four-point technique for $5 \times 5 \times 5$ neighboring cells (125 cells in total) at around the substrate surface cell that the ion reaches.

On the other hand, neutrals have an isotropic velocity distribution. Moreover, etch and/or sputter products are taken to be desorbed from substrate surfaces being etched into vacuum, thermally or isotropically with the so-called cosine distribution;

$$G_d(\Theta_d) \cos \Theta_d = \frac{1}{2} \cos \Theta_d, \quad (\text{A.4})$$

where Θ_d is the desorbed angle of the products; which corresponds to Eq. (A.2) with $R = 0$. These incoming particles and desorbed products are also assumed to be point masses.

Transport of ions and neutrals in the ASCeM-3D is analyzed in three dimensions (x , y , z) with periodic boundary conditions in the horizontal direction, based on single-particle trajectories with three velocity components (v_x , v_y , v_z). The particles are assumed to move straight from the top of the simulation domain onto substrate surfaces and then into microstructures thereon, without collisions with other particles in vacuum, where their transport is calculated every movement of step L , taking into account geometrical shadowing effects of the structure; then, the particles are assumed to reach the surface if there is a Si atom in any of the 26 cells neighboring the cell which the particle concerned is in. The local surface normal

and thus the local angle θ of incidence on microstructural feature surface is calculated by using the extended four-point technique^[86,218,220,224] for $5 \times 5 \times 5$ neighboring cells (125 cells in total) at around the substrate surface cell that the particle reaches, as shown in Fig. A.1; this is one of the key procedures in the cell-based simulations such as ASCeM, because the surface chemistry and kinetics calculations rely crucially on the local incidence angle θ , as mentioned below. Note that $\theta = \theta_i$ for completely planar substrate surfaces. In addition, feature surfaces are taken to be charge neutral during etching, owing to the Auger process for energetic ions incident on surfaces.^[225]

Moreover, the ASCeM-3D takes into account two-body elastic collisions between energetic ions and substrate Si atoms, to analyze the ion reflection or scattering from feature surfaces on incidence into vacuum and the ion penetration into substrates.^[226,227] The analysis is based on the 3D Monte Carlo calculation of ion trajectories according to the momentum and energy conservation through successive collisions with substrate Si atoms; then, the ions reflected from the surface into vacuum move further toward another surfaces of the feature or go out the simulation domain. The interatomic potential for Cl–Si employed is the Ziegler–Biersack–Littmark type.^[228,229] As mentioned below, in calculating the ion-related yields Y_{Si} , Y_{SiCl_x} , and $Y_{\text{SiCl}_x\text{O}_y}$, the ion energy concerned is taken to be its incident energy E_i in the case of penetration, while the energy loss or deposit energy on surface $\Delta E_i = E_i - E_r$ in the case of reflection, where E_r is the ion energy after reflection ($E_r = 0$ corresponds to the case of penetration). It should be noted that the reflection and penetration of energetic ions incident on feature surfaces is a second one of the prominent features characterizing the ASCeM; in practice, without the effects of ion reflection from surfaces on incidence, the ASCeM does not reproduce the evolution of 3D nanoscale surface features such as roughness and ripples as shown Figs. 4.11, 4.12, and 5.7 and that of 2D nanoscale profile anomalies such as microtrench and micropillars as reported previously.^[84,85,230] Here, in the ASCeM calculation, the magnitude of the effects of ion reflection can be modulated artificially by varying the reflection probability of energetic ions, R_i , which is defined as the fraction of the ion reflection calculation scheme switched on; thus, $R_i = 1$ corresponds to the situation in which both penetration and reflection occur based on Monte Carlo method (normal ASCeM calculation), and the effects decrease with decreasing R_i , then $R_i = 0$ corresponds to the situation in which the ion reflection does not occur (or any ion penetrates into the substrate surfaces).

A.3 Surface Chemistry and Kinetics for Si Etching in Cl₂/O₂ Plasmas

The ASCeM-3D takes into account surface chemistry and kinetics on substrate, also based on the 3D Monte Carlo algorithm.^[146,220,224] surface chlorination (or adsorption and reemission of neutrals), chemical etching, ion-enhanced etching, sputtering, surface oxidation, redeposition of etch and/or sputter products desorbed from feature surfaces being etched, and deposition of etch and/or sputter byproducts coming from plasma; the latter three lead to the formation of surface inhibitor or passivation layers, which are taken to be removed by sputtering through energetic ion bombardment. These are assumed to occur on substrate surface cells (or the outermost surface cells), each of which is allowed to contain four Cl, two Cl and one O, or two O atoms at maximum, in addition to one Si atom.

The surface chemistry concerned in this study for Si etching in Cl₂ and Cl₂/O₂ plasmas is summarized in **Tabel A.1**.

Surface chlorination. It is induced by adsorption of neutral reactants Cl, where the sticking probability is taken to be $S_n = 1 - (x + 2y)/4$ on SiCl_xO_y surfaces ($0 \leq x \leq 4$ for $y = 0$, $0 \leq x \leq 2$ for $y = 1$, $x = 0$ for $y = 2$); otherwise neutral Cl atoms are assumed to be reemitted thermally or reflected randomly with a probability $(1 - S_n)$ from the surface to vacuum, which the move further toward another surfaces of the feature or go out of the simulation domain.

Surface oxidation. It is induced by adsorption of strongly reactive O neutrals, where the sticking probability is taken to be $S_o = 1 - y/2$ on SiCl_xO_y surfaces ($0 \leq x \leq 4$ for $y = 0$, $0 \leq x \leq 2$ for $y = 1$, $x = 0$ for $y = 2$); otherwise neutral O atoms are also assumed to be reemitted thermally with a probability $(1 - S_o)$, similarly as for Cl neutrals.

Chemical etching. It is assumed to occur on fully chlorinated SiCl₄ surfaces, and corresponding reaction probability α_{SiCl_4} is taken from the known data depending on surface temperature T_s .^[34]

$$\alpha_{\text{SiCl}_4} = \frac{\rho_{\text{Si}} \text{ER}_{\text{chem}}}{\Gamma_{\text{Cl}}} = \frac{4\rho_{\text{Si}} \nu N_d^\gamma T_s^{1/2}}{\bar{u}} \exp\left(-\frac{E}{k_B T_s}\right), \quad (\text{A.5})$$

where $\text{ER}_{\text{chem}} = \nu N_d^\gamma T_s^{1/2} \exp(-E/k_B T_s)$ is the chemical etch rate for Si in heated Cl₂ gases, $\nu = 4.04 \times 10^{-18} \text{ \AA} \cdot \text{cm}^{3(1+\gamma)} \text{min}^{-1} \text{K}^{-1/2}$, $\gamma = 0.39$, and $E = 4.7 \text{ kcal/mol}$ are constants determined for P-doped poly-Si, and k_B is the Boltzmann constant. In addition, $\Gamma_{\text{Cl}} = (1/4)n_{\text{Cl}}\bar{u}$ is the flux of

Cl atoms incident on surfaces, n_{Cl} is Cl concentration in the gas phase, $\bar{u} = (8k_{\text{B}}T_{\text{g}}/\pi m_{\text{Cl}})^{1/2}$ is the average thermal velocity of Cl atoms with m_{Cl} being the atomic mass of Cl. In this study, the dopant concentration, surface temperature, and gas phase temperature are typically taken to be $N_{\text{d}} = 1.0 \times 10^{18} \text{ cm}^{-3}$, $T_{\text{s}} = 320 \text{ K}$, and $T_{\text{g}} = 500 \text{ K}$, respectively.

Ion-enhanced etching. It occurs through energetic Cl^+ ion incidence on chlorinated surfaces. The yield is taken to be $Y_{\text{SiCl}_x} = (x/4)Y_{\text{SiCl}_4}$ ($1 \leq x \leq 4$), where Y_{SiCl_4} is the etch yield for Cl^+ on Si surfaces chlorine saturated. The yield Y_{SiCl_4} is taken from the known model depending on ion incident energy E_i and local incident angle θ on the surface;^[204]

$$Y_{\text{SiCl}_4} = A \left(\sqrt{E_i - E_r} - E_{\text{th,SiCl}_4} \right) \cdot f(\theta), \quad (\text{A.6})$$

where the threshold energy and coefficient are assumed to be $E_{\text{th,SiCl}_4} = 12.0 \text{ eV}$ and $A = 0.353$, respectively,^[146] in view of the experiments of Cl_2 plasma beam,^[146] Cl^+ plus Cl/Cl_2 beam,^[200] and Cl^+ beam etching^[200,231] as well as the analytical models for sputtering.^[232] In addition, the angular dependence $f(\theta)$ is expressed as follows:

$$f(\theta) = \begin{cases} 1 & (0 < \theta < 25^\circ) \\ \frac{(90 - \theta)}{65} - \frac{(\theta - 25)(\theta - 90)}{5000} & (25 < \theta < 90^\circ) \end{cases}. \quad (\text{A.7})$$

Sputtering. It occurs through energetic Cl^+ ion incidence on pure Si surfaces and oxidized Si surfaces. The yield for pure Si surfaces is assumed to be

$$Y_{\text{Si}} = A \left(\sqrt{E_i - E_r} - E_{\text{th,Si}} \right) \cdot g(\theta), \quad (\text{A.8})$$

where the threshold energy is taken to be $E_{\text{th,Si}} = 29.7 \text{ eV}$ (Ref. [232]) and the angular dependence is expressed as follows:^[182]

$$g(\theta) = -81.70 \cos^5 \theta + 224.03 \cos^4 \theta - 208.19 \cos^3 \theta + 67.569 \cos^2 \theta - 0.711 \cos \theta - 0.0242. \quad (\text{A.9})$$

In addition, the yield for oxidized Si surfaces is assumed to be $Y_{\text{SiCl}_x\text{O}} = 4[(2+x)/4]^2 Y_{\text{SiO}_2}$ ($0 \leq x \leq 2$), in view of the experiments of Ar^+ plus Cl/Cl_2 beam etching of Si and SiO_2 ,^[143] where the yield Y_{SiO_2} is the sputter yield for Cl^+ on SiO_2 ;

$$Y_{\text{SiO}_2} = (1/\beta) \cdot A \left(\sqrt{E_i - E_r} - E_{\text{th,SiO}_2} \right) \cdot g(\theta), \quad (\text{A.10})$$

where the threshold energy $E_{\text{th,SiO}_2} = 40 \text{ eV}$,^[143] and the etch selectivity is assumed to be $\beta = Y_{\text{Si}}/Y_{\text{SiO}_2} = 8$ at $E_i = 100 \text{ eV}$ and $\theta = 0^\circ$, in view of the experiments of Ar^+ beam incidence on Si

and SiO₂ in Cl₂.^[233]

Deposition. The etch/sputter products desorbed from feature surfaces being etched and the incoming byproducts from the plasma are assumed to stick or deposit on all feature surfaces with probabilities $S_q = 0.05$ and $S_p = 0.05$, respectively; otherwise they are reemitted thermally with probabilities $1 - S_q$ and $1 - S_p$, similarly as for neutrals.

A.4 Surface Advancement

Si atoms are removed from the substrate surface cells, together with the neutrals contained therein (or the outermost surface cells become empty), when the etching/sputtering causes the desorption of etch/sputter products. On the other hand, Si atoms are newly allocated to the cells neighboring the outermost surface cells, together with the neutrals accompanied, when the redeposition and/or deposition of etch/sputter products occur. In addition, Si-containing cells floating in vacuum often occur during simulation, which are removed by percolation according to the Hoshen–Kopelman algorithm,^[234–236] this is a second one of the key procedures in the cell-based simulations such as ASCeM, because unphysically roughened surface features tend to occur without percolation.

Table A.1 Surface chemistry during Si etching in Cl_2 and Cl_2/O_2 plasmas.

Reaction	Process ^(a)	Coefficient ^(b)
(R1) Surface chlorination	$\text{Si}(s) + x\text{Cl}(s) + y\text{O}(s) + \text{Cl}(g) \rightarrow \text{Si}(s) + (x+1)\text{Cl}(s) + y\text{O}(s)$ $(0 \leq x \leq 4 \text{ for } y = 0, 0 \leq x \leq 2 \text{ for } y = 1, x = 0 \text{ for } y = 2)$	$S_n = 1 - (x + 2y)/4$
(R2) Surface oxidation	$\text{Si}(s) + x\text{Cl}(s) + y\text{O}(s) + \text{O}(g) \rightarrow \text{Si}(s) + x\text{Cl}(s) + (y+1)\text{O}(s)$ $(0 \leq x \leq 4 \text{ for } y = 0, 0 \leq x \leq 2 \text{ for } y = 1, x = 0 \text{ for } y = 2)$	$S_o = 1 - y/2$
(R3) Chemical etching	$\text{Si}(s) + 3\text{Cl}(s) + \text{Cl}(g) \rightarrow \text{SiCl}_4(g)$	α_{SiCl_4}
(R4) Ion-enhanced etching	$\text{Si}(s) + x\text{Cl}(s) \rightarrow \langle \text{Ion bombardment} \rangle \rightarrow \text{SiCl}_x(g) \quad (1 \leq x \leq 4)$	$Y_{\text{SiCl}_x} = (x/4)Y_{\text{SiCl}_4}$
(R5) Sputtering	$\text{Si}(s) \rightarrow \langle \text{Ion bombardment} \rangle \rightarrow \text{Si}(g)$	Y_{Si}
	$\text{Si}(s) + x\text{Cl}(s) + \text{O}(s) \rightarrow \langle \text{Ion bombardment} \rangle \rightarrow \text{SiCl}_x\text{O}(g) \quad (0 \leq x \leq 2)$	$Y_{\text{SiCl}_x\text{O}} = 4[(2+x)/4]^2 Y_{\text{SiO}_2}$
	$\text{Si}(s) + 2\text{O}(s) \rightarrow \langle \text{Ion bombardment} \rangle \rightarrow \text{SiO}_2(g)$	Y_{SiO_2}
(R6) Redeposition of etch and/or sputter products	$\text{SiCl}_x\text{O}_y(g) \rightarrow \text{Si}(s) + x\text{Cl}(s) + y\text{O}(s) \quad (0 \leq x \leq 4 \text{ for } y = 0, 0 \leq x \leq 2 \text{ for } y = 1, x = 0 \text{ for } y = 2)$	S_q
	$\text{SiCl}_x\text{O}_y(g) \rightarrow \text{Si}(s) + x\text{Cl}(s) + y\text{O}(s) \quad (0 \leq x \leq 4 \text{ for } y = 0, 0 \leq x \leq 2 \text{ for } y = 1, x = 0 \text{ for } y = 2)$	S_p

^(a) (s) denotes species on the surface, (g) denotes species in the gas phase.

^(b) S_j ($j = n, o, p, q$) denotes the sticking probability of neutrals, α_{SiCl_4} the reaction probability, Y_j ($j = \text{SiCl}_x, \text{Si}, \text{SiCl}_x\text{O}, \text{SiO}_2$) the etch/sputter yield.

Appendix B

Classical Molecular Dynamics

Classical molecular dynamics (MD) simulation is an useful technique to simulate physical and chemical interactions of low temperature plasmas with surfaces.^[237] MD simulations follow the detailed motion of sets of interacting atoms through integration of atomic equations of motion, using interatomic potentials that can account for bond breaking and formation that result when energetic species from the plasma impact surfaces. In this appendix, the interatomic potential model employed in this study and the model of the MD-based plasma etching simulation are described.^[96–97,205] The main scheme of the MD simulation used in this study has been developed by Ohta and co-workers.^[90–95]

B.1 Improved Stillinger-Weber Interatomic Potential for Si/Cl System

Any potential-energy function Φ describing interactions between N identical particles (or atoms) can generally be resolved into one-, two-, three-, ..., and N -body contributions $v_1, v_2, v_3, \dots, v_n$ as follows:^[238]

$$\Phi(1, \dots, N) = \sum_i v_1(i) + \sum_{i < j} v_2(i, j) + \sum_{i < j < k} v_3(i, j, k) + \dots + v_n(1, \dots, n), \quad (\text{B.1})$$

where the first term v_1 corresponds to interaction with a wall or external potentials. In order that this representation be useful in the usual types of theoretical modeling, it is necessary that the last term v_n converge quickly to zero with increasing n . When the potential is expressed as a function of position of the atoms, $\Phi(\mathbf{r}_1(t), \mathbf{r}_2(t), \dots, \mathbf{r}_n(t))$, the force acting on atom i at a given time t is calculated as a negative gradient of the potential,

$$\mathbf{f}_i(t) = - \frac{\partial}{\partial \mathbf{r}_i} \Phi(\mathbf{r}_1(t), \mathbf{r}_2(t), \dots, \mathbf{r}_n(t)), \quad (\text{B.2})$$

and the motion of atom i is determined by the Newton's equation of motion;

$$\frac{d^2 \mathbf{r}_i(t)}{dt^2} = \frac{\mathbf{f}_i(t)}{m_i}, \quad (\text{B.3})$$

where m_i is mass of atom i .

The interatomic potential employed in this study has a form of the Stillinger–Weber (SW) potential function for covalent bonds, which can qualitatively represent a diamond lattice structure of crystalline Si.^[238] The total potential energy is expressed by the summation of the two- and three-body potential functions.^[238–241]

$$\Phi = \sum_{i < j} v_2(i, j) + \sum_{i < j < k} v_3(i, j, k). \quad (\text{B.4})$$

By introducing energy and length units ε and σ , the two- and three-body functions are reduced (or normalized) as follows:

$$v_2(i, j) = v_2(r_{ij}) = \varepsilon u_2\left(\frac{r_{ij}}{\sigma}\right), \quad v_3(i, j, k) = v_3(\mathbf{r}_i, \mathbf{r}_j, \mathbf{r}_k) = \varepsilon u_3\left(\frac{\mathbf{r}_i}{\sigma}, \frac{\mathbf{r}_j}{\sigma}, \frac{\mathbf{r}_k}{\sigma}\right). \quad (\text{B.5})$$

Here, $r_{ij} = |\mathbf{r}_{ij}| = |\mathbf{r}_i - \mathbf{r}_j|$ denotes the distance between the atoms i and j . In the Si/Cl system, $\varepsilon = 2.1692$ eV and $\sigma = 2.0951$ Å. The reduced two-body potential function u_2 represented as

$$u_2(\bar{r}_{ij}) = \begin{cases} A_{ij} (B_{ij} \bar{r}_{ij}^{-p_{ij}} - \bar{r}_{ij}^{-q_{ij}}) \exp\left[\frac{C_{ij}}{\bar{r}_{ij} - a_{ij}}\right] & \text{if } \bar{r}_{ij} < a_{ij}, \\ 0 & \text{otherwise} \end{cases}, \quad (\text{B.6})$$

where $\bar{r}_{ij} = r_{ij}/\sigma$, and a_{ij} is corresponds to cutoff radius. In addition, the reduced three-body potential function u_3 represented as

$$u_3 = h_{jik}(\bar{r}_{ij}, \bar{r}_{ik}, \theta_{jik}) + h_{ijk}(\bar{r}_{ji}, \bar{r}_{jk}, \theta_{ijk}) + h_{ikj}(\bar{r}_{ki}, \bar{r}_{kj}, \theta_{ikj}), \quad (\text{B.7})$$

where if $\bar{r}_{ij} < a_{jik}^j$ and $\bar{r}_{ij} < a_{jik}^k$, then

B.1 Improved Stillinger-Weber Interatomic Potential for Si/Cl System

$$h_{jik}(\bar{r}_{ij}, \bar{r}_{ik}, \theta_{jik}) = \lambda_{jik} \exp\left[\frac{\gamma_{jik}^j}{\bar{r}_{ij} - a_{jik}^j} + \frac{\gamma_{jik}^k}{\bar{r}_{ik} - a_{jik}^k}\right] \times \left|\cos\theta_{jik} + \frac{1}{3}\right|^{2\alpha_{jik}}, \quad (\text{B.8})$$

otherwise, $h_{jik}(\bar{r}_{ij}, \bar{r}_{ik}, \theta_{jik}) = 0$. Here, $\theta_{jik} = \mathbf{r}_{ij} \cdot \mathbf{r}_{ik} / (r_{ij}r_{ik})$ is the angle between \mathbf{r}_{ij} and \mathbf{r}_{ik} . The parameters for Si/Cl system used in this study are summarized in **Table B.1**.^[51] In practice, the repulsive interaction is overestimated in the original SW model, when a halogen atom is surrounded by more than three Si atoms, or when a high-energy halogen penetrates deeper into substrates. Thus, an improved potential form of the SW model^[94,95] is employed in this study, which involves a correction term for the three-body potential function, to overcome this disadvantage and to predict surface reaction kinetics more accurately:

$$\Phi = \varepsilon \sum_{i < j} u_2 + \varepsilon \sum_{i < j < k} g_i(w_i) h_{jik}. \quad (\text{B.9})$$

Here, $g_i(w_i)$ is a correction factor for the three-body potential function,

$$g_i(w_i) = \begin{cases} 1 & w_i \leq 2 \\ 1 + s(w_i) \left(\frac{2}{w_i} - 1 \right) & 2 < w_i < 3 \\ \frac{2}{w_i} & 3 \leq w_i \end{cases}, \quad (\text{B.10})$$

Table B.1 Two- and three-body potential parameters for Si/Cl system.^[51]

u_{SiSi}	A_{SiSi}	7.049556277	u_{SiCl}	A_{SiCl}	28.0	u_{ClCl}	A_{ClCl}	8.611
	B_{SiSi}	0.6022245584		B_{SiCl}	0.67		B_{ClCl}	0.789
	C_{SiSi}	1		C_{SiCl}	1.3		C_{ClCl}	0.5795
	p_{SiSi}	4		p_{SiCl}	2.2		p_{ClCl}	6
	q_{SiSi}	0		q_{SiCl}	0.9		q_{ClCl}	5
	a_{SiSi}	1.8		a_{SiCl}	1.8		a_{ClCl}	2.0862
h_{SiSiSi}	λ_{SiSiSi}	16.404	h_{SiSiCl}	λ_{SiSiCl}	15	h_{SiSiCl}	λ_{SiSiCl}	15
	$\gamma_{\text{SiSiSi}}^{\text{Si}}$	1.0473 (Si)		$\gamma_{\text{SiSiCl}}^{\text{Si}}$	1		$\gamma_{\text{SiSiCl}}^{\text{Si}}$	1.0
	$a_{\text{SiSiSi}}^{\text{Si}}$	1.8 (Si)		$a_{\text{SiSiCl}}^{\text{Si}}$	1.8		$a_{\text{SiSiCl}}^{\text{Si}}$	1.8
	α_{SiSiSi}	1		$\gamma_{\text{SiSiCl}}^{\text{Cl}}$	1		$\gamma_{\text{SiSiCl}}^{\text{Cl}}$	1.0
				$a_{\text{SiSiCl}}^{\text{Cl}}$	1.8		$a_{\text{SiSiCl}}^{\text{Cl}}$	1.8
				α_{SiSiCl}	1		α_{SiSiCl}	0
h_{ClSiCl}	*		h_{ClClCl}	**				

$$* \quad h_{\text{ClSiCl}}(r_1, r_2, \theta) = 30 \left[(\cos\theta - \cos 103^\circ)^2 - 0.5 \right] \exp \left[(r_1 - 1.8)^{-1} + (r_2 - 1.8)^{-1} \right]$$

$$** \quad h_{\text{ClClCl}}(r_1, r_2, \theta) = 3(r_1 r_2)^{-2.056} \exp \left[\frac{0.5795}{r_1 - 2.0862} + \frac{0.5795}{r_2 - 2.0862} \right] + 23.778(2 - \cos^2\theta) \exp \left[\frac{1.7386}{r_1 - 1.6226} + \frac{1.7386}{r_2 - 1.6226} \right]$$

for $i = \text{Cl}$, and $g_i(w_i) = 1$ for $i = \text{Si}$, where $s(x)$ is a smoothing function,

$$s(x) = \frac{1}{1 + \exp[-10(x - 2.5)]}, \quad (\text{B.11})$$

and $w_i = \sum_j b_{ij}$ is the bonding number. The degree of bond formation, b_{ij} , is evaluated by $b_{ij} = u_{ij}/u_{ij}^{\min}$ for $\bar{r}_{ij} > \bar{r}_{ij}^{\min}$ and $b_{ij} = 1$ for $\bar{r}_{ij} < \bar{r}_{ij}^{\min}$, where u_{ij}^{\min} is the minimum value of the function u_{ij} at $\bar{r}_{ij} = \bar{r}_{ij}^{\min}$.

B.2 Molecular Dynamics Modeling of Cl_2 Plasma Etching of Silicon

Figure B.1(a) shows a schematic of the classical MD simulation for plasma etching. Substrate or target Si atoms are placed in the simulation cell, initially having a structure of a diamond lattice whose top surface corresponds to the Si(100) plane. The Si(100) surface concerned is a square of 32.58 \AA on one side (with an area of 1061 \AA^2), where a monolayer (ML) contains 72 Si atoms (or $6.78 \times 10^{14} \text{ atoms/cm}^2$). The simulation cell initially contains target atoms of 20 ML (or 1440 Si atoms) in a depth of 26.0 \AA . Target atoms in the bottom layer are fixed during the simulation, while periodic boundaries are imposed in the horizontal direction. Energetic Cl_x^+ ($x = 1, 2$) and SiCl_x^+ ($x = 0-4$) ions are injected toward the surface from randomly selected horizontal locations above the target at incident angle in the range $\theta_i = 0^\circ-90^\circ$ with translational energies in the range $E_i = 20-500 \text{ eV}$, where $\theta_i = 0^\circ$ corresponds to the normal incidence. In the case of molecular ions, the initial translational energy of ions is taken to be distributed to atoms constituting the ions, based on the respective atomic masses ($m_{\text{Si}} = 28.0855 \text{ g/mol}$, $m_{\text{Cl}} = 35.453 \text{ g/mol}$); moreover, the bond length and angle in molecular ions injected are assumed to be fixed at stable equilibrium, and the molecular orientation is given randomly in space about its center of mass. It is further noted that while energetic species are often referred to as ‘‘ions’’, they are assumed to be neutralized owing to the Auger process just before impact, and then interact with the surface as neutrals.^[225]

To simulate plasma etching environments with simultaneous exposure of energetic ions and neutral reactants, low-energy Cl atoms are supplied normally ($\theta_n = 0^\circ$) onto the surface also from random horizontal locations above the target prior to every ion impact. The number of neutrals supplied per ion impact corresponds to the incoming neutral-to-ion flux ratio in plasma environments, which is taken to be in the range $\Gamma_n^0/\Gamma_i^0 = 0-100$; in practice, $\Gamma_n^0/\Gamma_i^0 = 0$ simulates the etching by energetic ions only, and $\Gamma_n^0/\Gamma_i^0 = 100$ the etching by typical

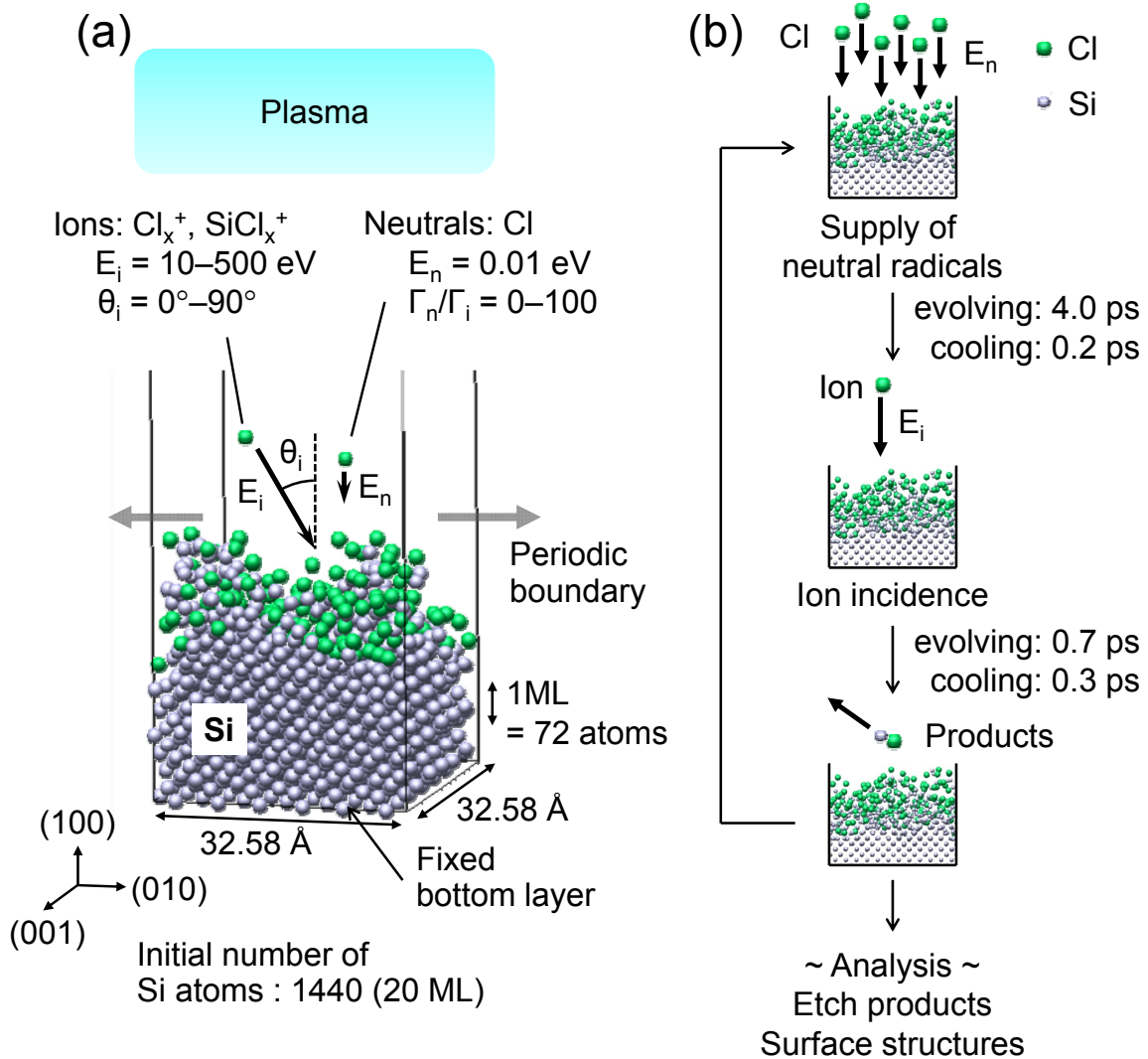


Fig. B.1. (a) Schematic and (b) calculation scheme of the classical MD simulation for plasma etching with exposure of energetic ions and low-energy neutrals, where every after injection of an energetic ion, a set of neutrals are supplied onto the surface. The ions of interest are Cl_x⁺ ($x = 1, 2$) and SiCl_x⁺ ($x = 0\text{--}4$) with translational energies in the range $E_i = 20\text{--}500\text{ eV}$, being incident on Si(100) surfaces at incident angles in the range $\theta_i = 0^\circ\text{--}90^\circ$; Cl neutrals of translational energy $E_n = 0.01\text{ eV}$ are also incident normally thereon with the neutral-to-ion flux ratio in the range $\Gamma_n^0/\Gamma_i^0 = 0\text{--}100$. Substrate or target Si atoms are placed in the simulation cell, which has a square of 32.58 Å on one side and contains target atoms of 20 ML or 1440 Si atoms in a depth of 26.0 Å. Note that an ML contains 72 Si atoms ($= 6.78 \times 10^{14}\text{ atoms/cm}^2$).

high-density plasmas such as ICP^[88] and ECR plasmas.^[132,133,206,207] The translational energy of neutrals is taken to be typically $E_n = 0.01\text{ eV}$, which would be low enough not to etch Si but to stick on the surface.

Figure B.1(b) shows a calculation scheme of the MD simulation for plasma etching, which is in a sense similar to the so-called digital or atomic layer etching of Si consisting of a repetition of Ar^+ ion incidence followed by that of neutral reactants.^[212–214] After every injection of an energetic ion (Cl_x^+ , SiCl_x^+), we let the system evolve for 0.7 ps with the total energy being constant, and then artificially cool the system for 0.3 ps down to the initial temperature (300 K) of target atoms, where the temperature is taken to be the mean kinetic energy over the target atoms contained in the simulation cell. The artificial cooling of the system is made by employing the Berendsen heat removal scheme^[242] with a coupling constant of $2.0 \times 10^{14} \text{ s}^{-1}$.^[243–245] Similarly, after every introduction of a set of low-energy neutrals (Cl), we let the system evolve for 4.0 ps and then cool it for 0.2 ps. In addition, we sometimes add a layer of Si atoms at the bottom of the simulation cell, to maintain the number of target atoms above ~ 20 ML therein during etching. The etch fundamentals, such as etch yield and threshold, product stoichiometry, desorption yield of adsorbates, velocity (energy and angular) distribution of products and adsorbates desorbed, and microscopic structures of surface reaction layers (thickness, coverage, stoichiometry, and depth profile), are analyzed after every ion impact, which are averaged over 1000 ion impacts after the etching characteristics and surface structures have become statistically stable, unless otherwise stated.

It should be noted that in high-density plasma etching environments, the ion flux onto substrate surfaces is often $< 10 \text{ mA/cm}^2$ (or $\Gamma_i^0 < 6.2 \times 10^{16} \text{ cm}^{-2}\text{s}^{-1}$),^[88,132,133,206,207] in which energetic ions impact the surface presently concerned at most approximately once every 10^{-4} s , and so individual ion impacts may be virtually assumed to be temporally isolated events. On the other hand, the MD simulations are limited to times of the order of 10^{-12} s , and so longer time-scale events such as thermal diffusion, reaction, and desorption (that are undoubtedly occurring in surface layers after ion impact) are not likely to occur intrinsically during relatively short times of the simulation. We took the simulation time of 1 ps (evolving and cooling times of 0.7 and 0.3 ps, respectively, as mentioned above), based on the transit time for a “shock wave” to traverse the distance from the top surface to the fixed bottom layer of the simulation cell and back,^[243–245] which is slightly less than that of 1–2 ps generally taken in other MD studies.^[237] No significant change was confirmed in the etching characteristics and surface structures obtained for varying the evolving and cooling times in the range 0.7–2.8 and 0.3–2.1 ps, respectively (or the simulation time in the range 1–5 ps).

When MD simulations of atomic collision cascade are carried out, the time step integration

B.2 Molecular Dynamics Modeling of Cl₂ Plasma Etching of Silicon

algorithm of the Newton's equation of motion [eq. (B.3)] is important for the stability, accuracy, and computational time. In this study, the Smith's "Two step A algorithm" is used for the accuracy and computational time.^[246,247]

Appendix C

Particle-in-Cell Simulation

Particle-in-Cell (PIC) is a simulation method of partially ionized gases,^[197,248,249] where interaction between electromagnetic fields and charged particles are solved using spatial meshes. In addition, particle collisions are taken into account with Monte Carlo methods. In this appendix, the application for calculation of ion trajectories concerned with experiments using a sheath control plate is described.

C.1 Calculation of Ion Trajectories

Figure C.1(a) shows a schematic of the simulation domain, including the plasma region and a sheath control plate on the wafer stage. The height of simulation area is 15 mm (distance between bottom of plasma region and top of wafer stage), and the width is variable depending on the geometry of the sheath control plate (slit width in the range $w_s = 3\text{--}7$ mm, silt height of $h_s = 4$ mm, blade thickness of $t_s = 1$ mm, and slit angles of $\theta_s = 45^\circ$ and 90°), where periodic boundaries are imposed in the horizontal direction. The Cartesian coordinates (x – z) are employed, in which a number of simulated particles are loaded along with three velocity

$$\nabla^2 \phi = -\frac{\rho}{\varepsilon_0} = -\frac{e}{\varepsilon_0}(n_i - n_e) \quad (\text{C.3})$$

is solved by Broyden's second method,^[250] where ϕ is electrostatic potential, ρ charge density, ε_0 permittivity in vacuum, n_i and n_e ion and electron density, respectively. In this calculation, the electron density is assumed to be determined by the Boltzmann relation

$$n_e = n_p \exp\left[\frac{e}{k_B T_e}(\phi - V_p)\right], \quad (\text{C.4})$$

where n_p is plasma density, k_B the Boltzmann constant, T_e electron temperature, and V_p plasma potential.

After the steady-state electrostatic potential distribution is averaged over time, the tracer ions are set at the sheath edge with the Bohm velocity

$$\mathbf{u}_B = \left(\frac{k_B T_e}{m_i}\right)^{1/2} \cdot \frac{\mathbf{E}}{|\mathbf{E}|}, \quad (\text{C.5})$$

and the ion trajectories (or ion incident energy and angle) onto the surfaces of the sheath control plate and wafer stage are calculated.

References

- [1] S. M. Sze and K. K. Ng: *Physics of Semiconductor Devices*, 3rd ed., (Wiley, Hoboken, NJ, 2007).
- [2] *ULSI Technology*, edited by C. Y. Chang and S. M. Sze, (McGraw-Hill, New York, 1996).
- [3] H. Abe, M. Yoneda, and H. Fujiwara: *Jpn. J. Appl. Phys.* **47**, 1435 (2008).
- [4] J. S. Kilby: U.S. Patent 3138743, Jun. 23, 1964.
- [5] R. N. Noyce: U.S. Patent 2981877, Apr. 25, 1961.
- [6] G. E. Moore: *Electronics* **38**, 114 (1965).
- [7] G. E. Moore: *IEDM Tech. Dig.* **21**, 11 (1975).
- [8] “International Technology Roadmap for Semiconductors (ITRS) 2013 edition”
<http://www.itrs.net/>
- [9] R. H. Dennard, F. H. Gaensslen, V. L. Rideout, W. Bassous, and A. R. LeBlanc: *IEEE J. Solid-State Circuits* **SC-9**, 256 (1974).
- [10] C. T. Sah: *Proc. IEEE* **76**, 1280 (1988).
- [11] D. Hisamoto, W.-C. Lee, J. Kedzierski, H. Takeuchi, K. Asano, C. Kuo, E. Anderson, T.-J. King, J. Bokor, and C. Hu: *IEEE Trans. Electron Devices* **47**, 2320 (2000).
- [12] X. Huang, W.-C. Lee, C. Kuo, D. Hisamoto, L. Chang, J. Kedzierski, E. Anderson, H. Takeuchi, Y.-K. Choi, K. Asano, V. Subramanian, T.-J. King, J. Bokor, and C. Hu: *IEEE Trans. Electron Devices* **48**, 880 (2001).
- [13] B. S. Doyle, S. Datta, M. Doczy, S. Harelend, B. Jin, J. Kavalieros, T. Linton, A. Murthy, R. Rios, and R. Chau: *IEEE Electron Device Lett.* **24**, 263 (2003).
- [14] I. Ferain, C. A. Colinge, and J.-P. Colinge: *Nature* **479**, 310 (2011).

References

- [15] K. J. Kanarik, G. Kamarthy, and R. A. Gottscho: *Solid State Technol.* **55**(3), 15 (2012).
- [16] M. A. Lieberman and A. J. Lichtenberg: *Principles of Plasma Discharges and Materials Processing*, 2nd ed. (Wiley, Hoboken, NJ, 2005).
- [17] V. M. Donnelly and A. Kornblit: *J. Vac. Sci. Technol. A* **31**, 050825 (2013).
- [18] B. Wu, A. Kumar, and S. Pamarthy: *J. Appl. Phys.* **108**, 051101 (2010).
- [19] F. F. Chen: *Introduction to plasma physics and controlled fusion*, 2nd ed. Vol. 1 Plasma physics (Springer, NY, 2006).
- [20] H. Nakata, K. Nishioka, and H. Abe: *J. Vac. Sci. Technol.* **17**, 1351 (1980).
- [21] T. Kitagawa, K. Nakamura, K. Osari, K. Takahashi, K. Ono, M. Oosawa, S. Hasaka, and M. Inoue: *Jpn. J. Appl. Phys.* **45**, L297 (2006).
- [22] K. B. Jung, H. Cho, Y. B. Hahn, E. S. Lambers, S. Onishi, D. Johnson, A. T. Hurst Jr., J. R. Childress, Y. D. Park, and S. J. Pearton: *J. Appl. Phys.* **85**, 4788 (1999).
- [23] J. E. Stevens: "Electron cyclotron resonance plasma sources" in *High Density Plasma Source, Design, Physics and Performance*, edited by O. A. Ppov (Noyes Publications, Park Ridge, NJ, 1995), pp. 312–379.
- [24] H. Sugai, I. Ghanashev, and M. Nagatsu: *Plasma Source Sci. Technol.* **7**, 192 (1998).
- [25] F. F. Chen: "Helicon plasma sources" in *High Density Plasma Source, Design, Physics and Performance*, edited by O. A. Ppov (Noyes Publications, Park Ridge, NJ, 1995), pp. 1–75.
- [26] J. C. Forster and J. H. Keller: "Planar inductive sources" in *High Density Plasma Source, Design, Physics and Performance*, edited by O. A. Ppov (Noyes Publications, Park Ridge, NJ, 1995), pp. 76–99.
- [27] Y. H. Lee, G. S. Oehrlein, and C. Ransom: *Rad. Eff. Defects Solids* **111-112**, 221 (1989).
- [28] P. Verdonck, C. M. Hasenak, and R. D. Mansano: *J. Vac. Sci. Technol. B* **14**, 538 (1996).
- [29] J. Hopwood, C. R. Guarnieri, S. J. Whitehair, and J. J. Cuomo: *J. Vac. Sci. Technol. A* **11**, 152 (1993).
- [30] J. H. Keller, J. C. Foster, and M. S. Barnes: *J. Vac. Sci. Technol. A* **11**, 2487 (1993).
- [31] I. M. El-Fayoumi, I. R. Jones, and M. M. Turner: *J. Phys. D: Appl. Phys.* **31**, 3082 (1998).
- [32] S.-H. Seo, J.-I. Hong, K.-H. Bai, and H.-Y. Chang: *Phys. Plasmas* **6**, 614 (1999).
- [33] A. M. Daltrini, S. A. Moshkalev, M. J. R. Monteiro, E. Bessler, A. Kostyukov, and M. Machida: *J. Appl. Phys.* **101**, 073309 (2007).
- [34] E. A. Ogryzlo, D. E. Ibbotson, D. L. Flamm, and J. A. Mucha: *J. Appl. Phys.* **67**, 3115 (1990).
- [35] P. Sigmund: *Phys. Rev.* **184**, 383 (1969).
- [36] H. F. Winters and J. W. Coburn: *Surf. Sci. Rep.* **14**, 162 (1992).
- [37] J. W. Coburn and H. F. Winters: *J. Appl. Phys.* **50**, 3189 (1979).
- [38] P. Pan and L. Liu: *J. Vac. Sci. Technol. B* **15**, 1752 (1997).

-
- [39] E. Pargon, M. Darnon, O. Joubert, T. Chevolleau, L. Vallier, L. Mollard, and T. Lill: *J. Vac. Sci. Technol. B* **23**, 1913 (2005).
- [40] K. Eriguchi and K. Ono: *J. Phys. D: Appl. Phys.* **41**, 024002 (2008).
- [41] K. Eriguchi and Y. Kosaka: *IEEE Trans. Electron Devices* **45**, 160 (1998).
- [42] T. Yunogami, T. Mizutani, K. Suzuki, and S. Nishimatsu: *Jpn. J. Appl. Phys. Part 1* **28**, 2172 (1989).
- [43] L. Desvoivres, L. Vallier, and O. Joubert: *J. Vac. Sci. Technol. B* **18**, 156 (2000).
- [44] S. A. Vitale and B. A. Smith: *J. Vac. Sci. Technol. B* **21**, 2205 (2003).
- [45] M. Fukasawa, Y. Nakakubo, A. Matsuda, Y. Takao, K. Eriguchi, K. Ono, M. Minami, F. Uesawa, and T. Tasumi: *J. Vac. Sci. Technol. A* **29**, 041301 (2011).
- [46] K. Eriguchi, A. Matsuda, Y. Nakakubo, M. Kamei, H. Ohta, and K. Ono: *IEEE Electron Device Lett.* **30**, 712 (2009).
- [47] Y. Nakakubo, A. Matsuda, M. Kamei, H. Ohta, K. Eriguchi, and K. Ono: in *Emerging Technologies and Circuits*, 2021, A. Amara, T. Ea, and M. Belleville, Eds., Springer, pp. 107-120 (2010).
- [48] K. Eriguchi, U. Nakakubo, A. Matsuda, Y. Takao, and K. Ono: *IEEE Electron Device Lett.* **30**, 1275 (2009).
- [49] D. J. Thomas, P. Southworth, M. C. Flowers, and R. Greef: *J. Vac. Sci. Technol. B* **7**, 1325 (1989).
- [50] R. Pétri, P. Brault, O. Vatel, D. Henry, E. André, P. Dumas, and F. Salvan: *J. Appl. Phys.* **75**, 7498 (1994).
- [51] H. Feil, J. Dieleman, B. J. Garrison: *J. Appl. Phys.* **74**, 1303 (1993).
- [52] K.-T. Sung and S. W. Pang: *Jpn. J. Appl. Phys. Part 1* **33**, 7112 (1994).
- [53] M. J. M. Vugts, M. F. A. Eurlings, L. J. F. Hermans, and H. C. W. Beijerinck: *J. Vac. Sci. Technol. A* **14**, 2780 (1996).
- [54] P. Brault, P. Dumas, and F. Salvan: *J. Phys. Condens. Matter* **10**, L27 (1998).
- [55] Y.-P. Zhao, J. T. Drotar, G.-C. Wang, and T.-M. Lu: *Phys. Rev. Lett.* **82**, 4882 (1999).
- [56] J. T. Drotar, Y.-P. Zhao, T.-M. Lu, and G.-C. Wang: *Phys. Rev. B* **61**, 3012 (2000).
- [57] J. T. Drotar, Y.-P. Zhao, T.-M. Lu, and G.-C. Wang: *Phys. Rev. B* **62**, 2118 (2000).
- [58] E. Gogolides, C. Boukouras, G. Kokkoris, O. Brani, A. Tserepi, V. Constantoudis: *Microelectron. Eng.* **73-74**, 312 (2004).
- [59] A. A. E. Stevens and H. C. W. Beijerinck: *J. Vac. Sci. Technol. A* **23**, 126 (2005).
- [60] E. Zakka, V. Constantoudis, and E. Gogolides: *IEEE Trans. Plasma Sci.* **35**, 1359 (2007).
- [61] G. kokkoris, V. Constantoudis, P. Angelikopoulos, G. Boulousis, and E. Gogolides: *Phys. Rev. B* **76**, 193405 (2007).
- [62] Y. Yin and H. H. Sawin: *J. Vac. Sci. Technol. A* **26**, 151 (2008).
- [63] W. S. Hwang, B.-J. Cho, D. S. H. Chan, S. W. Lee, and W. J. Yoo: *J. Electrochem. Soc.* **155**, H6 (2008).

References

- [64] M. Martin and G. Cunge: *J. Vac. Sci. Technol. B* **26**, 1281 (2008).
- [65] W. Guo and H. H. Sawin: *J. Phys. D: Appl. Phys.* **42**, 194014 (2009).
- [66] J. J. Végh and D. B. Graves: *Plasma Sources Sci. Technol.* **19**, 045005 (2010).
- [67] E. Gogolides, V. Constantoudis, G. Kokkoris, D. Kontziampasis, K. Tsougeni, G. Boulousis, M. Vlachopoulou, and A. Tserepi: *J. Phys. D: Appl. Phys.* **44**, 170421 (2011).
- [68] Y. Yin and H. H. Sawin: *J. Vac. Sci. Technol. A* **25**, 802 (2007).
- [69] W. Guo and H. H. Sawin: *J. Vac. Sci. Technol. A* **28**, 259 (2010).
- [70] X. Hua, S. Engelmann, G. S. Oehrlein, P. Jiang, P. Lazzeri, E. Iacob, and M. Anderle: *J. Vac. Sci. Technol. B* **24**, 1850 (2006).
- [71] A. R. Pal, R. L. Bruce, F. Weirnboeck, S. Engelmann, T. Lin, M.-S. Kuo, R. Phaneuf, and G. S. Oehrlein: *J. Appl. Phys.* **105**, 013311 (2009).
- [72] G. S. Oehrlein, R. J. Phaneuf, and D. B. Graves: *J. Vac. Sci. Technol. B* **29**, 010801 (2011).
- [73] R. L. Bruce, F. Weirnboeck, T. Lin, R. J. Phaneuf, G. S. Oehrlein, B. K. Long, C. G. Willson, J. J. Végh, D. Nest, and D. B. Graves: *J. Appl. Phys.* **107**, 084310 (2010).
- [74] T.-C. Lin, R. L. Bruce, G. S. Oehrlein, R. J. Phaneuf, and H.-C. Kan: *Appl. Phys. Lett.* **100**, 233113 (2012).
- [75] Y. Yin, S. Rasgon, and H. H. Sawin: *J. Vac. Sci. Technol. B* **24**, 2360 (2006).
- [76] J. Thiault, J. Foucher, J. H. Tortai, O. Joubert, S. Landis, and S. Pauliac: *J. Vac. Sci. Technol. B* **23**, 3075 (2005).
- [77] E. Gogolides, V. Constantoudis, G. P. Patsis, and A. Tserepi: *Microelectron. Eng.* **83**, 1067 (2006).
- [78] K. Patel, T.-J. King Liu, and C. J. Spanos: *IEEE Trans. Electron Devices* **56**, 3055 (2009).
- [79] X. Sun and T.-J. King Liu: *IEEE Trans. Semicond. Manuf.* **23**, 311 (2010).
- [80] E. Altamirano-Sánchez, V. Paraschiv, M. Demand, and W. Boullart: *Microelectron. Eng.* **88**, 2871 (2011).
- [81] K. Eriguchi, Y. Takao, and K. Ono: *J. Vac. Sci. Technol. A* **29**, 041303 (2011).
- [82] K. S. Chen, A. Ayon, and S. M. Spearing: *J. Am. Ceram. Soc.* **83**, 1476 (2000).
- [83] N. Tayebi and A. A. Polycarpou: *J. Appl. Phys.* **98**, 073528 (2005).
- [84] H. Tsuda, M. Mori, Y. Takao, K. Eriguchi, and K. Ono: *Jpn. J. Appl. Phys.* **49**, 08JE01 (2010).
- [85] H. Tsuda, M. Mori, Y. Takao, K. Eriguchi, and K. Ono: *Thin Solid Films* **518**, 3475 (2010).
- [86] H. Tsuda, H. Miyata, Y. Takao, K. Eriguchi, and K. Ono: *Jpn. J. Appl. Phys.* **50**, 08JE06 (2011).
- [87] H. Tsuda, Y. Takao, K. Eriguchi, and K. Ono: *Jpn. J. Appl. Phys.* **51**, 08HC01 (2012).
- [88] H. Tsuda, N. Nakazaki, Y. Takao, K. Eriguchi, and K. Ono: *J. Vac. Sci. Technol. B* **32**,

- 031212 (2014).
- [89] T. Hatsuse, N. Nakazaki, H. Tsuda, Y. Takao, K. Eriguchi, and K. Ono: *Jpn. J. Appl. Phys.* (unpublished).
- [90] A. Iwakawa, H. Ohta, K. Eriguchi, and K. Ono: *Jpn. J. Appl. Phys.* **47**, 6464 (2008).
- [91] H. Ohta, A. Iwakawa, K. Eriguchi, and K. Ono: *J. Appl. Phys.* **104**, 073302 (2008).
- [92] A. Iwakawa, T. Nagaoka, H. Ohta, K. Eriguchi, and K. Ono: *Jpn. J. Appl. Phys.* **47**, 8560 (2008).
- [93] T. Nagaoka, K. Eriguchi, K. Ono, and H. Ohta: *J. Appl. Phys.* **105**, 023302 (2009).
- [94] H. Ohta, T. Nagaoka, K. Eriguchi, and K. Ono: *Jpn. J. Appl. Phys.* **48**, 020225 (2009).
- [95] T. Nagaoka, H. Ohta, K. Eriguchi, and K. Ono: *Jpn. J. Appl. Phys.* **48**, 070219 (2009).
- [96] N. Nakazaki, Y. Takao, K. Eriguchi, and K. Ono: *Jpn. J. Appl. Phys.* **53**, 056201 (2014).
- [97] N. Nakazaki, Y. Takao, K. Eriguchi, and K. Ono: *J. Appl. Phys.* **118**, 233304 (2015).
- [98] N. Nakazaki, Y. Takao, K. Eriguchi, and K. Ono: *Jpn. J. Appl. Phys.* (unpublished).
- [99] J. W. Coburn and M. Chen: *J. Appl. Phys.* **51**, 3134 (1980).
- [100] R. d'Agostino, F. Cramarossa, S. D. Benedictis, and G. Ferraro: *J. Appl. Phys.* **52**, 1259 (1981).
- [101] V. M. Donnelly, D. L. Flamm, W. C. Dautremont-Smith, and D. J. Werder: *J. Appl. Phys.* **55**, 242 (1984).
- [102] R. d'Agostino, F. Cramarossa, S. D. Benedictis, F. Fracassi, L. Laska, and K. Masak: *Plasma Chem. Plasma Process.* **5**, 239 (1985).
- [103] M. J. Schabel, V. M. Donnelly, A. Kornblit, and W. W. Tai: *J. Vac. Sci. Technol. A* **20**, 555 (2002).
- [104] E. Karakas, V. M. Donnelly, and D. J. Economou: *Appl. Phys. Lett.* **102**, 034107 (2013).
- [105] J. P. Booth, O. Joubert, J. Pelletier, and N. Sadeghi: *J. Appl. Phys.* **69**, 618 (1991).
- [106] R. E. Walkup, K. L. Saenger, and G. S. Selwyn: *J. Chem. Phys.* **84**, 2668 (1986).
- [107] M. V. Malyshev and V. M. Donnelly: *J. Appl. Phys.* **87**, 1642 (2000).
- [108] N. C. M. Fuller, I. P. Herman, and V. M. Donnelly: *J. Appl. Phys.* **90**, 3182 (2001).
- [109] A. R. Striganov and N. S. Sventitskii: *Tables of Spectral Lines of Neutral and ionized Atoms*, (IFI/Plenum, New York, 1968).
- [110] R. W. B. Pearse and A. G. Gaydon: *The Identification of Molecular Spectra*, 3rd ed., (Chapman & Hall, London, 1963).
- [111] K. P. Huber and G. Hertzberg: *Molecular Spectra and Molecular Structure: IV. Constants of Diatomic Molecules*, (Van Nostrand Reinhold, New York, 1979).
- [112] S. D. Peterimhoff and R. J. Buenker: *Chem. Phys.* **57**, 279 (1981).
- [113] J. Tellinghuisen and D. K. Chakraborty: *Chem. Phys. Lett.* **134**, 565 (1987).
- [114] P. C. Tellinghuisen, B. Guo, D. K. Chakraborty, and J. Tellinghuisen: *J. Mol. Spectrosc.* **128**, 268 (1988).
- [115] V. M. Donnelly: *J. Vac. Sci. Technol. A* **14**, 1076 (1996).

References

- [116] F. P. Huberman: *J. Mol. Spectrosc.* **20**, 29 (1966).
- [117] R. P. Tuckett and S. D. Peyerimhoff: *Chem. Phys.* **83**, 203 (1984).
- [118] J. C. Choi and J. L. Hardwick: *J. Mol. Spectrosc.* **137**, 138 (1989).
- [119] H. Bredohl, Ph Demoulin, Y. Houbrechts, and F. Melen: *J. Phys. B* **14**, 1771 (1981).
- [120] B. P. Ruzsicska, A. Jodhan, I. Safarik, and O. P. Strausz: *Chem. Phys. Lett.* **113**, 67 (1985).
- [121] N. Washida, Y. Matsumi, T. Hayashi, T. Ibuki, A. Hiraya, and K. Shobatake: *J. Chem. Phys.* **83**, 2769 (1985).
- [122] D. Sameith, J. P. Monch, H.-J. Tiller and K. Schade: *Chem. Phys. Lett.* **128**, 483 (1986).
- [123] M. Suzuki, N. Washida, and G. Inoue: *Chem. Phys. Lett.* **131**, 24 (1986).
- [124] M. D. Rowe: *J. Chem. Soc., Faraday Trans. 2* **84**, 191 (1988).
- [125] K. H. A. Bogart and V. M. Donnelly: *J. Appl. Phys.* **86**, 1822 (1999).
- [126] J. Y. Choe, N. C. M. Fuller, V. M. Donnelly, and I. P. Herman: *J. Vac. Sci. Technol. A* **18**, 2669 (2000).
- [127] P. Ho and W. G. Breiland: *Appl. Phys. Lett.* **44**, 51 (1984).
- [128] H. Singh, J. W. Coburn, and D. B. Graves: *J. Vac. Sci. Technol. A* **17**, 2447 (1999).
- [129] H. Singh, J. W. Coburn, and D. B. Graves: *J. Vac. Sci. Technol. A* **18**, 299 (2000).
- [130] J. Benedikt, A. Hecimovic, D. Ellerweg, and A. v. Keudell: *J. Phys. D: Appl. Phys.* **45**, 403001 (2012).
- [131] H. M. Mott-Smith and I. Langmuir: *Phys. Rev.* **28**, 727 (1926).
- [132] K. Ono, M. Tuda, K. Nishikawa, T. Oomori, and K. Namba: *Jpn. J. Appl. Phys.* **33**, 4424 (1994).
- [133] K. Nishikawa, T. Oomori, and K. Ono: *J. Vac. Sci. Technol. B* **17**, 127 (1999).
- [134] K. Nakamoto: *Infrared and Raman Spectra of Inorganic and Coordination Compounds: Part A: Theory and Applications in Inorganic Chemistry*, 5th ed., (Wiley, New York, 1997), Sec. II. p. 160 and p. 193.
- [135] J. M. Campbell, D. Klapstein, M. Dulick, and P. F. Bernath: *Astrophys. J. Suppl. Ser.* **101**, 237 (1995).
- [136] J. K. Lawson, D. M. Aikens, R. E. English, Jr., and C. R. Wolfe: *Proc. SPIE* **2775**, 345 (1996).
- [137] A. Duparré, J. Ferre-Borrull, S. Gliech, G. Notni, J. Steinert, and J. M. Bennett: *Appl. Opt.* **41**, 154 (2002).
- [138] V. V. Yashchuk, A. D. Franck, S. C. Irick, M. R. Howells, A. A. MacDowell, and W. R. McKinney: *Proc. SPIE* **5858**, 58580A (2005).
- [139] M. Senthilkumar, N. K. Sahoo, S. Thakur, and R. B. Tokas: *Appl. Surf. Sci.* **252**, 1608 (2005).
- [140] K. Tsujimoto, T. Kumihashi, and S. Tachi: *Appl. Phys. Lett.* **63**, 1915 (1993).
- [141] C. Steinbrüchel: *Appl. Phys. Lett.* **55**, 1960 (1989).

-
- [142] M. Balooch, M. Moalem, W.-E. Wang, and A. V. Hamza: *J. Vac. Sci. Technol. A* **14**, 229 (1996).
- [143] J. P. Chang and H. H. Sawin: *J. Vac. Sci. Technol. B* **19**, 1319 (2001).
- [144] L. Sha and J. P. Chang: *J. Vac. Sci. Technol. A* **22**, 88 (2004).
- [145] S. A. Vitale, H. Chae, and H. H. Sawin: *J. Vac. Sci. Technol. A* **19**, 2197 (2001).
- [146] W. Jin, S. A. Vitale, and H. H. Sawin: *J. Vac. Sci. Technol. A* **20**, 2106 (2002).
- [147] N. Nakazaki, H. Tsuda, Y. Takao, K. Eriguchi, and K. Ono: *Appl. Phys. Express* (unpublished).
- [148] A. E. Lita and J. E. Sanchez, Jr.: *J. Appl. Phys.* **85**, 876 (1999).
- [149] D. B. Fenner: *J. Appl. Phys.* **95**, 5408 (2004).
- [150] D. Raoufi: *Physica B* **405**, 451 (2010).
- [151] M. Nie, T. Meta, and K. Ellmer: *J. Appl. Phys.* **115**, 154905 (2014).
- [152] T. Tsuchizawa, C. Takahashi, and S. Matsuo: *Jpn. J. Appl. Phys. Part I* **33**, 6019 (1994).
- [153] I. P. Herman: *Optical Diagnostics for Thin Film Processing*, (Academic, New York, 1996), Chap. 6, p. 175.
- [154] V. M. Donnelly: *J. Appl. Phys.* **79**, 9353 (1996).
- [155] G. Cunge, N. Sadeghi, and R. Ramos: *J. Appl. Phys.* **102**, 093305 (2007).
- [156] S. Tinck, W. Boullart, and A. Bogaerts: *Plasma Source Sci. Technol.* **20**, 045012 (2011).
- [157] G. Cunge, R. L. Inglebert, O. Joubert, L. Vallier, and N. Sadeghi: *J. Vac. Sci. Technol. B* **20**, 2137 (2002).
- [158] G. Cunge, M. Kogelschatz, and N. Sadeghi: *J. Appl. Phys.* **96**, 4578 (2004).
- [159] G. Cunge, D. Vempaire, R. Ramos, M. Touzeau, O. Joubert, P. Bodard, and N. Sadeghi: *Plasma Source Sci. Technol.* **19**, 034017 (2010).
- [160] C. Lee, D. B. Graves, and M. A. Lieberman: *Plasma Chem. Plasma Process.* **16**, 99 (1996).
- [161] M. W. Kiehlbauch and D. B. Graves: *J. Vac. Sci. Technol. A* **21**, 116 (2003).
- [162] A. Agarwal and M. J. Kushner: *J. Vac. Sci. Technol. A* **26**, 498 (2008).
- [163] H. Singh, J. W. Coburn, and D. B. Graves: *J. Vac. Sci. Technol. A* **19**, 718 (2001).
- [164] A. W. Kofschoten, R. A. Haring, A. Haring, and A. E. de Vries: *J. Appl. Phys.* **55**, 3813 (1984).
- [165] D. J. Oostra, A. Haring, R. P. van Ingen, and A. E. de Vries: *J. Appl. Phys.* **64**, 315 (1988).
- [166] J. W. Coburn: *J. Vac. Sci. Technol. B* **12**, 1384 (1994).
- [167] R. Basner, M. Gutkin, J. Mahoney, V. Tarnovsky, H. Deutsch, and K. Becker: *J. Chem. Phys.* **123**, 054313 (2005).
- [168] K. Becker, J. Mahoney, M. Gutkin, V. Tarnovsky, and R. Basner: *Jpn. J. Appl. Phys. Part I* **45**, 8188 (2006).
- [169] S. J. King and S. D. Price: *J. Chem. Phys.* **134**, 074311 (2011).

References

- [170] J. Mahoney, V. Tarnovsky, and K. H. Becker: *Eur. Phys. J. D* **46**, 289 (2008).
- [171] M. Gutkin, J. M. Mahoney, V. Tarnovsky, H. Deutsch, and K. Becker: *Int. J. Mass Spectrom.* **280**, 101 (2009).
- [172] P. Calandra, C. S. S. O'Connor, and S. D. Price: *J. Chem. Phys.* **112**, 10821 (2000).
- [173] S. Pal, P. Bhatt, and J. Kumar: *Int. J. Mass Spectrom.* **229**, 151 (2003).
- [174] P. Mozejko, G. Kasperski, Cz. Szmytkowski, A. Zecca, G. P. Karwasz, L. Del Longo, and R. S. Brusa: *Eur. Phys. J. D* **6**, 481 (1999).
- [175] H. N. Kothari, S. H. Pandya, and K. N. Joshipura: *J. Phys. B* **44**, 125202 (2011).
- [176] F. A. Stevie and M. J. Vasile: *J. Chem. Phys.* **74**, 5106 (1981).
- [177] M. V. Kurepa and D. S. Belić: *J. Phys. B* **11**, 3719 (1978).
- [178] L. G. Christophorou and J. K. Olthoff: *J. Phys. Chem. Ref. Data* **28**, 131 (1999).
- [179] T. Ito, K. Karahasi, S.-Y. Kang, and S. Hamaguchi: *J. Vac. Sci. Technol. A* **31**, 031301 (2013).
- [180] T. Sakai, A. Sakai, and H. Okano: *Jpn. J. Appl. Phys. Part 1* **32**, 3089 (1993).
- [181] K. Boussu, B. Van der Bruggen, A. Volodin, J. Snauwaert, C. Van Haesendonck, and C. Vandecasteele: *J. Colloids Interface Sci.* **286**, 632 (2005).
- [182] W. Guo, B. Bai, and H. H. Sawin: *J. Vac. Sci. Technol. A* **27**, 388 (2009).
- [183] W. L. Chan and E. Chason: *J. Appl. Phys.* **101**, 121301 (2007).
- [184] C. Carter, B. Navinsek, and J. L. Whitton: "Heavy ion sputtering induced surface topography development" in *Sputtering by Particle Bombardment II. Sputtering of Alloys and Compound, Electron and Neutron Sputtering, Surface Topography*, edited by R. Behrisch, (Springer, Berlin, 1983), Chap. 3, pp. 231–269.
- [185] R. M. Bradley and J. M. E. Harper: *J. Vac. Sci. Technol. A* **6**, 2390 (1988).
- [186] R. Cuerno, H. A. Makse, S. Tomassone, S. T. Harrington, and H. E. Stanley: *Phys. Rev. Lett.* **75**, 4464 (1995).
- [187] M. A. Makeev and A.-L. Barabási: *Appl. Phys. Lett.* **71**, 2800 (1997).
- [188] G. Carter: *J. Appl. Phys.* **85**, 455 (1999).
- [189] M. A. Makeev, R. Cuerno, A.-L. Barabási: *Nucl. Instrum. Methods B* **197**, 185 (2002).
- [190] J. Munõz-Garcia, M. Castro, and R. Cuerno: *Phys. Rev. Lett.* **96**, 086101 (2006).
- [191] T. K. Chini, D. P. Datta, and S. R. Bhattacharyya: *J. Phys.: Condens. Matter* **21**, 224004 (2009).
- [192] I. Koponen, M. Hautala, and O.-P. Sievänen: *Phys. Rev. Lett.* **78**, 2612 (1997).
- [193] A.-D. Brown, J. Erlebacher, W.-L. Chan, and E. Chason: *Phys. Rev. Lett.* **95**, 056101 (2005).
- [194] C. C. Cheng, K. V. Guinn, I. P. Herman, and V. M. Donnelly: *J. Vac. Sci. Technol. A* **13**, 1970 (1995).
- [195] J.-H. Lee, G.-Y. Yeon, J.-W. Lee, and J.-Y. Lee: *J. Vac. Sci. Technol. A* **15**, 573 (1997).
- [196] S. Takahashi, K. Suzuki, M. Okano, M. Imada, T. Nakamori, Y. Ota, K. Ishizaki, and S.

- Noda: *Nature Mater.* **8**, 721 (2009).
- [197] Y. Takao, K. Matsuoka, K. Eriguchi, and K. Ono: *Jpn. J. Appl. Phys.* **50**, 08JC02 (2011).
- [198] B. Ziberi, M. Cornejo, F. Frost, and B. Rauschenbach: *J. Phys: Condens. Matter* **21**, 224003 (2009).
- [199] D. P. Hamblen and A. Cho-Lin: *J. Electrochem. Soc.* **135**, 1816 (1988).
- [200] J. P. Chang and H. H. Sawin: *J. Vac. Sci. Technol. A* **15**, 601 (1997).
- [201] T. M. Mayer, R. A. Barker, and L. J. Whitman: *J. Vac. Sci. Technol.* **18**, 349 (1981).
- [202] H. Okano and Y. Horiike: *Jpn. J. Appl. Phys.* **20**, 2429 (1981).
- [203] M. A. Bösch, L. A. Coldren, and E. Good: *Appl. Phys. Lett.* **38**, 264 (1981).
- [204] W. Guo and H. H. Sawin: *J. Vac. Sci. Technol. A* **27**, 1326 (2009).
- [205] N. Nakazaki, Y. Takao, K. Eriguchi, and K. Ono: *J. Appl. Phys.* (unpublished).
- [206] K. Ono, T. Oomori, M. Tuda, and K. Namba: *J. Vac. Sci. Technol. A* **10**, 1071 (1992).
- [207] M. Tuda and K. Ono: *Jpn. J. Appl. Phys.* **36**, 2482 (1997).
- [208] M. Tuda and K. Ono: *Jpn. J. Appl. Phys. Part 2* **35**, L1374 (1996).
- [209] K. Ono and M. Tuda: *Thin Solid Films* **374**, 208 (2000).
- [210] A. Agarwal, S. Rauf, and K. Collins: *Appl. Phys. Lett.* **99**, 021501 (2011).
- [211] C. Petit-Etienne, M. Darnon, P. Bodart, M. Fouchier, G. Cunge, E. Pargon, L. Vallier, O. Joubert, S. Banna: *J. Vac. Sci. Technol. B* **31**, 011201 (2013).
- [212] H. Sakaue, S. Ishida, and K. Asami: *Jpn. J. Appl. Phys.* **29**, 2648 (1990).
- [213] S. D. Athavale and D. J. Econmou: *J. Vac. Sci. Technol. A* **13**, 966 (1995).
- [214] K. J. Kanarik, T. Lill, E. A. Hudson, S. Sriraman, S. Tan, J. Marks, V. Vahedi, and R. A. Gottscho: *J. Vac. Sci. Technol. A* **33**, 020802 (2015).
- [215] S. Noda, H. Nishimori, T. Ida, T. Arikado, K. Ichiki, T. Ozaki, and S. Samukawa: *J. Vac. Sci. Technol. A* **22**, 1506 (2004).
- [216] S. Samukawa: *Jpn. J. Appl. Phys.* **45**, 2395 (2006).
- [217] N. Kuboi, T. Tatsumi, T. Kinoshita, T. Shigetoshi, M. Fukasawa, J. Komachi, and H. Ansai: *J. Vac. Sci. Technol. A* **33**, 061308 (2015).
- [218] Y. Osano and K. Ono: *Jpn. J. Appl. Phys.* **44**, 8650 (2005).
- [219] Y. Osano, M. Mori, N. Itabashi, K. Takahashi, K. Eriguchi, and K. Ono: *Jpn. J. Appl. Phys.* **45**, 8157 (2006).
- [220] Y. Osano and K. Ono: *J. Vac. Sci. Technol. B* **26**, 1425 (2008).
- [221] R. A. Gottscho: *J. Vac. Sci. Technol. B* **11**, 1884 (1993).
- [222] M. Tuda, K. Ono, and K. Nishikawa: *J. Vac. Sci. Technol. B* **14**, 3291 (1996).
- [223] M. Tuda, K. Nishikawa, and K. Ono: *J. Appl. Phys.* **81**, 960 (1997).
- [224] A. P. Mahorowala and H. H. Sawin: *J. Vac. Sci. Technol. B* **20**, 1064 (2002).
- [225] H. D. Hagstun: *Phys. Rev.* **122**, 83 (1961).
- [226] P. Sigmund: "Sputtering by ion bombardment theoretical concepts" in *Sputtering by Particle Bombardment I. Physical Sputtering of Single-Element Solids*, edited by R.

References

- Behrisch, (Springer, Berlin, 1981), Chap. 2, pp. 9–71.
- [227] J. P. Biersack and W. Eckstein: *Appl. Phys. A* **34**, 73 (1984).
- [228] J. F. Ziegler, J. P. Biersack, and U. Littmark: *The Stopping and Range of Ions in Matter*, Edited by J. F. Ziegler, (Pergamon, New York, 1985), Chap. 2, pp. 14–65.
- [229] J. F. Ziegler, J. P. Biersack, and M. D. Ziegler: *SRIM-The Stopping and Range of Ions in Matter*, (SRIM, Chester, MD, 2008), Chap. 2, pp. 2-1–49.
- [230] K. Ono, H. Ohta, and K. Eriguchi: *Thin Solid Films* **518**, 3461 (2010).
- [231] S. Tachi, K. Tsujimoto, S. Arai, and T. Kure: *J. Vac. Sci. Technol. A* **9**, 796 (1991).
- [232] K. Wittmaack: *Phys. Rev. B* **68**, 235211 (2003).
- [233] D. J. Oostra, R. P. van Ingen, A. Haring, and A. E. de Vries: *Appl. Phys. Lett.* **50**, 1506 (1987).
- [234] J. Hoshen and R. Kopelman: *Phys. Rev. B.* **12**, 3438 (1976).
- [235] J. Hoshen, R. Kopelman, and E. M. Monberg: *J. Stat. Phys.* **19**, 219 (1978).
- [236] J. Hoshen, P. Klymko, and R. Kopelman: *J. Stat. Phys.* **21**, 583 (1979).
- [237] D. B. Graves and P. Brault: *J. Phys. D: Appl. Phys.* **42**, 194011 (2009).
- [238] F. H. Stillinger and T. A. Weber: *Phys. Rev. B* **3**, 5262 (1985).
- [239] F. H. Stillinger and T. A. Weber: *J. Chem. Phys.* **88**, 5123 (1988).
- [240] F. H. Stillinger and T. A. Weber: *Phys. Rev. Lett.* **62**, 2144 (1989).
- [241] T. A. Weber and F. H. Stillinger: *J. Chem. Phys.* **92**, 6239 (1990).
- [242] H. J. C. Berendsen, J. P. M. Postma, W. F. van Gunsteren, A. DiNola, and J. R. Haak: *J. Chem. Phys.* **81**, 3684 (1984).
- [243] D. E. Hanson, A. F. Voter, and J. D. Kress: *J. Appl. Phys.* **82**, 3552 (1997).
- [244] D. E. Hanson, J. D. Kress, and A. F. Voter: *J. Vac. Sci. Technol. A* **17**, 1510 (1999).
- [245] H. Ohta and S. Hamaguchi: *J. Vac. Sci. Technol. A* **19**, 2373 (2001).
- [246] R. Smith and D. E. Harrison, Jr.: *Comput. Phys.* **3**, 68 (1989).
- [247] R. Smith, D. E. Harrison, Jr., and B. J. Garrison: *Phys. Rev. B* **40**, 93 (1989).
- [248] C. K. Birdsall: *IEEE Trans. Plasma Sci.* **19**, 65 (1991).
- [249] Y. Takao, N. Kusaba, K. Eriguchi, and K. Ono: *J. Appl. Phys.* **108**, 093309 (2010).
- [250] G. P. Srivastava: *J. Phys. A: Math. Gen.* **17**, L317 (1984).

List of Publications

Journal Paper

1. Nobuya Nakazaki, Yoshinori Takao, Koji Eriguchi and Kouichi Ono, “Molecular dynamics simulations of silicon chloride ion incidence during Si etching in Cl-based plasmas,” *Jpn. J. Appl. Phys.* **53**, 056201-1–9 (2014).
<DOI:10.7567/JJAP.53.056201>
* 第37回 (2015年度) 応用物理学会論文奨励賞受賞
2. Hirotaka Tsuda, Nobuya Nakazaki, Yoshinori Takao, Koji Eriguchi, and Kouichi Ono, “Surface roughening and rippling during plasma etching of silicon: Numerical investigations and a comparison with experiments,” *J. Vac. Sci. Technol. B* **32**, 031212-1–21 (2014).
<DOI: 10.1116/1.4874309>, <<http://hdl.handle.net/2433/193618>>
3. Nobuya Nakazaki, Hirotaka Tsuda, Yoshinori Takao, Koji Eriguchi and Kouichi Ono, “Two modes of surface roughening during plasma etching of silicon: Role of ionized etch products,” *J. Appl. Phys.* **116**, 223302-1–20 (2014).
<DOI:10.1063/1.4903956>, <<http://hdl.handle.net/2433/193256>>
4. Nobuya Nakazaki, Yoshinori Takao, Koji Eriguchi, and Kouichi Ono, “Molecular dynamics simulations of Si etching in Cl- and Br-based plasmas: Cl⁺ and Br⁺ ion incidence in the presence of Cl and Br neutrals,” *J. Appl. Phys.* **118**, 233304-1–18 (2015).
<DOI:10.1063/1.4937449>, <<http://hdl.handle.net/2433/203166>>

International Conference

1. Nobuya Nakazaki, Hirotaka Tsuda, Yoshinori Takao, Koji Eriguchi, and Kouichi Ono, "Molecular Dynamics Analysis of Ion Incident Energy and Angle Dependence of Si etching with Cl, Br, and HBr beams," 33rd International Symposium on Dry Process, Nov. 10~11, 2011, Kyoto Garden Palace Hotel, Kyoto, Japan, P1-16, in *Proc. 33rd Int. Symp. Dry Process*, pp. 53–54.
2. Nobuya Nakazaki, Hirotaka Tsuda, Yoshinori Takao, Koji Eriguchi, and Kouichi Ono, "Molecular Dynamics Analysis of Ion Incident Energy and Angle Dependences of Si etching with Cl, Br, and HBr beams," 64th Annual Gaseous Electronics Conference, Nov. 15~18, 2011, Salt Palace Convention Center, Salt Lake City, UT, USA, NR1-11, in *Bull. Am. Phys. Soc.* **56**(15), p. 64.
3. Nobuya Nakazaki, Hirotaka Tsuda, Yoshinori Takao, Koji Eriguchi, and Kouichi Ono, "Molecular Dynamics Analysis of Si Etching with Cl beams: Ion Incident Angle and Neutral Radical Flux Dependence," The 5th International Conference on Plasma-Nanotechnology & Science, Mar. 9~10, 2012, Inuyama International Sightseeing Center, Aichi, Japan, S-2, in *The 5th International Conference on Plasma-Nanotechnology & Science*, pp. P-36.
4. Nobuya Nakazaki, Yoshinori Takao, Koji Eriguchi, and Kouichi Ono, "Molecular Dynamics Analysis of Si Etching in Cl- and Br-based Plasmas," The 11th Asia Pacific Conference on Plasma Science and Technology and 25th Symposium on Plasma Science for Materials, Oct. 2~5, 2012, Kyoto University ROHM Plaza, Kyoto, Japan, 2-P28, in *Abstracts*, p. 266.
5. Nobuya Nakazaki, Yoshinori Takao, Koji Eriguchi, and Kouichi Ono, "Molecular Dynamics Analysis of Physical and Chemical Behavior of Etch Products Desorbed during Si Etching in Cl- and Br-based Plasmas," The 65th Annual Gaseous Electronics Conference, Oct. 22~26, 2012, the AT&T Conference Center on The University of Texas at Austin campus in Austin, TX, USA, HW2-5, in *Bull. Am. Phys. Soc.* **57**(8), p. 46.
6. Nobuya Nakazaki, Hirotaka Tsuda, Yoshinori Takao, Koji Eriguchi, and Kouichi Ono, "Molecular Dynamics Analysis of Si Etching with Cl and Br Beams: Ion Incident Angle and Neutral Radical Flux Dependence," American Vacuum Society 59th International Symposium & Exhibition, Oct. 28~Nov. 2, 2012, Tampa Convention Center, Tampa, FL, USA, PS2-TuA10.
7. Nobuya Nakazaki, Hirotaka Tsuda, Yoshinori Takao, Koji Eriguchi, and Kouichi Ono, "Molecular Dynamics Analysis of Surface Structure and Etch Products in Si/Cl and Si/Br Systems," 34th International Symposium on Dry Process, Nov. 15~16, 2012, The University of Tokyo, Tokyo, Japan, P-33, in *Proc. 34th Int. Symp. Dry Process*, pp. 91–92.
8. Nobuya Nakazaki, Yoshinori Takao, Koji Eriguchi, and Kouichi Ono, "Molecular dynamics analysis of Si etching in HBr-based plasmas: Effects of neutral radicals," 35th International Symposium on Dry Process, Aug. 29~30, 2013, Ramada Plaza Jeju Hotel, Korea, P-74, in *Proc. 35th Int. Symp. Dry Process*, pp. 159–160.

9. Nobuya Nakazaki, Yoshinori Takao, Koji Eriguchi, and Kouichi Ono, "Molecular Dynamics Analysis of Surface Reaction Kinetics during Si Etching in Cl-based Plasmas: Effects of Etch By-Products Ion Incidence," The 66th Annual Gaseous Electronics Conference, Sep. 30~Oct. 4, 2013, the Westin Hotel, Princeton, NJ, USA, LW1-6, in *Bull. Am. Phys. Soc.* **58**(8), p. 71.
10. Nobuya Nakazaki, Yoshinori Takao, Koji Eriguchi, and Kouichi Ono, "Molecular Dynamics Analysis of Si Etching in HBr-based Plasmas: Ion Incident Energy and Angle Dependence," American Vacuum Society 60th International Symposium & Exhibition, Oct. 27~Nov. 1, 2013, the Long Beach Convention Center, Long Beach, CA, USA, PS-ThM-1.
11. Nobuya Nakazaki, Yoshinori Takao, Koji Eriguchi, and Kouichi Ono, "Surface roughening during Si etching in inductively coupled Cl₂ plasmas," 8th International Conference on Reactive Plasmas and 31st Symposium on Plasma Processing, Feb. 3~7, 2014, Fukuoka Convention Center, Fukuoka, Japan, 4B-PM-O2.
12. Nobuya Nakazaki, Koji Eriguchi, and Kouichi Ono, "Molecular dynamics analysis of silicon chloride ion incidence during Si etching in Cl-based plasmas: Effects of ion incident energy, angle, and neutral radical-to-ion flux ratio," The 67th Annual Gaseous Electronics Conference, Nov. 2~7, 2014, Marriott City Center & Raleigh Convention Center, Raleigh, NC, USA, ET2-5, in *Bull. Am. Phys. Soc.* **59**(9), p. 26.
13. Nobuya Nakazaki, Haruka Matsumoto, Koji Eriguchi, and Kouichi Ono, "Surface Roughening Mechanisms and Roughness Suppression during Si Etching in Inductively Coupled Cl₂ Plasmas," American Vacuum Society 61st International Symposium & Exhibition, Nov. 9~14, 2014, the Baltimore Convention Center, Baltimore, MD, USA, PS1-WeM-12.
14. Nobuya Nakazaki, Haruka Matsumoto, Koji Eriguchi, and Kouichi Ono, "Surface rippling by oblique ion incidence during plasma etching of silicon: Experimental demonstration using sheath control plates," 68th Annual Gaseous Electronics Conference/9th International Conference on Reactive Plasmas/33rd Symposium on Plasma Processing, Oct. 12~16, 2015, Hawaii Convention Center, Honolulu, HI, USA, OR2-4, in *Bull. Am. Phys. Soc.* **60**(9), p. 118.
15. Nobuya Nakazaki, Haruka Matsumoto, Soma Sonobe, Yoshinori Takao, Koji Eriguchi, and Kouichi Ono, "Experimental demonstration of oblique ion incidence with sheath control plates during plasma etching of silicon," 37th International Symposium on Dry Process, Nov. 5~6, 2015, Awaji Yumebutai International Conference Center, Awaji Island, Japan, B-3, in *Proc. 37th Int. Symp. Dry Process*, pp. 13~14.

Japanese Conference

1. 中崎暢也、谷口健、津田博隆、鷹尾祥典、江利口浩二、斧高一、「分子動力学法を用いた Si エッチング表面反応解析：Cl, Br, HBr ビームエッチングにおけるイオン入射角度依存性」、2011 年度春季第 58 回応用物理学関係連合講演会、2011 年 3 月 24～27 日、神奈川工科大学。（東日本震災により講演会中止）
2. 中崎暢也、谷口健、津田博隆、鷹尾祥典、江利口浩二、斧高一、「分子動力学法を用いた Si エッチング表面反応解析：Cl, Br, HBr ビームエッチングにおけるイオン入射角度依存性及び入射エネルギー依存性」、2011 年秋季第 72 回応用物理学学会学術講演会、2011 年 8 月 29 日～9 月 2 日、山形大学小白川キャンパス、30a-M-12.
3. 中崎暢也、津田博隆、鷹尾祥典、江利口浩二、斧高一、「分子動力学法を用いた Si エッチング表面反応解析：中性ラジカル付加とイオンビーム入射角度依存性」、プラズマ・核融合学会第 28 回年会／応用物理学学会第 29 回プラズマプロセッシング研究会／日本物理学会（領域 2）2011 年秋季大会／Plasma Conference 2011、2011 年 11 月 22～25 日、石川県立音楽堂、22B01.
4. 中崎暢也、津田博隆、鷹尾祥典、江利口浩二、斧高一、「分子動力学法を用いた Si/Cl ビームエッチング表面反応解析：イオン入射角度依存性と中性ラジカルフラックス依存性」、第 59 回応用物理学関係連合講演会、2012 年 3 月 15～18 日、早稲田大学、17p-A7-15.
5. 中崎暢也、津田博隆、鷹尾祥典、江利口浩二、斧高一、「分子動力学法による Si/Cl, Si/Br ビームエッチング表面反応解析：イオン入射エネルギー・角度と中性ラジカルフラックス比依存性」、2012 年秋季第 73 回応用物理学学会学術講演会、2012 年 9 月 11～14 日、愛媛大学、13a-E3-11.

*** 第 33 回 (2012 年秋季) 応用物理学学会講演奨励賞受賞**

6. 中崎暢也、津田博隆、鷹尾祥典、江利口浩二、斧高一、「分子動力学法による Si/Cl, Si/Br プラズマエッチングの解析：表面反応層内の原子分布と結合状態」、第 30 回プラズマプロセッシング研究会、2013 年 1 月 21～23 日、アクトシティ浜松・研修交流センター、B1-02.
7. **【招待講演】** 中崎暢也、津田博隆、鷹尾祥典、江利口浩二、斧高一、「分子動力学法を用いた HBr プラズマによる Si エッチング表面反応解析」、2013 年春季第 60 回応用物理学学会学術講演会、2013 年 3 月 27～30 日、神奈川工科大学、27p-A3-9.

*** 応用物理学学会講演奨励賞受賞記念講演**

8. 中崎暢也、鷹尾祥典、江利口浩二、斧高一、「プラズマエッチングにおけるナノスケール表面ラフネスとリップル構造」、応用物理学学会関西支部平成 25 年度第 1 回講演会、2013 年 6 月 13 日、京都大学桂キャンパス、P-14.

*** 応用物理学会関西支部平成 25 年度第 1 回講演会ポスター賞 (最優秀賞) 受賞**

9. 中崎暢也、鷹尾祥典、江利口浩二、斧高一、「分子動力学法を用いた塩素系プラズマによる Si エッチング表面反応解析：エッチング副生成物イオン入射の効果」、第 74 回応用物理学会秋季学術講演会、2013 年 9 月 16～20 日、同志社大学京田辺キャンパス、18a-C2-7.
10. 中崎暢也、鷹尾祥典、江利口浩二、斧高一、「Molecular dynamics simulation of etch by-product ion incidence during Si etching in Cl-based plasmas」、第 26 回プラズマ材料科学シンポジウム、2013 年 9 月 23～24 日、九州大学医学部百年講堂、24a-A-2.
11. 中崎暢也、鷹尾祥典、江利口浩二、斧高一、「分子動力学法による塩素系プラズマ Si エッチングの表面反応解析：エッチング副生成物イオンの斜め入射」、第 61 回応用物理学会春季学術講演会、2014 年 3 月 17～20 日、青山学院大学相模原キャンパス、19a-F6-2.
12. 中崎暢也、松本悠、鷹尾祥典、江利口浩二、斧高一、「誘導結合 Cl₂ プラズマ Si エッチングにおける表面ラフネスの解析」、第 61 回応用物理学会春季学術講演会、2014 年 3 月 17～20 日、青山学院大学相模原キャンパス、19a-F6-4.
13. 中崎暢也、松本悠、江利口浩二、斧高一、「誘導結合 Cl₂ プラズマ Si エッチングにおける表面ラフネスの解析：パルスバイアスエッチングの効果」、第 75 回応用物理学会秋季学術講演会、2014 年 9 月 17～20 日、北海道大学札幌キャンパス、19p-S10-6.
14. **【招待講演】** 中崎暢也、初瀬巧、松本悠、津田博隆、鷹尾祥典、江利口浩二、斧高一、「Cl₂ プラズマ Si エッチングにおける表面ラフネスの解析」、応用物理学会シリコンテクノロジー分科会第 178 回研究集会、2015 年 2 月 13 日、東京大学.
15. 中崎暢也、園部蒼馬、初瀬巧、松本悠、江利口浩二、斧高一、「シースコントロールプレートを用いた基板表面へのイオン斜入射とリップル形成」、第 62 回応用物理学会春季学術講演会、2015 年 3 月 11～14 日、東海大学湘南キャンパス、14p-A27-7.
16. **【招待講演】** 中崎暢也、鷹尾祥典、江利口浩二、斧高一、「Molecular dynamics simulations of silicon chloride ion incidence during Si etching in Cl-based plasmas」、第 76 回応用物理学会秋季学術講演会、2015 年 9 月 13 日～16 日、名古屋国際会議場、15a-2Q-7.

*** 応用物理学会論文奨励賞受賞記念講演**

Review

1. 中崎暢也、「研究紹介：分子動力学法を用いたハロゲン系プラズマによる Si エッチング表面反応解析」、プラズマエレクトロニクス分科会会報 No. 58, pp. 21–22、2013 年 6 月． <http://annex.jsap.or.jp/plasma/PE_files/PE58.pdf>
2. 斧高一、津田博隆、中崎暢也、鷹尾祥典、江利口浩二、「プラズマナノ加工における表面ラフネスとリップル形成機構」、表面科学 Vol. 34, No.10, pp. 528–534、2013 年 10 月． <https://www.jstage.jst.go.jp/article/jssj/34/10/34_528/_article>
3. 斧高一、中崎暢也、津田博隆、鷹尾祥典、江利口浩二、「プラズマエッチングにおけるナノスケール表面形状揺らぎ」、プラズマ・核融合学会誌 Vol. 90, No. 7, pp. 398–404、2014 年 6 月． <<http://ci.nii.ac.jp/naid/110009839098>>
4. 中崎暢也、初瀬巧、松本悠、津田博隆、鷹尾祥典、江利口浩二、斧高一、「Cl₂ プラズマ Si エッチングにおける表面ラフネスの解析」、シリコンテクノロジー「微細加工プロセスの最前線」 No. 178, pp. 24–29、2015 年 2 月．

Award

1. 第 33 回（2012 年秋季）応用物理学会講演奨励賞、2013 年 3 月 27 日．
2. 応用物理学会関西支部平成 25 年度第 1 回講演会ポスター賞（最優秀賞）、2013 年 6 月 13 日．
3. 応用物理学会関西支部第 2 回関西奨励賞、2014 年 2 月 28 日．
4. 第 37 回（2015 年度）応用物理学会論文奨励賞、2015 年 9 月 13 日．